

Catalyst Development for Selective Hydrogenation of Functionalized Alkynes and Nitroarenes

THÈSE N° 6464 (2014)

PRÉSENTÉE LE 16 DÉCEMBRE 2014

À LA FACULTÉ DES SCIENCES DE BASE

LABORATOIRE DE GÉNIE DE LA RÉACTION CHIMIQUE

PROGRAMME DOCTORAL EN CHIMIE ET GÉNIE CHIMIQUE

ÉCOLE POLYTECHNIQUE FÉDÉRALE DE LAUSANNE

POUR L'OBTENTION DU GRADE DE DOCTEUR ÈS SCIENCES

PAR

Artur YARULIN

acceptée sur proposition du jury:

Prof. B. Fierz, président du jury

Prof. L. Kiwi, directrice de thèse

Dr B. Louis, rapporteur

Prof. J. Luterbacher, rapporteur

Prof. D. Murzin, rapporteur



ÉCOLE POLYTECHNIQUE
FÉDÉRALE DE LAUSANNE

Suisse
2014

To my parents

Посвящаю моим родителям

Acknowledgements

First of all, I thank Prof. Lioubov Kiwi-Minsker for having accepted me in her group as a master thesis intern and further as a PhD student. These almost 4.5 years altogether were a great and unforgettable journey for me. I would like to thank her for her care, lessons of science and life, and especially for gathering a team of great people within GGRC.

I thank Prof. Dmitry Murzin, Dr. Benoît Louis and Prof. Jeremy Luterbacher for their tricky, challenging and yet enjoyable questions during my thesis defense brilliantly chaired by Prof. Beat Fierz. I deeply appreciate our discussions during and after the exam.

I had the opportunity to work with Prof. Albert Renken as an assistant of his course. I thank him for this experience and the multiple stories he shared with me during this time.

I owe a big part of this thesis to Igor who helped me through my research. I thank him for being my tutor for the last 4 years.

If I learnt how to structure my ideas and produce the articles there is a huge impact of Fernando, a professional papers writer, but also a nice flat mate and a good friend.

I would like to thank my friend Julien for all fun we had during our PhD time: wakeboarding/snowboarding, weekly training sessions to prepare to meet Veronica's

parents, surprise birthday parties. Special thanks for everything that preceded me appearing in a purple t-shirt at EPFL. I thank my office musketeers Daniel and Charline for their French lessons, friendship, mousse au chocolat, being angry when I moved away and many more. Big thanks to Guillaume a soccer guy for the high-level “Inter Milan is not a very strong team”-type discussions, and teaching me Français stylé. I thank our youngest PhD student Oliver for taking care of his health every day of the week except Saturdays, Sundays and les jours fériés. Many thanks to Sasha for bringing a peace of chaos into my office. Also for being responsible together with Daniel for all the entertainment during my last few months at EPFL: fondues, alsacien wines, Ricks & Morties, roof walks and roof drivings. I thank our great postdocs: Micaela = scientist + mother, Anne-Laure = scientist + applemaniac, Tatiana = scientist + safety, Madhav = scientist + moustache. I am thankful to my master students Ana and Alexandra for giving me hard times but also great results. I thank Edi for his energy enough to light up the whole EPFL, no solar cells would be needed. I thank the people from atelier and magasin, who are simply the best, as well as our secretaries who helped us to survive among the piles of bills and payment slips.

Everything I achieved is owing to my parents and my little sister who always support me and who lived this thesis with me.

Finally, I thank Irisha who came to the lab and changed my life. And also did a nice Master project.

Abstract

Catalyst design is of major importance for fine chemicals industry due to complexity of the synthesis and high product quality requirements. Moreover, the catalyst formulation has to comply with the standards of health, safety and environmental regulations. The conventional systems often do not satisfy the latter criteria and, therefore, have to be improved to become both efficient and eco-friendly. The advancing technologies of materials synthesis and characterization allow catalyst development from *model* systems (*i.e.* colloidal metal nanoparticles (NPs)) towards *real* heterogeneous catalysts for industrial implementation.

The main approach taken in this thesis is based on surface and electronic structure design of the catalytically active NPs (Pd, Pt) by means of size control (2.1 – 9.8 nm) and modification by a second component (Ag, Cu, Zn) during the catalyst preparation.

We analyzed the size effect of unsupported Pd NPs in the selective hydrogenation of alkynols with different alkyl chains, *i.e.* C₁₆ in dehydroisophytol (to isophytol) and C₁ in methylbutynol (to methylbutenol). Antipathetic structure sensitivity was established where larger Pd NPs exhibit intrinsically higher (up to *ca.* 2-fold) specific activity (per Pd surface atom). A higher Pd dispersion delivered greater yields to isophytol (89 → 93%), while the product distribution in methylbutynol hydrogenation was insensitive to NP size. The distinct size effect on hydrogenation performance for

both α -alkynols is associated with modifications in the adsorption strength linked to the hydrocarbon chain length. Furthermore, the incorporation of Ag or Cu in Pd NPs had a critical impact on yield to the target isophytol (up to 97%). This result is attributed to the dilution of the Pd surface sites by a second metal (Ag, Cu) and a modification of the Pd electronic properties. Pd-Ag NPs, having shown the highest selectivity, were further deposited on a structured support based on sintered metal fibers (SMF) coated with ZnO. The improved selectivity achieved over the unsupported Pd-Ag colloidal particles was retained over the structured catalytic system. The resulted Pd-Ag/ZnO/SMF (*patent WO 2013/060821 A1*) represents a viable alternative to the conventional Lindlar catalyst.

Another bimetallic system was studied in selective 3-nitrostyrene hydrogenation, where Pt catalyst was modified by alloying with Zn through the reactive metal–support interactions. Pt/ZnO catalyst containing monodispersed Pt NPs (*ca.* 2.3 nm) favored 3-vinylaniline formation (97%) showing a remarkable activity (close to that of the benchmark Pt catalysts), *i.e.* the catalyst had superior combined selectivity/activity response as compared to the reported literature. Additionally, the catalytic tests were performed over bimetallic Pt-Zn NPs embeded within the hypercross-linked polystyrene (HPS) support. The controlled pore size of HPS (*ca.* 4 nm) allows immobilization and a NP size control by confining Pt within the nanocavities of the polymeric matrix. The catalytic results demonstrated boosted yields towards 3-vinylaniline (16 \rightarrow 97%) over Pt-Zn/HPS catalyst as compared to monometallic Pt/HPS.

The findings presented here over monodispersed NPs establish the basis of catalyst development for the selective production of fine chemicals. The product distribution can be controlled on a *nano-level* by tuning the properties of the active phase through the particle size optimization and incorporation of a second metal.

Keywords: Bimetallic nanoparticles, selective hydrogenation, Pd, Pd-Ag, Pd-Cu, Pt, Pt-Zn, alkynols, nitrostyrene.

Version Abrégée

La conception des catalyseurs est très importante pour l'industrie de chimie fine en raison de la complexité des synthèses et des hautes exigences en matière de qualité du produit. De plus, la formulation du catalyseur doit être en adéquation avec les standards de santé, sécurité et environnementaux. Souvent, les systèmes catalytiques conventionnels ne répondent pas à toutes les exigences et doivent donc être améliorés pour devenir à la fois efficaces et respectueux de l'environnement. L'avancement des technologies pour la synthèse et de caractérisation des matériaux permet le développement d'un catalyseur à partir de systèmes *modèles* – constitués de nanoparticules (NPs) métalliques colloïdales – jusqu'aux catalyseurs hétérogènes *réels*, pour une implémentation industrielle.

Dans cette thèse, une méthode reposant sur des NPs catalytiques (Pd, Pt) conçues sur mesure par le contrôle de leur taille (2.1 – 9.8 nm) et par la modification de la phase active avec un second métal (Ag, Cu, Zn) est employée. Nous avons analysé l'effet de taille des NPs colloïdales de Pd sur les hydrogénations sélectives d'alcynols avec des chaînes alkyles différentes, c'est-à-dire C₁₆ dans dehydroisophytol (en isophytol) et C₁ dans methylbutynol (en methylbutenol). La sensibilité à la structure a été établie, où les NPs de Pd plus grandes ont montré une activité spécifique (par

atome de surface de Pd) deux fois plus élevée. En revanche, les NPs de Pd plus petites ont fourni un rendement en isophytol plus élevé ($89 \rightarrow 93\%$), tandis que la distribution des produits dans l'hydrogénation du methylbutynol n'est pas affectée par la taille des NPs. On a associé cette sensibilité à la structure à des modifications de l'énergie d'adsorption qui est dépendante de la taille de chaîne alkyle. En outre, une augmentation du rendement en isophytol (jusqu'à 97%) a été démontrée avec le Pd modifié par Ag ou Cu. Ce résultat est attribué à la formation d'un l'alliage intermétallique (Pd-Ag ou Pd-Cu) et à la modification des propriétés électroniques et géométriques du Pd. La sélectivité la plus haute ayant été obtenue avec les NPs de Pd-Ag, celles-ci ont été immobilisées sur un support structuré composé de fibres métalliques frittées (SMF) recouvertes de ZnO. La sélectivité obtenue sur des particules de Pd-Ag colloïdales a été maintenue sur le système catalytique structuré. Le système Pd-Ag/ZnO/SMF qui en résulte (*patente WO 2013/060821 A1*) représente une alternative viable au catalyseur de Lindlar.

Un autre système catalytique de Pt modifié par le Zn (Pt/ZnO) a été étudié dans l'hydrogénation sélective du 3-nitrostyrène. Le Pt/ZnO contenant des NPs monodispersées de Pt (*env.* 2.3 nm) est favorable à la formation du 3-vinylaniline (97%) et montre une activité remarquable (proche de celle des catalyseurs de référence). De plus, des tests catalytiques ont été effectués sur des NPs bimétalliques immobilisées sur du polystyrène hyper-réticulé (HPS). La taille des pores du HPS (*env.* 4 nm) permet de contrôler la taille des NPs de Pt en les confinant dans les nanocavités de la matrice polymérique. Les résultats catalytiques ont démontré des

rendements en 3-vinylaniline grandement améliorés (16 → 97%) sur le Pt-Zn/HPS en comparaison de ceux obtenus avec le catalyseur monométallique de Pt/HPS.

Les découvertes sur les NPs monodispersées présentées ici établissent la base pour un développement de catalyseurs dédiés à la fabrication sélective de produits de chimie fine, où la distribution des produits peut être contrôlée à l'échelle nanométrique par la modification des propriétés de la phase active. Cela peut être effectué par l'optimisation de la phase active au moyen de la taille des particules et par l'incorporation d'un second métal.

Mots-clés: Nanoparticules bimétalliques, hydrogénation sélective, Pd, Pd-Ag, Pd-Cu, Pt, Pt-Zn, alcynols, nitrostyrene.

Table of Contents

Acknowledgements	i
Abstract	iii
Version Abrégée	vii
Table of Contents	xi
List of Symbols	xv
Chapter 1. Introduction	1
1.1 Motivation and Objectives	1
1.2 Structure of the Work	3
Chapter 2. State of the Art	7
2.1 Hydrogenation Processes	7
2.1.1 Selective Hydrogenation of Alkynols	8
2.1.2 Selective Hydrogenation of Functionalized Nitroarenes	11
2.2 Catalyst Optimization for Hydrogenation Reactions	13
2.2.1 Effect of Metal Particle Size on Catalyst Performance	14
2.2.2 Active Phase Modification with Second Metal	18
2.2.2 Role of Support in Catalytic Hydrogenation	23
2.3 Size-Controlled Synthesis of Metal Nanoparticles	25
2.4 Unconventional Catalyst Supports	28

2.4.1 Sintered Metal Fibers	29
2.4.2 Hypercross-linked Polystyrene	29
Chapter 3. Selective Hydrogenation of Alkynols: Size effect of Pd Nanoparticles	31
Abstract	32
3.1 Introduction	33
3.2 Experimental	34
3.2.1 Materials	34
3.2.2 Catalyst Preparation	34
3.2.3 Catalyst Characterization	36
3.2.4 Catalytic Hydrogenation.	37
3.3 Results and Discussion	38
3.3.1 Characterization of Pd Nanoparticles	38
3.3.2 Catalytic Response of PVP-Stabilized Pd Nanoparticles	42
3.3.3 Structure Sensitivity of Alkynol Hydrogenation	44
3.3.4 Kinetic Model	56
3.4 Conclusions	63
Chapter 4. Selective Hydrogenation of Alkynols: Pd Modification with Second Metal	65
Abstract	66
4.1 Introduction	67
4.2 Experimental	68
4.2.1 Materials	68

4.2.2 Preparation of Mono- and Bimetallic Nanoparticles	69
4.2.3 Preparation of Supported Catalysts	70
4.2.4 Catalyst Characterization	71
4.2.5 Catalytic Hydrogenation	72
4.3 Results and Discussion	74
4.3.1 Characterization of Mono- and Bimetallic Nanocatalysts	74
4.3.2 Catalytic Results over Unsupported Nanoparticles	79
4.3.3 Catalytic Results over Supported Catalyst	87
4.4 Conclusions	91
Chapter 5. Hydrogenation of 3-Nitrostyrene: Pt Modification with the Zn	93
Abstract	94
5.1 Introduction	95
5.2 Experimental	96
5.2.1 Materials	96
5.2.2 Catalyst Preparation	97
5.2.3 Catalyst Characterization	97
5.2.4. Catalytic Hydrogenation	99
5.3. Results and Discussion	101
5.3.1 Catalyst Characterization	101
5.3.2. Influence of Metal-Support Interaction on Catalyst Performance	107
5.3.3 Effect of Reaction Conditions on Activity and Selectivity	113
5.4 Conclusions	117

Chapter 6. Hydrogenation of 3-Nitrostyrene: Pt-Zn Nanoparticles	
Supported on Porous Polymeric Matrix	119
Abstract	120
6.1 Introduction	121
6.2 Experimental	122
6.2.1 Materials	122
6.2.2 Catalyst Preparation	123
6.2.3. Catalyst Characterization	123
6.2.4 Catalytic Hydrogenation	124
6.3 Results and Discussion	127
6.3.1 Catalyst Characterization	127
6.3.2 Catalytic Results	132
6.4 Conclusions	139
Chapter 7. General Conclusions and Outlook	141
7.1 Achieved Results	141
7.2 Further Development	144
References	145
Curriculum Vitae	163

List of Symbols

Abbreviations

3-EA	3-ethylaniline
3-ENB	3-ethylnitrobenzene
3-NS	3-nitrostyrene
3-VA	3-vinylaniline
AAS	Atomic absorption spectroscopy
BE	Binding energy
CP	Condensation products
DIP	Dehydroisophytol
DRIFTS	Diffuse reflectance infrared Fourier transform spectroscopy
EDX	Energy dispersive X-ray spectroscopy
GC	Gas chromatography
HIP	Hydroisophytol
HPS	Hypercross-linked polystyrene
HRTEM	High resolution transmission electron microscopy
IP	Isophytol

M	Metal
MBA	2-methyl-3-butan-2-ol
MBE	2-methyl-3-buten-2-ol
MBY	2-methyl-3-butyn-2-ol
NP	Nanoparticle
PVP	Poly(N-vinyl-2-pyrrolidone)
SBR	Semi-batch reactor
SMF	Sintered metal fibers
SMSI	Strong metal-support interactions
SSA	Specific surface area
STEM	Scanning transmission electron microscopy
TCD	Thermal conductivity detector
TEM	Transmission electron microscopy
TOF	Turnover frequency
TPR	Temperature programmed reduction
VA	Vinylaniline
XPS	X-ray photoelectron spectroscopy
XRD	X-ray diffraction

Greek Symbols

γ_i	Surface energy of metal i	[J m ⁻²]
θ_i	Surface coverage of compound i	[-]
π	Pi-bond	
π^*	Pi-star molecular orbital	
σ	Sigma bond	
τ	Residence time	[s]

Roman Symbols

C_i	Concentration of compound i	[mol m ⁻³]
d	Metal diameter	[nm]
D	Dispersion	[-]
E_a	Activation energy	[J mol ⁻¹]
E_T^N	Solvent polarity	[-]
f_i	Fraction of compound i	[-]
K_i	Adsorption constant of compound i	[cm ³ mol ⁻¹]
k_i	Kinetic constant of reaction i	[mol mol ⁻¹ s ⁻¹]
n_i	Amount of compound i	[mol]
n_i	Number of particles of diameter d_i	[-]
P_{H_2}	Hydrogen pressure	[bar]
R_i	Transformation rate of compound i	[mol mol ⁻¹ s ⁻¹]

r_i	Reaction i	
r_i	Atomic radius of metal i	[nm]
S_i	Selectivity towards compound i	[-]
T	Temperature	[K]
t	Time	[s]
T_A	Activation temperature	[K]
t_R	Reaction time	[s]
T_R	Reaction temperature	[K]
V_{tot}	Volume of reacting mixture	[m ³]
x_i	Fraction of specific surface atoms	[-]
X_i	Conversion of compound i	[-]

Subscripts

i	Generic compound
edge	Edge atoms
plane	Plane atoms
surf	Surface atoms
tot	Total
Y	Alkynol
E	Alkenol
H	Hydrogen

A	Alkanol	
R	Reacting mixture	
core	Core atoms	
shell	Shell atoms	
x	Molar ratio	[-]

Superscripts

*	Active center	
n	Number of Hydrogen atoms attached to a molecule	[-]

Chapter 1

Introduction

This chapter formulates the objectives of the present work and provides the structure of the whole thesis.

1.1 Motivation and Objectives

Catalysis as a scientific discipline originated in the early 20th century with one of the main research interests focusing on the development of metal catalysts for hydrogenation [1]. Nowadays, more than a century later, this topic is still a top priority in the field. Modern technologies allow control over composition, size and morphology of the catalytically active particles giving rise to important improvements in the catalyst performance. On the other hand, the increasing environmental concerns necessitate development of ecologically harmless and sustainable processes. These two factors define the directions of catalysis evolution.

This thesis addresses several key problems of catalytic processes that involve hydrogenation of the molecules containing unsaturated carbon-carbon bonds. Two groups of reactions can be identified: (i) $\text{C}\equiv\text{C} \rightarrow \text{C}=\text{C}$ transformation, where the full hydrogenation of the unsaturated group must be avoided, and (ii) hydrogenation of poly-substituted molecules where the $\text{C}=\text{C}$ functionality has to be preserved. This is a very challenging task since vinyl groups are readily hydrogenated. Metal catalysts, being unable to provide high selectivities to the target products, are usually complemented by the additional modifiers dissolved in the reaction mixture. However, separation and treatment of such compounds after the reaction cycle is costly and can be harmful for the environment. On the other hand, a switch from *mono-* to *bimetallic* catalysts was demonstrated to impact the catalytic response through the modification of the properties of the active phase. This approach represents a more sustainable alternative to the employment of reaction modifiers.

Another issue associated with many catalytic hydrogenations is their structure sensitivity. In this type of reactions, modifications in metal particle size were identified as effective means of influencing catalyst activity/selectivity. Conventional methods of catalyst preparations require harsh heat treatment steps and, therefore, lack control over metal dispersion and nanoparticle (NP) size distribution. Moreover, the relationship between the performance and properties of the active phase is difficult to establish in classical heterogeneous catalysis due to the number of variables that can affect catalytic response. The unsupported metal NPs as *model* systems allow a systematic analysis of critical characteristics (such as particle size)

affecting the activity/selectivity response. Once the model system has been optimized, the information obtained can be employed to design a *real* supported catalyst.

The main objective of this work is the development of metal catalysts for selective hydrogenation of alkynols and nitrostyrene as model, yet industrially important, reactions. In both cases, the reduction of target C=C group has to be avoided. The strategy of the design is focused on increased catalyst performance by modification of intrinsic properties of the active metal, *i.e.* without addition of selectivity promoters to the reaction mixture. The final catalysts should be usable in the processes under real reaction conditions for industrial implementations.

1.2 Structure of the Work

This project is focused on catalyst optimization for hydrogenation reactions through the strict control of metal NP size and modification of the active phase by the second metal. In **Chapter 2**, the current state of the art relevant to this work is reviewed. The following **Chapters 3 – 6** constitute the main part of the thesis showing the experiments carried out and the results obtained during this work. In order to facilitate the understanding of the project scope, a general layout of these chapters is schematically represented in **Figure 1.1**.

Chapter 3 presents the results over the size-tailored (2.1 – 9.8 nm) Pd NPs tested *unsupported* in liquid-phase selective hydrogenation of alkynols. The nanocatalysts were synthesized *via* colloidal technique with poly(N-vinyl-2-pyrrolidone) (PVP) as a stabilizing agent to generate monodispersed particles. The effect of metal dispersion

was studied for the molecules with different alkyl chains: C₁₆ in dehydroisophytol (DIP) and C₁ in 2-methyl-3-butyn-2-ol (MBY). The established structure sensitivity of the reactions was rationalized using kinetic model based on the Langmuir-Hinshelwood mechanism.

The catalyst developed in Chapter 3, was further optimized by modifying Pd with the second metal for the application in DIP hydrogenation (**Chapter 4**). A series of *unsupported* bimetallic Pd-Ag and Pd-Cu NPs with different Pd/modifier molar ratios were examined as model systems. The bimetallic structure of the particles was analyzed by means of energy-dispersive X-ray spectroscopy (EDX). Further, in order to assess real catalytic systems, the optimized model nanocatalysts were deposited on a structured support based on sintered metal fibers (SMF) coated with ZnO. The resulted Pd-Ag/ZnO/SMF was compared to the benchmark in terms of activity and selectivity in solvent-free DIP hydrogenation. In addition, the stability of the developed catalyst was evaluated in a series of consecutive runs.

The approach of active phase modification by incorporation of the second metal was taken further to study the promoting effect of Zn on Pt-catalyzed liquid-phase hydrogenation of 3-nitrostyrene (3-NS) (**Chapter 5**). Monodispersed bimetallic NPs were generated on ZnO support during the catalyst activation. A series of critical characterization techniques (XPS, XRD) were used to assess the Pt-Zn alloy formation. In order to extend the boundaries of catalyst application, bimetallic Pt-Zn NPs were prepared inside the “pores” of the hypercross-linked polystyrene (HPS) and tested in 3-NS hydrogenation (**Chapter 6**). HPS possesses several advantages compared to ZnO, such as high specific surface area and controlled “pore” size, which

allows formation of small metal NPs with narrow size distribution even at high metal loadings.

Finally, **Chapter 7** summarizes the findings of the study and presents general conclusions and outlook.

Catalyst Development for Selective Hydrogenation

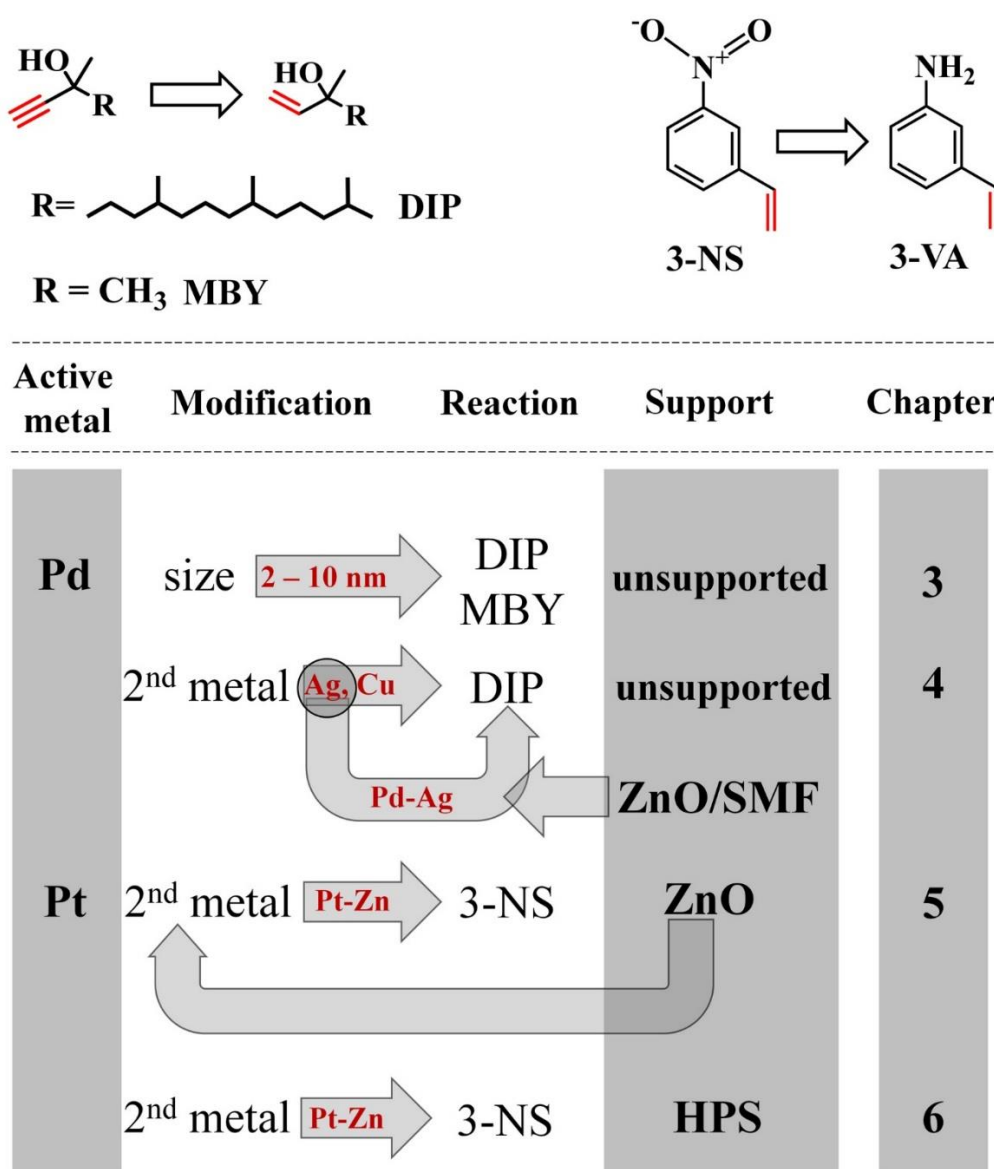


Figure 1.1. Graphical representation of the project scope.

Chapter 2

State of the Art

This chapter provides a brief introduction into the catalyst design for hydrogenation reactions. In each section, theoretical aspects of the corresponding topics are given and complemented with the current state of the art concerning the subject.

2.1 Hydrogenation Processes

Catalysis is crucial in green chemistry and vital for sustainable process design [2]. Hydrogenations are among the most extensively applied catalytic reactions in chemical industry [3, 4]. From the environmental point of view, reduction with H₂ is an atom efficient transformation and undoubtedly the cleanest method for organic molecule reduction [5]. With a continuously increasing application scope, about 10% of all chemical reactions in multistep syntheses of pharmaceuticals, vitamins and fine

chemicals are catalytic hydrogenations [6]. It is clear that these transformations should be highly selective, in order to preserve the target functionalities and to provide high yields of the final products. The prominent examples are hydrogenations where the target products contain a C=C functional group, such as semi-hydrogenation of alkynols to alkenols [7, 8], and reduction of C=C-functionalized nitroarenes to the corresponding anilines [9].

2.1.1 Selective Hydrogenation of Alkynols

A wealth of chemical processes in pharmaceutical, agrochemical and petrochemical industries is based on hydrogenation of unsaturated hydrocarbons over heterogeneous catalysts [10]. Particularly, semi-hydrogenations of alkynols to corresponding alkenols are fundamental reactions for the production of vitamins [8]. A simplified reaction network illustrating possible hydrogenation pathways is presented in **Figure 2.1**. Alkynol can either be semi-hydrogenated to alkenol (reaction 1) or directly hydrogenated to alkanol (reaction 2). On the other hand, alkenol can be over-hydrogenated to alkanol through reaction 3.

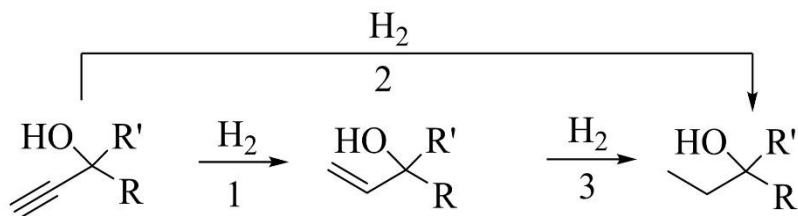


Figure 2.1. Reaction network associated with hydrogenation of alkynol.

A number of metals (*e.g.* Rh, Ni, Pd and Pt) have been tested as catalysts in this type of reactions. Among them, Pd was identified as the most effective in terms of combined high activity and selectivity to the target alkenol [10]. The observed catalytic response was attributed to a stronger adsorption of C \equiv C group (relative to C=C) on the Pd surface [11]. Nevertheless, the formation of undesired over-hydrogenated products (alkanols) is also promoted by Pd catalysts to some extent [12]. In order to increase the olefin yield, selectivity enhancers are commonly added into the reaction mixture [13]. Up to 100% alkenol selectivity was achieved using S-, N- and/or O-containing compounds (*e.g.* quinoline, 2,2'-ethylenedioxydiethanol, 2,2'-ethylenedithiodiethanol, 3,6-dithia-1,8-octanediol) or metal salts (Mn²⁺, Pb²⁺) as reaction modifiers [13-17]. The main drawback of this approach is the additional costs of product separation and waste treatment steps before their disposal as well as the negative environmental impact [18].

The mechanism of C \equiv C hydrogenation is still a subject of extensive investigations [7], but the general consensus that emerges from the literature is that a Pd-catalyzed reaction follows the Langmuir-Hinshelwood mechanism with an associative and/or dissociative adsorption of alkynol and H₂ on the catalyst surface [19-21]. The C \equiv C bond transformation during hydrogenation can involve formation of various intermediates, as illustrated in **Figure 2.2**. The intermediates I – III are considered to lead to olefins, while structures IV – V have been proposed as species leading to the fully hydrogenated products. The compound V is valid only for mono-substituted alkynes. The intermediate VI arises from olefin adsorption, leading also to alkane [14, 22].

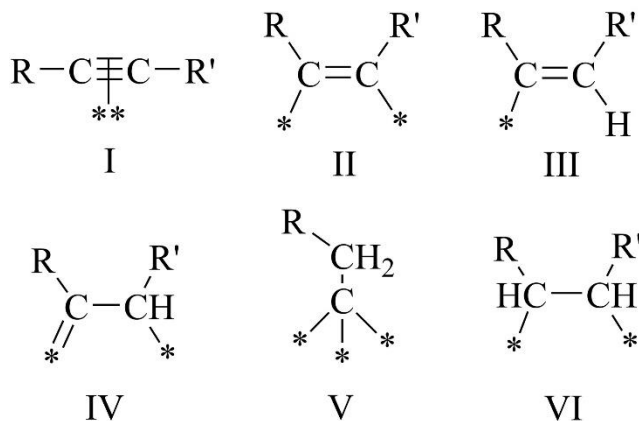


Figure 2.2. Possible reactive intermediates during hydrogenation of a molecule containing a $\text{C}\equiv\text{C}$ bond and other functionalities (R, R') on the catalyst surface (*).

Adapted from Rajaram *et al.* [14] with permission of Elsevier.

The reaction between alkynol and H_2 on the catalyst surface proceeds through a successive addition of dissociated hydrogen atoms to the substrate, as was described by Horiuti and Polanyi [23]. Provided the reaction takes place in a kinetic regime, it can be limited by (i) dissociative adsorption of H_2 , (ii) bonding of the first hydrogen atom with the substrate molecule or (iii) addition of the second hydrogen to the adsorbed substrate [24]. The rate-limiting step in heterogeneous catalysis can be controlled by various factors, such as activation energies of the corresponding transformation stages or a surface concentration of the intermediates linked to their bulk concentrations [25]. There is a lack of the agreement between various theoretical calculations reported in the literature, pointing to the addition of the first [26] or the second [27, 28] hydrogen atom as the most energy demanding reaction step. Nevertheless, namely the addition of the second hydrogen to the adsorbed alkyne was

identified in various reviews as a rate limiting step [29, 30] and was successfully used to explain the experimental results obtained in the hydrogenation of alkynes in general [31, 32] and alkynols in particular [21, 33].

2.1.2 Selective Hydrogenation of Functionalized Nitroarenes

Functionalized anilines are high value chemicals with multiple industrial applications (*e.g.* production of pharmaceuticals, polymers) [34]. They are conventionally produced by selective catalytic hydrogenation of functionalized nitroarenes, where the crucial issue is to avoid cleavage or hydrogenation of other reducible groups [35, 36]. Particularly, nitrostyrene (NS) reduction is very challenging since C=C functionality is one the most reactive bonds in metal-catalyzed hydrogenations [37]. Possible reaction pathways associated with the catalytic reduction of 3-NS are presented in **Figure 2.3**. The reaction 1 involves NO₂-group reduction (*via* 3-vinylnitrosobenzene and 3-vinylhydroxylamine intermediates) leading to 3-VA, which could be further transformed to undesired 3-ethylaniline (3-EA; reaction 2). In the reaction 3, 3-NS is hydrogenated to 3-ethylnitrobenzene (3-ENB), which can be converted to 3-EA (reaction 4). Additionally, the 3-NS → 3-VA transformation can proceed through the formation of condensation products (CP): azoxy-, azo-, hydrazoarenes (reactions 5 – 6). Reduction of vinyl groups in the condensation products is not considered in the scheme for the sake of simplicity. It is clear that the formation of condensation intermediates is also possible within the step 4, since it is not elementary.

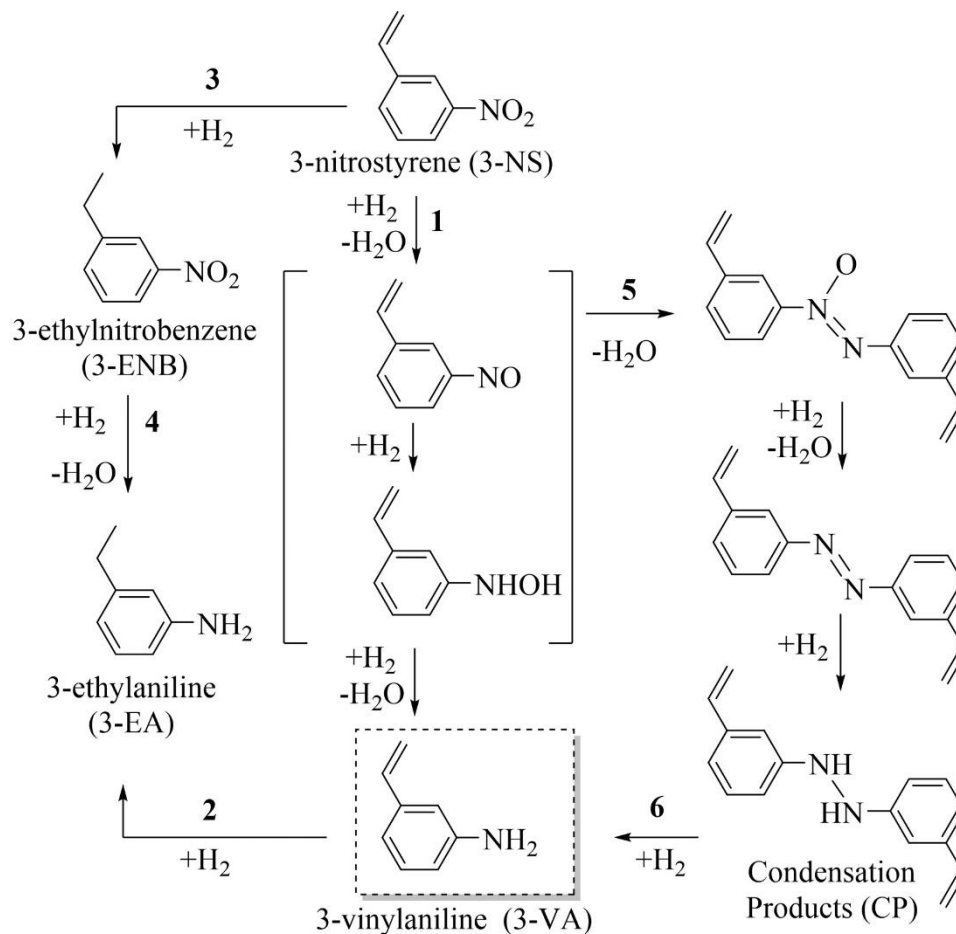


Figure 2.3. Simplified reaction scheme associated with the nitrostyrene hydrogenation.

Highly selective catalysts (VA yields up to 100%) based on Au [38, 39], Ag [40, 41], Mo [42] were developed for NS hydrogenation. However, they exhibit low activity compared to other metals [38] and, therefore, demand more harsh reaction conditions [35]. On the other hand, Pt catalysts commonly demonstrate a *ca.* 20-fold higher activity than Au in NS hydrogenation [38, 43]. Typically, these catalysts require an addition of modifiers (H₃PO₂, N(CH₃)₄Cl, FeCl₂) to the reaction mixture to achieve *ca.* 95% yield to VA [3, 44, 45].

The classical adsorption-reaction-desorption mechanism suggests that the rate of catalytic hydrogenation depends on the strength of (functionalized) nitroarene adsorption and on the rate of the slowest step in a catalytic cycle [37]. The catalyst selectivity towards corresponding (functionalized) aniline is influenced by the relative impact of these factors. For example, for two competing functional groups, the group that is adsorbed more strongly on the metal surface will hinder the access to another functionality. In the case of a NS molecule, the close adsorption energies of NO_2 - and C=C-groups on the pure metal surface [46] result in an activation of both functionalities and, therefore, in a low VA selectivity. Moreover, it is generally assumed that nitroarene molecules adsorb in a “flat-lying” geometry with the molecular plane parallel to the metal surface [37, 46, 47]. This means that on a flat surface other substituents in the benzene ring are also activated and subjected to transformations. The problem of low selectivity can be solved by a careful catalyst design through the optimization of its structural and electronic properties.

2.2 Catalyst Optimization for Hydrogenation Reactions

Development of catalysts for selective hydrogenation has been in a research focus for many years. There is, however, a long-standing interest on this topic and an intense research activity is still continuing to provide better understanding of the factors, which are decisive in governing selectivities [22]. The key to a successful catalyst design is to find a correlation between characteristics of the active phase and

the catalytic performance. Once the correlation is found, a modification of catalyst properties for a particular reaction becomes possible.

2.2.1 Effect of Metal Particle Size on Catalyst Performance

In terms of structural characteristics that control catalytic performance in hydrogenations, a metal NP structure has been identified as critical, *i.e.* these reactions are known to be structure-sensitive [19, 48]. Variations in the metal particle size can induce variations in the specific reaction rate, expressed per metal surface atom – a turnover frequency (*TOF*) [49]. In structure-sensitive reactions, an *increase* or *decrease* of *TOF* with the particle size is referred to as *antipathetic* or *sympathetic structure sensitivity*, respectively [50] (**Figure 2.4 (I)**). This is correlated with a change in the relative proportions of surface atoms (*i.e.* vertex, edge, plane) with different reactivities, affected by the metal dispersion [51, 52] (**Figure 2.4 (II)**). A comprehensive set of models became available to provide a framework for assessing the geometry of the surfaces of small particles. The calculations performed by van Hardeveld and Hartog [53] on the variation in the populations of specific surface atoms with a particle size increase represent a valuable model that facilitates an interpretation of the size effect on catalyst activity. It has been frequently invoked to describe the reaction structure sensitivity in various studies [19, 54, 55].

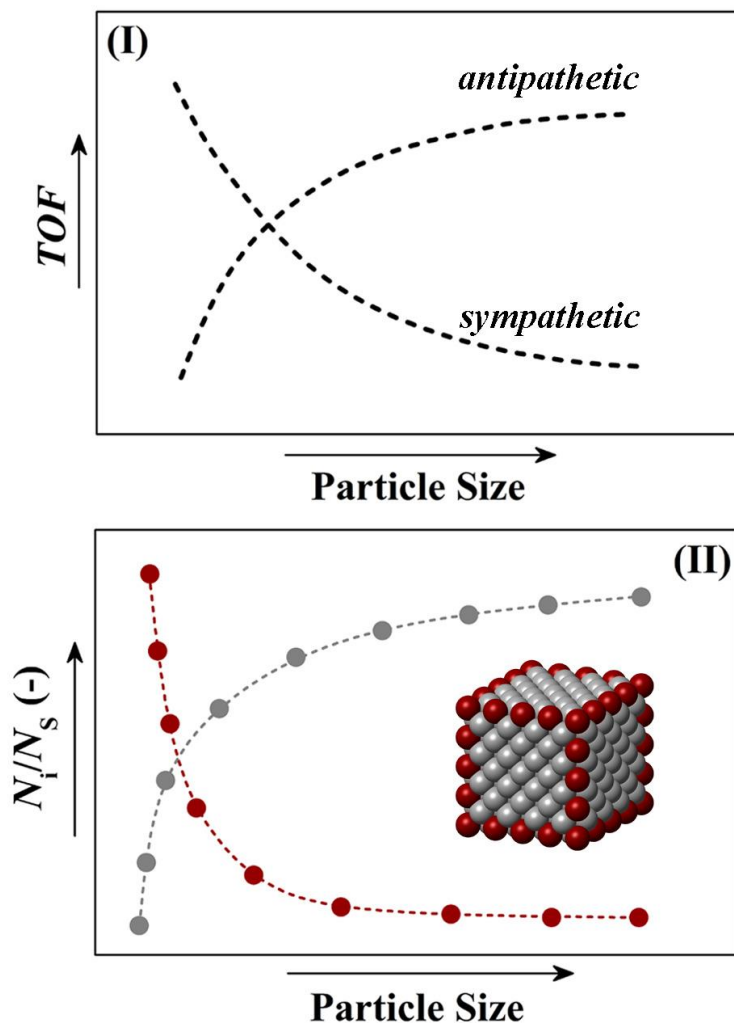


Figure 2.4. Possible forms of reaction structure sensitivity depending on particle size **(I)** and variation of the fraction of vertex/edge (●) and plane (●) surface atoms (N_i/N_s) as a function of particle size **(II)**.

The distinct catalytic activity/selectivity response of NPs with different morphologies is often linked to geometric and/or electronic factors [30]. The former effect plays an important role when the reaction requires an ensemble of surface atoms constituting an active center. For example, in $C\equiv C$ hydrogenation, a specific

group of surface atoms is needed for π - or di- σ -adsorbed flat-lying alkynes (**Figure 2.2**), which are the precursors for alkene formation [22]. The probability of finding large ensembles of Pd atoms on the surface increases with the NP size. Alternatively, the geometric nature of the size effect has a significant influence on Pd-catalyzed $C\equiv C$ hydrogenation where the formation of unselective β -PdH phase leading to over-hydrogenated products is favored in large NPs [56]. Aramendia *et al.* [57], taking the hydrodechlorination of chlorobenzene over Pd NPs (2 – 16 nm) supported on $AlPO_4$, reported reaction rates up to an order of magnitude higher over bigger Pd particles and attributed this to the contribution of β -Pd hydride as an alternative source of active hydrogen at lower dispersions.

Regarding the electronic nature of structure sensitivity, there is much evidence indicating that a very small metal particle has a different band structure compared to that of bulk metal, the former being more electron deficient [58]. The X-ray photoelectron spectroscopy (XPS) measurements of Pd and Pt revealed a change in binding energy for NPs with the sizes between 1 and 5 nm suggesting a change of the NP electronic structure [50]. Chemisorption of electron-rich substrates (*e.g.* alkynes, nitroarenes) on such NPs is, therefore, affected [22]. This is supported by calculated adsorption energies that showed higher values over smaller NPs (<3 nm) [59]. Additionally, the electronic nature of structure sensitivity can have an indirect influence when, for example, a shift of electrons from the metal particle to the support may cause a larger electron deficiency for smaller particles [30].

It is important to stress that the geometric and electronic effects cannot often be separated as independent parameters. For instance, an increase in the metal particle size results in an electron bandwidth increase and lower binding energies of core electrons, but the nature of the exposed planes and the topology of surface sites change as well [60].

Regarding the studies of structure sensitivity in hydrogenation of alkynes and alkynols, some consensus emerges from the available literature that points to an increasing *TOF* for Pd NPs in the size range of 4 \rightarrow 10 nm (antipathetic structure sensitivity) [51] and invariant activity (structure insensitivity) [19, 51] for larger (>10 nm) metal crystallites. Nonetheless, this conclusion is by no means irrefutable. Telkar *et al.* [61] studying the hydrogenation of 2-butyne-1,4-diol over unsupported Pd NPs (5 – 7 nm) reported the highest activity over the smallest metal crystallites. Boitiaux *et al.* [62] investigating hydrogenation of butyne over Pd/Al₂O₃ (0.4 – 4.2 nm) reported a 10-fold increase in activity over the larger particles. Mastalir *et al.* [63] examining hydrogenation of 4-octyne over Pd NPs (1.5, 3.0 and 6.2 nm) showed a decreased *TOF* for bigger particles while the highest *TOF* in hydrogenation of phenylacetylene was achieved over 3 nm-sized nanocrystals.

The studies of particle size effects in hydrogenation of functionalized nitroarenes over Au-, Ag- and Pt-based catalysts suggest both sympathetic and antipathetic structure sensitivities depending on the active metal used. The catalytic activity of Au and Ag in hydrogenation reactions is significantly lower as compared to the conventional transition metals (*e.g.* Pt, Pd), a response being attributed to a less

effective activation/dissociation of H_2 [64]. Therefore, low coordination (vertex, edge) surface sites are required for the Au- and Ag-catalyzed reactions. In this case, an increase in *TOF* over catalysts with higher metal dispersions was attributed to the abundance of low-coordinated atoms on the surface of small particles [40, 65]. The antipathetic structure sensitivity of functionalized nitroarenes hydrogenation over supported Pt catalysts was ascribed to a distinct adsorption-activation mechanism for highly dispersed (<2 nm) *vs.* larger (≥ 3 nm) Pt NPs [66]. Alternatively, increased *TOFs* were explained by a stabilization of negatively charged reaction intermediates on the surface of larger Pt particles [47]. Studying the effect of Pt NP size on the VA selectivity in NS hydrogenation, Corma *et al.* [38] came to a conclusion that hydrogenation of the C=C-group in a NS molecule is significantly more structure sensitive than that of the NO_2 -group. Therefore, it is possible to increase the VA production by decreasing the Pt NP size, which results in a lower catalyst activity towards C=C hydrogenation, while maintaining the activity of the NO_2 -group reduction.

The understanding of the aforementioned size-effects could be used for rational catalyst design for structure-sensitive reactions.

2.2.2 Active Phase Modification with Second Metal

Controlled modifications in metal particle size have been identified as effective means of influencing catalytic activity/selectivity [19]. Alternatively, catalyst modification by introducing another component, *e.g.* a second metal, allows for the fine-tuning of its catalytic properties [11]. Bimetallic NPs are known to have an

improved catalytic performance for hydrogenations relative to the monometallic counter partners [67]. The synergistic catalytic effect over bimetallic NPs could be ascribed to the following main aspects that influence the activity/selectivity response [11, 68]:

- structural changes of the active metal surface that can affect the adsorption mode of the reacting molecules;
- blocking of non-selective surface sites;
- electronic interaction between the active metal and the modifier that influences the adsorption strength of the substrates and products on the catalyst surface;
- in the case of Pd-based catalysts, the incorporation of the modifier can suppress (or diminish) the formation of the β -PdH phase, deemed to be unselective in $C\equiv C$ hydrogenations;
- indirect improvement of the catalyst performance, *e.g.*, by providing thermal, mechanical, chemical stability or enhancing the dispersion of NPs.

It should be noted that a combination of these factors could affect the catalytic response of a bimetallic catalyst. Moreover, the impact of each factor on catalyst characteristics, such as, for instance, their electronic properties, depends on the nature of the metals. Pd atoms have high vacancies in the *d*-states being receptive to chemisorption of $C\equiv C$ and $C=C$ groups that act as electron donors [69]. A Pd modification with Ag or Cu induces a higher Pd *d*-band electron density resulting in a weaker adsorption strength of unsaturated hydrocarbon bonds [60, 69].

A prominent example of modified catalytic system is Pd/CaCO₃ treated by Pb, known as a Lindlar catalyst [70]. It is industrially applied for C≡C hydrogenation, where the addition of Pb limits the predisposition of Pd to form β-PdH phases, hinders alkene adsorption and, therefore, over-hydrogenation [18]. Particularly, in alkynol hydrogenation, up to 99% yields to the corresponding alkenols were achieved over the Lindlar catalyst. However, such high yields can be attained only after the addition of quinoline (another promoter in Lindlar's recipe) to the reaction mixture [14]. Other Pd-based bimetallic systems modified with Ag⁰ [71], Cu⁰ [72, 73], and Zn⁰ [17] showed up to 99% selectivity to the target alkenol. A prominent example is a bimetallic catalyst for NS hydrogenation developed by Serna *et al.* [43] by combining Au with Pt. The resulted Au-Pt/TiO₂ showed 93% VA selectivity ($X_{NS} = 95\%$).

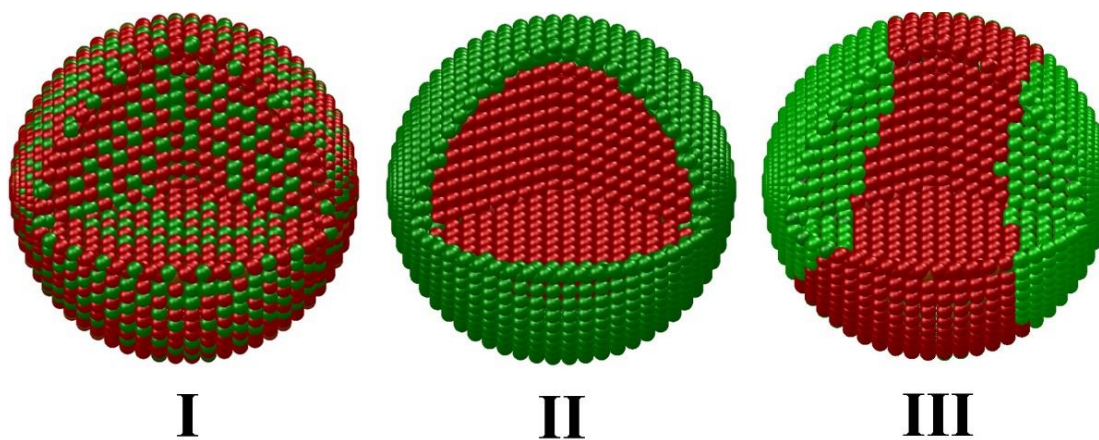


Figure 2.5. Schematic representation of possible structures of bimetallic NPs.

In addition to the metals' nature, the physical and chemical characteristics of bimetallic NPs strongly depend on the distribution of both components within the crystal nanostructure [68, 74, 75] which, in turn, impacts on the catalytic properties

[76]. Three main patterns can be identified (**Figure 2.5**): mixed alloy (**I**), core-shell (**II**), and cluster-in-cluster (**III**).

A real structure of bimetallic NPs is determined by a number of parameters [67, 76]:

- Relative bonding strength between the similar (M_1-M_1 , M_2-M_2) and different (M_1-M_2) metal atoms. A strong M_1-M_2 bonding favors mixing.
- Surface energies of bulk elements. The element with the lowest surface energy tends to segregate to the surface.
- Relative atomic sizes. Smaller atoms tend to occupy the more sterically confined core.
- Charge transfer. An electron transfer from less to more electronegative elements favors mixing.
- Binding strength of surface ligands (surfactants) or gases. The NP surface is saturated with the element that binds more strongly the ligands or adsorbed gas molecules.
- NPs preparation method. Simultaneous reduction of two metals can lead to an alloy structure, while deposition/reduction of metal M_2 on a particle containing sole element M_1 results in a core-shell structure. In the latter case, the first metal serves as a catalyst for reduction of the second metal.

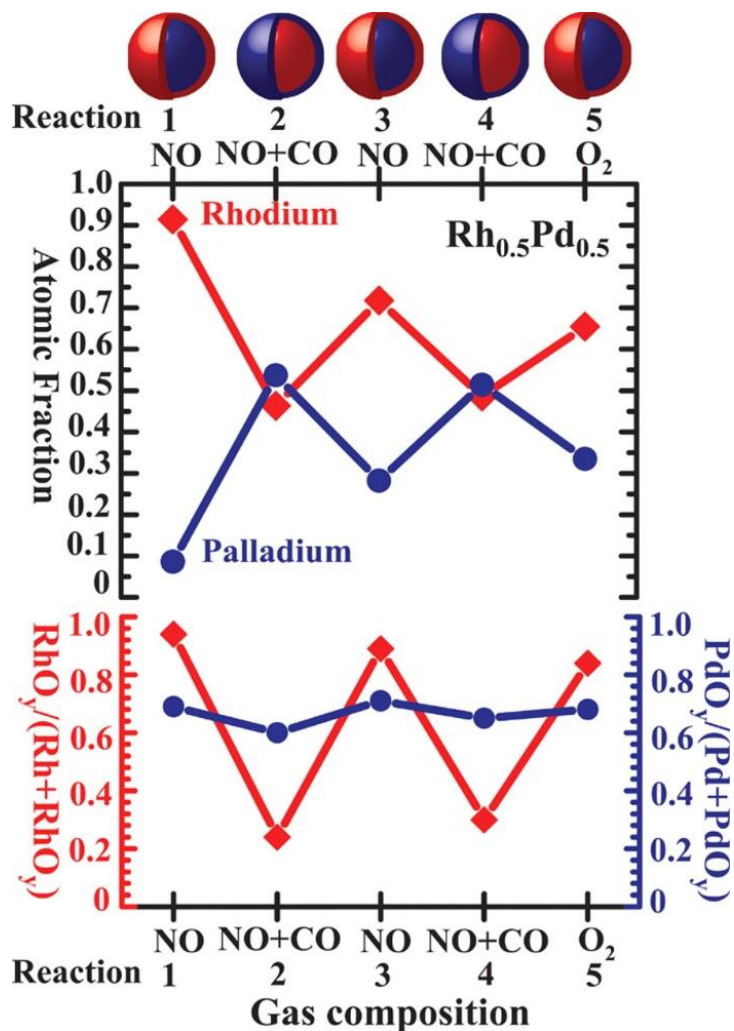


Figure 2.6. (Top) Evolution of Rh ($\text{Rh}^0 + \text{Rh}^{2y+}$) and Pd ($\text{Pd}^0 + \text{Pd}^{2y+}$) atomic fractions in the $\text{Rh}_{0.5}\text{Pd}_{0.5}$ NPs oxidizing (NO or O₂) and catalytic (NO or O₂) conditions denoted in the x-axis. **(Bottom)** Evolution of the fraction of the oxidized Rh (left y-axis) and Pd atoms (right y-axis) in the examined region under the same reaction conditions as the top part of the figure. Schematic diagrams above the top of the figure show the reversible segregation of Rh and Pd under alternating oxidizing and catalytic conditions. Reproduced from Tao *et al.* [77], with permission of the American Association for the Advancement of Science.

It is important to note that the observed atomic arrangement for a particular bimetallic system depends on the combination of the outlined factors as well as reaction conditions. Tao *et al.* [77] demonstrated that bimetallic catalysts can undergo profound structural changes in response to reactive environments even at ambient pressures (**Figure 2.6**).

2.2.2 Role of Support in Catalytic Hydrogenation

A type of support can have a strong influence on the performance of a heterogeneous catalyst. Indeed, such effects were observed for selective hydrogenation of alkynols and functionalized nitroarenes [33, 37, 73, 78]. A role of support includes (but is not limited by) control of the NP size, metal distribution, particles stability (*e.g.* to agglomeration, leaching) and mass transfer effects [79]. The acid-base properties of a carrier can result in electron transfer from/to the metal phase giving rise to positively (electron-deficient) or negatively charged active metal particles [80]. Furthermore, the support facilitates both catalyst handling and separation from the reaction medium. In addition, it can also act as a co-catalyst or affect the catalyst performance through interactions with the active phase [46, 81]. Therefore, in the design of industrial catalysts for a given application, in addition to active phase morphology, the support effects need to be taken into consideration as a critical factor affecting the catalytic response [82].

When reducible oxides are used as carriers, their partial reduction leads to the established strong metal-support interactions (SMSI) [30, 56]. This induces active phase modifications manifested in (i) metal surface sites blocking *via* migration of

(partially) reduced oxide species from the support [38] and/or (ii) the formation of new bimetallic phase(s) (alloying) [83]. The latter form of interplay between metal and support is termed as “reactive metal-support interaction” [84] and results in the modified electronic and geometric properties of the active phase affecting the catalyst performance in the hydrogenation reactions [82, 85]. Recent studies have demonstrated high alkenol yields (>95%) during hydrogenation of alkynols over Pt/ZnO [31, 78]. The distinct catalytic behavior was ascribed to formation of a Pd-Zn alloy as a result of ZnO reduction in the presence of Pd NPs. The Pd-Zn phase imposes new adsorption properties on the catalyst, towards both H₂ and the organic substrate [86]. Pt and Au deposited on TiO₂ or Fe₂O₃ showed high VA selectivities ($S_{VA} = 93 - 99\%$) in NS hydrogenation ($X_{NS} = 95 - 99\%$) [38, 39, 43, 87]. When TiO₂ was used as a support, the increase in selectivity was attributed to the surface modification of active phase by partially reduced TiO_x species [38, 88].

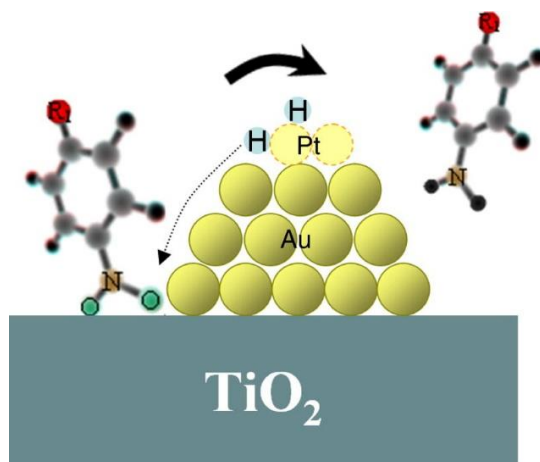


Figure 2.7. Schematic representation of nitroarenes hydrogenation over 1.5%Au@0.01%Pt/TiO₂ catalyst. Reproduced from Serna *et al.* [43] with permission of Elsevier.

In summary, there are many ways to improve the catalyst performance. Among them, the control of active metal characteristics through the optimization of particle size, modification with a second metal or choosing a proper support, represent powerful catalyst design tools. A striking example was shown by Serna *et al.* [43] in their approach of the NS hydrogenation catalyst development (**Figure 2.7**). The resulting 1.5%Au@0.01%Pt/TiO₂ contains small Au NPs rich in low-coordinated surface atoms to enhance the adsorption capacity of the catalyst. Incorporated Pt serves to increase the rate of H₂ dissociation while the SMSI between Au and TiO₂ result in the surface sites that selectively promote NS adsorption through the NO₂-group.

2.3 Size-Controlled Synthesis of Metal Nanoparticles

The control over NP morphology is of fundamental importance for catalysis [89]. It is often achieved through a regulating of the size and shape of NPs [19]. However, typical preparation techniques of supported catalysts lack the control over metal dispersion leading to a broad particle size distribution [51, 90]. Monodispersed NPs of noble metals are mostly prepared using colloidal methods [91-93]. They imply chemical reduction of a metal precursor in the presence of a stabilizing agent, which prevents aggregation and improves the chemical stability of the formed NPs. An advantage of this preparation technique is simple instrumentation design, easy process implementation and scale-up [94].

In general, a NP formation can be separated into two stages: nucleation and growth. Nuclei can be generated in two ways. A heterogeneous nucleation is carried out by adding preformed seed particles to the reactant mixture, while in a homogeneous nucleation, seeds are formed *in situ* [95, 96]. The latter is a more common synthetic strategy due to the practical ease of carrying out a one-pot reaction [94]. The mechanism of a homogeneous nucleation and growth was proposed by LaMer and Dinegar [97] and is schematically represented in **Figure 2.8**.

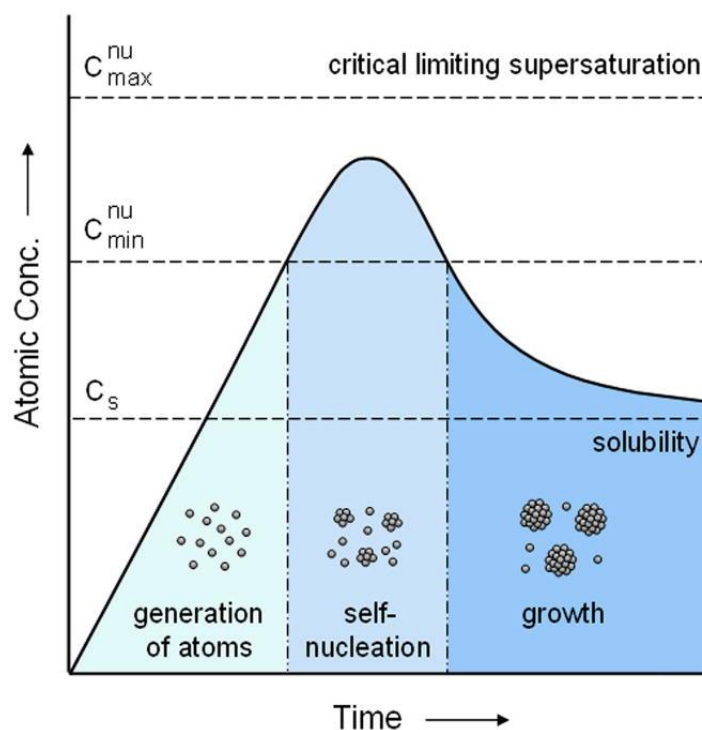


Figure 2.8. Schematic representation of atomic concentration as a function of time, illustrating the generation of atoms, nucleation, and subsequent growth.

Reproduced with permission of LaMer *et al.* [97] (copyright 1950 American Chemical Society) and Xia *et al.* [93] (copyright 2009 Wiley-VCH Verlag GmbH & Co).

According to the mechanism, the concentration of metal atoms steadily increases with time upon the precursor decomposition/reduction. Once the concentration of atoms reaches a critical point of supersaturation, atoms start to aggregate into small clusters (*i.e.*, nuclei) *via* self-nucleation [93]. The accelerated nuclei growth after the nucleation step results in a drop of the metal atoms concentration in the solution [98]. When the concentration drops below the critical level, the nucleation stops and the particles continue to grow by a molecular addition until an equilibrium concentration of precipitated species is reached [93].

Uniformity of the size distribution is achieved through a short nucleation period that generates all particles followed by a self-sharpening growth process [98]. The rate of metal precursor reduction is one of the most important parameters in controlling the nucleation events. When the reduction rate is high, more seeds will be formed in the nucleation stage. The number of seeds and the size of final NP are inversely proportional to each other, provided the amount of the precursor is the same [92]. The reduction kinetics can be controlled by various parameters, such as (i) the concentration and reduction potential of the metal precursor, (ii) strength and concentration of the reducing agent, (iii) reaction temperature and/or (iv) pH of the reaction mixture [51, 89, 99, 100].

Typical stabilizing agents used in colloidal methods to prevent NPs from agglomeration are linear and branched polymers, ligands, surfactants, polyelectrolytes, or ionic liquids [89, 91]. The common examples include cetyltrimethylammonium bromide [54, 75, 101], sodium di-2-ethylhexylsulfosuccinate [18, 102], N-dodecyl-N,N-dimethyl-3-amino-1-propan sulfonate [103], polyvinyl

alcohol [51, 104], poly(N-vinyl-2-pyrrolidone) (PVP) [105-108]. In addition to particles stabilization, they can affect the size of nanocrystals. PVP is the most widespread linear polymer used given its versatility and growth-directing capability. For instance, it was employed in a synthesis of monodispersed Pd NPs in the range of 2 – 7 nm [99, 109, 110]. With its use, the size control was also achieved for several Pd-based bimetallic systems, such as, Pd-Pt [111], Pd-Au [112], Pd-Ni [113], Pd-Cu [114], Pd-Ag [76].

2.4 Unconventional Catalyst Supports

For rational catalyst design, a catalyst support should satisfy multiple requirements. In addition to anchoring and stabilizing the active phase to avoid particles agglomeration [59], it can promote catalyst activity and/or selectivity, provide thermal stability, enhanced mass transfer, low pressure drop, high adsorption surface area and easy separation from the reaction mixture [18]. Conventional supports (powders, granules, extrudates) often do not comply with all these criteria. In the search of alternative catalytic systems, promising results have been obtained by using common support materials (*e.g.* metals, oxides, carbons) produced in unconventional forms (*e.g.* fibers, structured monoliths, filters, membranes, adsorbents). Successful examples of such supports include systems based on structured sinter metal fibers (SMF) and hypercross-linked polystyrene (HPS).

2.4.1 Sintered Metal Fibers

Sintered metal fibers are structured materials consisting of mechanically and chemically stable thin metal filaments ($d = 8 - 40 \text{ }\mu\text{m}$) [115-117]. Available commercially in the form of panels of different compositions, they possess regular structures with porosities ranging between 70 and 90%. As a support, they offer a series of benefits with respect to powder catalysts as a result of the open macrostructures leading to a low pressure drop during fluid-passage, narrow residence time distribution, enhanced mass and heat transfer and high thermoconductivity [118-122]. For catalytic applications, SMF can be readily modified in order to attain the required characteristics (*e.g.* surface area, acidity). They have been successfully coated with layers of metal oxides (ZnO , MgO , Al_2O_3), carbons or zeolites for use as catalyst supports in both gas- and liquid-phase reactions [33, 78, 116, 117, 123].

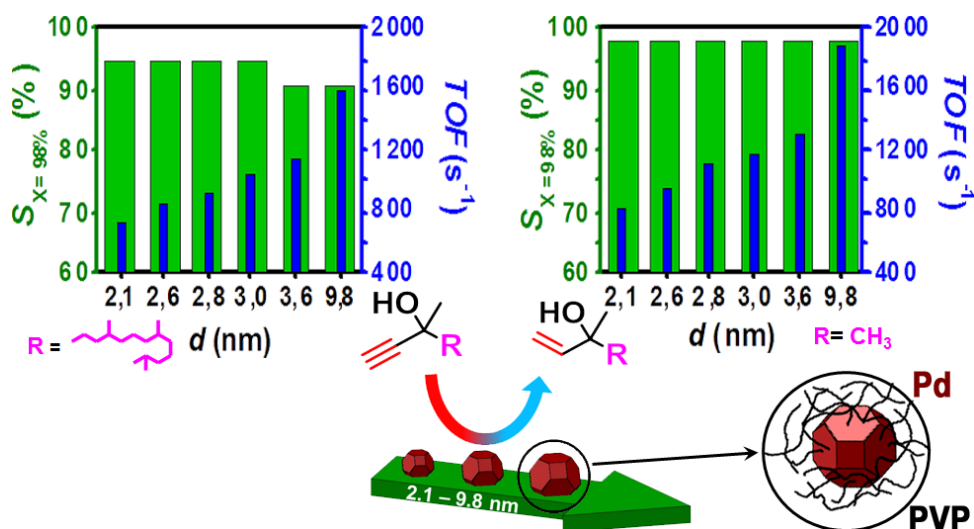
2.4.2 Hypercross-linked Polystyrene

Nanostructured polymeric matrices, such as hypercross-linked polystyrene (HPS), employed commonly as sorbent materials, show a great potential to be used as catalyst supports [66, 124]. They are characterized by a combination of high specific surface area ($\text{SSA}_{\text{HPS}} > 1000 \text{ m}^2 \text{ g}^{-1}$) and well-defined nanocavities (pores) of a controlled size [66]. If active metal NPs are formed within such nanoporous polymer matrix, their size is restricted by the pore size. Therefore, the HPS structure promotes the formation of well-distributed monodispersed NPs and prevents their

agglomeration even at high metal loadings. HPS has been used for controlled NPs formation of such metals as Co, Pt, Pd resulting in monodispersed particles in a size range of 2 – 35 nm [125-128]. HPS showed high performance as a catalyst support in liquid-phase hydrogenation of functionalized nitroarenes and acetylene alcohols [66, 125].

Chapter 3

Selective Hydrogenation of Alkynols: Size effect of Pd Nanoparticles



This chapter is based on the following publication: A. Yarulin, F. Cárdenas-Lizana, P. Abdulkin, L. Kiwi-Minsker, *J. Phys. Chem. C* 117 (2013), 13424-13434. Reproduced with permission of American Chemical Society (Copyright 2013).

Abstract

In this chapter, the effect of unsupported Pd NP size was studied in the selective $\text{C}\equiv\text{C}$ *semi*-hydrogenation of alkynols with different alkyl chains, *i.e.* C_{16} in dehydroisophytol (DIP) (to isophytol (IP)) *vs.* C_1 in 2-methyl-3-butyn-2-ol (MBY) (to 2-methyl-3-buten-2-ol (MBE)). The Pd NPs were synthesized *via* colloidal technique with PVP as stabilizing agent where a range of crystal sizes (2.1 – 9.8 nm; confirmed by HRTEM) was generated. Both reactions show *antipathetic structure sensitivity* consistent with higher specific activity (*TOF*) over larger Pd NPs where the structure sensitivity effect is more pronounced for NPs ≤ 3.0 nm. All the Pd NPs exhibit high ($\geq 88\%$) selectivity to the target alkenol product at almost complete (98%) conversion. Increased IP selectivity (S_{IP} ; $X_{\text{DIP}}=98\%$ *ca.* 95%) was observed over smaller (2.1– 3.0 nm) Pd NPs while *ca.* 98% selectivity to MBE (at $X_{\text{DIP}} = 98\%$) is obtained irrespective of particle size. The kinetic results were consistent with a Langmuir-Hinshelwood model. The observed Pd NPs size effect on catalytic response is ascribed to a contribution of Pd electronic surface modifications, fraction of Pd_{plane} active sites and the steric effects, which impact on alkynol/alkenol adsorption constants. The results obtained in this work provide a powerful tool of catalyst design for industrial applications.

3.1 Introduction

Pd particle size is critical for the control of catalyst performance in $\text{C}\equiv\text{C}$ hydrogenation [19, 48]. However, in conventional catalysts, because of the number of associated variables involved, it is difficult to establish an explicit link between catalytic properties and metal dispersion. Moreover, in spite of the number of studies devoted to this topic, the influence of metal dispersion over Pd NPs below 4 nm has not been investigated to a great extent and the reported literature is not only scant but also inconclusive. One of the reasons that can account for the lack of literature and discrepancy of results is the difficulty in the synthesis of highly dispersed unimodal metal nanocrystals. An effective strategy to circumvent this problem is the preparation of size-controlled unsupported polymer-stabilized metal NPs [51, 129].

The mechanism of $\text{C}\equiv\text{C}$ bond hydrogenation is still open to question and the Langmuir-Hinshelwood model has been used to account for the observed catalytic response [19, 78]. Pd NPs > 5 nm have been typically employed and we could not find any report where alkynol hydrogenation over highly dispersed (<4 nm) unsupported metal NPs has been subjected to kinetic and mechanistic assessment.

The aim of the study presented in this chapter is to extend the boundaries of size effect to the lower sizes for unsupported poly(N-vinyl-2-pyrrolidone) (PVP)-stabilized Pd NPs (from 10 \rightarrow 2 nm with a special emphasis on the less studied 2 – 3 nm metal NPs) in carbon-carbon triple bond alkynol hydrogenation. The transformation of 3,7,11,15-tetramethyl-1-hexadecyn-3-ol (dehydroisophytol, DIP) to isophytol (IP) has

been selected as a model reaction. We also address the impact of Pd-PVP NP size on the catalytic response for alkynols with different hydrocarbon tail length (C_{16} in DIP *vs.* C_1 in MBY). The alkenol products of DIP and MBY hydrogenations – IP and methylbutenol (MBE), respectively – are the key blocks in the synthesis of isoprenoids (vitamins A and E) [130-132]. In addition, a reaction kinetic model has been proposed to account for the observed phenomena.

3.2 Experimental

3.2.1 Materials

Poly(N-vinyl-2-pyrrolidone) (PVP) (Sigma Aldrich), $PdCl_2$ (Fluka; $\geq 99\%$), palladium (II) acetylacetonate (Sigma Aldrich; $\geq 95\%$), NaCl (Fluka; $\geq 99.5\%$), ethanol (Sigma Aldrich; 96%), L-ascorbic acid (Sigma Aldrich; 99%), 1,4-dioxane (AppliChem GmbH; $\geq 99.5\%$), ethylene glycol (AppliChem GmbH; $\geq 99.5\%$), NaOH (Reactolab), acetone (Sigma Aldrich; $\geq 90\%$), $NaBH_4$ (Sigma Aldrich; $\geq 98\%$), DIP (DSM Nutritional Products; $\geq 95\%$) and MBY (DSM Nutritional Products; $\geq 95\%$) were used as received without further purification. All the gases used in this study (H_2 and N_2) were of ultra-high purity (Carbagas; $\geq 99.99\%$).

3.2.2 Catalyst Preparation

A series of PVP-stabilized Pd NPs were prepared by colloidal technique. The Pd-PVP NPs preparation procedures are thoroughly described elsewhere [100, 110] but some features, pertinent to this work, are given below. The ***Pd-A*** sample was

synthesized as following: firstly a water + ethanol (water/ethanol = 3/2 v/v) solution (600 cm³) containing $1.0 \cdot 10^{-2}$ mol of PVP was heated up to 363 K. An aqueous solution of Na₂PdCl₄ ($5.0 \cdot 10^{-5}$ mol cm⁻³), prepared by dissolving PdCl₂ + NaCl in water (Pd/Na molar ratio = 0.5; $T = 363$ K), was then added to the mixture leading to the formation of a dark brown solution and kept at 363 K under stirring for 3 h. The **Pd-B** sample was prepared by stepwise growing method [99, 110] using *Pd-A* NPs as seeds. An aqueous Na₂PdCl₄ solution ($2.5 \cdot 10^{-5}$ mol cm⁻³, preparation procedure as described above) was added to a hot (363 K) water + ethanol (3/2 v/v) solution (600 cm³) containing $2.5 \cdot 10^{-4}$ mol of *Pd-A* and $5.0 \cdot 10^{-3}$ mol of PVP (PVP/Pd molar ratio = 10) and kept under heating and stirring for 3 h. **Pd-C** was synthesized with palladium (II) acetylacetonate ($1.0 \cdot 10^{-3}$ mol) as Pd precursor. The metal precursor was dissolved in 1,4-dioxane (50 cm³) under Ar atmosphere. A solution of PVP ($10.0 \cdot 10^{-3}$ mol) in ethylene glycol (120 cm³) was then added to the metal precursor-containing solution. The mixture was cooled down (273 K) and the pH was adjusted (*ca.* 10) by dropwise addition of a NaOH + deionized water solution ($5.0 \cdot 10^{-3}$ mol cm⁻³). The solution was kept under constant stirring (*ca.* 500 rpm) at 413 K for 2 h. **Pd-D** was prepared by dissolving of palladium (II) acetylacetonate ($1.0 \cdot 10^{-3}$ mol) and PVP ($1.0 \cdot 10^{-2}$ mol) in ethanol (120 cm³) under Ar atmosphere. NaBH₄ ($2.0 \cdot 10^{-3}$ mol) was subsequently added and the solution was kept under constant stirring (*ca.* 500 rpm) at room temperature for 9 h. The **Pd-E** sample was synthesized by adding an aqueous Na₂PdCl₄ solution ($1.0 \cdot 10^{-4}$ mol cm⁻³) to a *pre*-heated (363 K) aqueous mixture (30 cm³) containing ascorbic acid ($8.5 \cdot 10^{-4}$ mol) and PVP ($5.0 \cdot 10^{-3}$ mol; PVP/Pd molar ratio = 10). The mixture was kept under stirring at 363 K for 3 h. **Pd-F** sample was prepared using

the similar procedure to that described for *Pd-A* but in a 30 cm³ (instead of 600 cm³) water/ethanol (3/2 v/v) solution. All the methodologies described above resulted in a dark colloidal solution, which indicates the formation of Pd⁰ NPs [92].

Prior to use in catalysis, the Pd NPs were cleaned-up from the excess of stabilizer *via* flocculation with acetone (1/3 v/v solution/acetone), rinsed thoroughly with acetone and redispersed in water attaining *ca.* 0.4% Pd in the final solution.

3.2.3 Catalyst Characterization

The Pd content in the synthesized colloidal solutions was measured by atomic absorption spectroscopy (AAS) using a Shimadzu AA-6650 spectrometer with an air-acetylene flame from the diluted solutions in "aqua regia" (1/3 v/v HNO₃/HCl).

Pd NP size was evaluated by transmission electron microscopy (TEM) using a CM20 FEG (Philips) unit operated at an accelerating voltage of 200 kV using Gatan Digital Micrograph 3.4 for data treatment. The specimens were prepared by dispersion in ethanol and deposited on a holey carbon/Cu grid (300 Mesh). Up to 500 individual Pd metal particles were counted for each catalyst and the mean metal diameter (d) was calculated from:

$$d \text{ (nm)} = \frac{\sum_i n_i d_i}{\sum_i n_i} \quad (3.1)$$

3.2.4 Catalytic Hydrogenation.

Liquid phase hydrogenation reactions ($P_{\text{H}_2} = 4$ bar; $T = 313 - 353$ K) were carried out in a commercial semi-batch stirred stainless steel reactor (150 cm³ autoclave, Büchi AG, Uster, Switzerland) equipped with a pressure controlled H₂ supply system. Hydrogen consumption in the reactor vessel was monitored *on-line* with a press gas flow controller (BPC-6002, Büchi, Switzerland) and a stainless steel 6-blade disk turbine impeller (equipped with a self-gassing hollow shaft) provided effective agitation, *i.e.* 2000 rpm, to ensure avoidance of external mass transfer limitations [31]. A bath circulator (HAAKE B-N3) was used to control the reaction temperature within ± 1 K using water as the thermal medium. Hydrogenations of DIP and MBY were carried out with ethanol as a solvent. At the beginning of each experiment, an ethanol-alkynol solution ($C_{\text{alkynol}} = 0.34 \cdot 10^{-3}$ mol cm⁻³, $V_{\text{tot}} = 80$ cm³, $Pd_{\text{tot}}/DIP \sim 7 \cdot 10^{-6}$) was charged into the reactor and flushed three times with N₂ under constant agitation. The temperature was set and allowed to stabilize (*ca.* 30 min). H₂ was then introduced and the system was pressurized ($P_{\text{H}_2} = 4$ bar, time $t = 0$ for reaction). In a series of blank tests, reactions carried out in the absence of catalyst did not result in any measurable conversion.

A *non-invasive* liquid sampling system *via* syringe allowed a controlled removal of aliquots (≤ 0.3 cm³) from the reactor. Repeated reaction runs with the same batch of catalyst delivered conversion and selectivity values that were reproducible to within $\pm 0.4\%$.

The composition of the reaction mixture was analyzed using a Perkin-Elmer Auto System XL chromatograph equipped with a programmed split/splitless injector and a flame ionization detector employing a Stabilwax (Cross-bond Carbowax-PEG, Restek, USA) capillary column (i.d. = 0.32 mm, length = 30 m, film thickness = 0.25 μm). Data acquisition/manipulation were performed using the TotalChrom Workstation Vers. 6.3.2. (for Windows) chromatography data system and the concentration of organic species in the bulk liquid phase were determined from the total mass balance in the reaction mixture. The conversion of (*e.g.*) DIP is defined as

$$X_{\text{DIP}}(\%) = \frac{C_{\text{DIP},0} - C_{\text{DIP}}}{C_{\text{DIP},0}} \cdot 100 \quad (3.2)$$

and selectivity with respect to (*e.g.*) IP as target product is given as

$$S_{\text{IP}}(\%) = \frac{C_{\text{IP}}}{C_{\text{DIP},0} - C_{\text{DIP}}} \cdot 100 \quad (3.3)$$

3.3 Results and Discussion

3.3.1 Characterization of Pd Nanoparticles

Monodispersed Pd NPs were synthesized by means of colloidal method using PVP as stabilizing agent. In this approach, the use of a reducing agent that allows a fast ($\text{Pd}^{2+} \rightarrow \text{Pd}^0$) reduction renders small Pd NPs with narrow size distribution [99]. PVP molecules attached to the Pd NPs *via* interaction between the carbonyl groups and the metal surface provide steric colloid stabilization [91, 133], *i.e.* Pd NPs agglomeration is avoided. In order to modify Pd crystal size in a control manner, two

methodologies were employed, *i.e.* (a) step-wise growing technique and (b) controlled modification of the reduction kinetics which is affected by (bI) the metal precursor solution concentration ($0.1 \cdot 10^{-5} - 1.7 \cdot 10^{-5}$ mol cm⁻³), (bII) reduction potential of the metal precursor, (bIII) the strength of the reducing agent ($\text{NaBH}_4 > \text{ascorbic acid} > \text{ethylene glycol} \approx \text{ethanol}$) and (bIV) reduction temperature. Both factors have been shown [92, 99, 100] to impact on Pd NPs size where lower metal concentrations/reduction potential and reducing agents with increase strength favor the formation of smaller NPs whereas stepwise growth mechanism allows a fine tuning of the Pd NPs size leading to the genesis of larger metal crystallites.

Representative TEM images (**I-II**) and NPs size distributions (**III**) associated with Pd-A (**a**) and Pd-E (**b**) as examples of Pd-PVP nanocatalysts with high and low dispersion, respectively, are presented in **Figure 3.1**. The TEM images show a quasi-spherical morphology that extends to the Pd NPs in all samples. Such shape is consistent with a cubo-octahedral crystal morphology, the most thermodynamically favorable crystal geometry [110]. The diffractogram patterns for isolated Pd NPs are included (as insets) in the high-resolution images (**II**) where the d -spacings (0.22/0.19 nm) are consistent with the (111) and (200) main planes of metallic Pd (JCPDS-ICDD reference standard 05-0681).

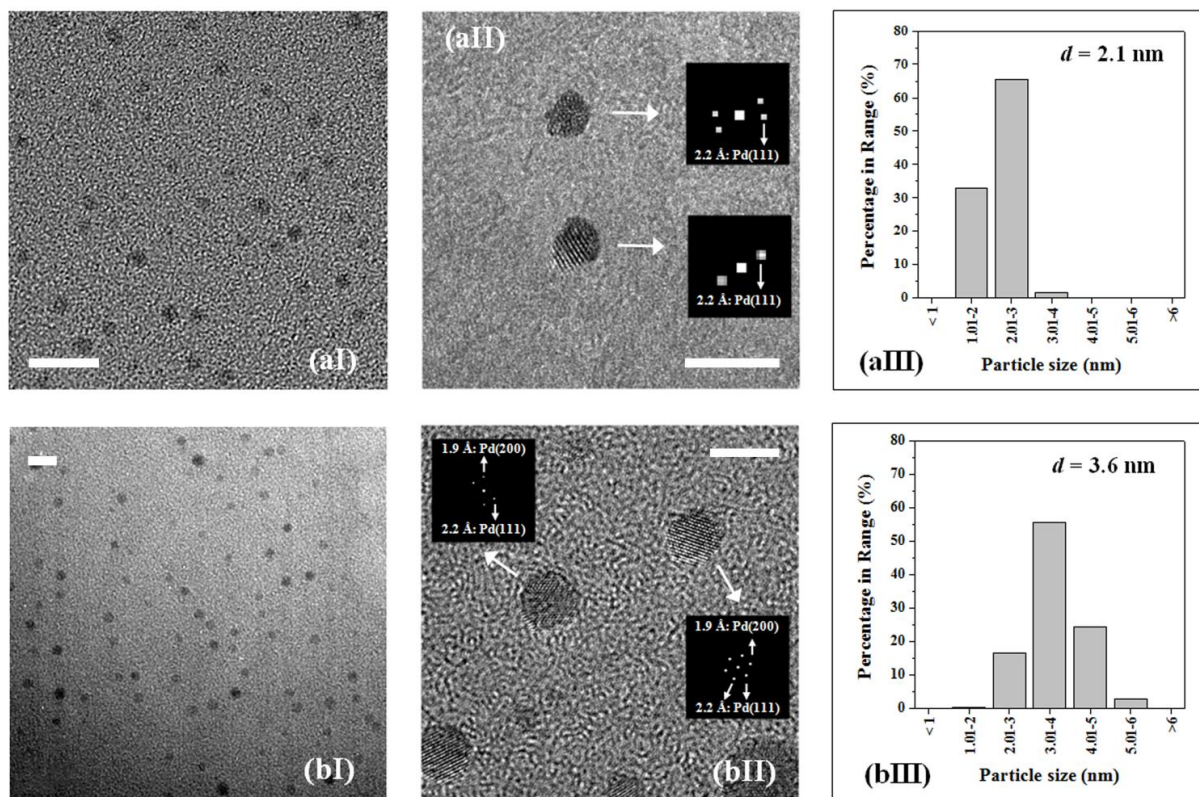


Figure 3.1. Representative **(I)** medium (scale bar = 10 nm) and **(II)** high (scale bar = 5 nm) magnification TEM images and **(III)** metal particle size distributions associated with PVP-stabilized Pd NPs in **(a)** Pd-A and **(b)** Pd-E. *Note:* diffractogram patterns and associated d -spacings and planes for single Pd particles in **(aII)** and **(bII)** are included as insets.

A concomitant decrease in Pd dispersion (from Pd-A to Pd-F; **Table 3.1**) and narrow NPs size distribution (**Figure 3.1(III)**) was proved by the TEM analyses. The average Pd NPs size fall within the 2.1 nm (Pd-A) to 9.8 nm (Pd-F) size range (dashed lines in **Tables 3.1, 3.2** and **3.4** separate “small” – $d \leq 3.0$ nm – and “large” – $d \geq 3.6$ nm – Pd NPs).

Table 3.1. Metal particle size (d), dispersion (D), fraction of Pd surface plane (x_{plane}) and edge (x_{edge}) atoms and ratio of PVP to total (Pd_{tot}) and surface (Pd_{surf}) Pd.

Sample	d (nm)	D_{a} (-)	$x_{\text{plane}}^{\text{b}}$ (-)	$x_{\text{edge}}^{\text{b}}$ (-)	PVP/Pd_{tot} (-)	PVP/Pd_{surf} (-)
Pd-A	2.1 ± 0.4	0.45	0.09	0.53	20	44
Pd-B (Pd-B1)	2.6 ± 0.3 (2.6 ± 0.3)	0.38 (0.38)	0.16 (0.16)	0.49 (0.49)	10 (20)	26 (53)
Pd-C	2.8 ± 0.7	0.35	0.18	0.48	10	28
Pd-D	3.0 ± 0.8	0.34	0.19	0.47	10	29
Pd-E	3.6 ± 0.3	0.28	0.29	0.42	10	36
Pd-F	9.8 ± 2.3	0.11	0.68	0.19	20	186

$$^{\text{a}}D = (Pd_{\text{surf}}/Pd_{\text{tot}})$$

$$^{\text{b}}x_i = (Pd_i/Pd_{\text{surf}})$$

It is important to stress that, despite the studies focused on structure sensitivity [61, 63] and/or reaction kinetics [21] of alkynol hydrogenation, to the best of our knowledge, this is the first report considering the dependence of activity/selectivity response on alkyl chain length over such small (≤ 3.0 nm) monodispersed unsupported Pd NPs. In this critical size range, changes in NP surface morphology are the most pronounced [59, 134] and, consequently, the highest impact of NP size on catalytic response can be expected. Variations in crystal dispersion result in changes in the relative fractions of surface atoms (x_i) [19], *i.e.* planes (Pd_{plane}) versus edges (Pd_{edge})

referred to the total amount of surface atoms (Pd_{surf}). Moreover, low [20, 135] or even lack [48, 51, 136] of activity of Pd_{edge} (relative to Pd_{plane}) surface atoms in alkyne hydrogenation has been reported elsewhere. The Pd dispersion (D) as well as Pd_{plane} and Pd_{edge} fractions (x_{plane} and x_{edge} respectively) shown in **Table 3.1** were determined using a *non*-ideal fcc cubo-octahedral model according to the method described by van Hardeveld and Hartog [53]. Surface statistics of the *non*-ideal fcc crystal model was previously applied for Pd NPs in the 6 – 31 nm size range with different shapes (*i.e.* cubes, cubo-octahedra and octahedra) [19]. In the present work, a similar (2-fold) increase in the x_{plane} was obtained with the NP size growth from 2.1 \rightarrow 3.0 nm and from 3.6 \rightarrow 9.8 nm. In contrast, the x_{edge} did not change significantly (*ca.* 0.50 ± 0.03) for Pd NPs in the 2.1 – 3.0 nm range while it decreased (2-fold) for larger NPs (from 3.6 nm to 9.8 nm).

3.3.2 Catalytic Response of PVP-Stabilized Pd Nanoparticles

The adsorbed PVP, which can remain on the Pd surface even after careful cleaning procedure, can poison the catalytically active sites [137, 138]. It has been established that even trace amounts (~ 10 ppm) [139] of stabilizing agent can induce electronic and steric modifications to the metal NPs that will result in changes of the activity/selectivity response in hydrogenation reactions [61, 138]. There is a minimum amount of PVP in the colloid solution at which the maximum PVP concentration on the surface of the Pd NPs is achieved and so, for solutions with increased PVP concentration, catalyst behavior is no longer dependent on the PVP/Pd ratio. This amount of PVP on the external NP surface (Pd_{surf}) is controlled by the crystal size, *i.e.*

a greater amount of PVP is required for smaller Pd NPs with higher metal dispersion. A direct comparison of catalytic response for Pd NPs with different sizes can only be established under conditions in which the PVP/Pd_{surf} ratio is sufficiently large or the amount of the stabilizer is high enough to saturate the entire available metal surface.

In this work, only two PVP/Pd_{tot} ratios were used ($PVP/Pd_{\text{tot}} = 10$ and 20; **Table 3.1**). Since Pd-B shows the lowest PVP/Pd_{surf} ratio among the catalysts tested ($PVP/Pd_{\text{surf}} = 26$), we compared the action of this catalyst with that of an additional sample with the same metal dispersion but increased (by 2-fold) PVP content, *i.e.* Pd-B1 ($PVP/Pd_{\text{tot}} = 20$, $PVP/Pd_{\text{surf}} = 53$). The results obtained over both catalysts did not show any measurable difference in terms of neither activity nor selectivity, which suggests that in both cases the amount of PVP adsorbed on the external Pd surface remains constant, *i.e.* the metal NP surface is saturated. This is in line with the findings of Hirai and Yakura [139] who established for Pd NPs in the range 2.0 – 2.5 nm PVP adsorption saturation at $PVP/Pd_{\text{tot}} > 4$. Moreover, Li *et al.* [110] studying the liquid-phase Suzuki reaction over 6 nm-sized Pd NPs reported similar catalytic response that was independent of the amount of PVP stabilizer ($PVP/Pd_{\text{tot}} = 2.5 - 20$). Since at the lowest PVP/Pd_{tot} ratio used in this study ($= 10$; see **Table 3.1**) the surface of Pd-B NPs (with the lowest PVP/Pd_{surf} ratio) is fully covered by PVP, we can conclude that the surface of the rest of the Pd NPs samples is also saturated and so, any difference in catalytic response can be linked to modifications in Pd NP size.

In order to rule out the possibility to aggregate during the reaction, a special experiment with the nanocatalyst of the highest dispersion (Pd-A, $d = 2.1 \pm 0.3$ nm)

has been carried out. A similar Pd-size *before* and *after* reaction was confirmed by TEM analysis.

3.3.3 Structure Sensitivity of Alkynol Hydrogenation

The synthesized monodispersed Pd NPs with different crystal size were tested in the liquid-phase DIP hydrogenation at 353 K where the only products detected were those from the *semi*- (target IP) and *full*-hydrogenation (hydroisophytol, HIP). The reaction network illustrating the hydrogenation pathways is presented in the simplified **Figure 3.2** where C \equiv C bond hydrogenation can proceed *via* stepwise (r_1 , r_3) and/or parallel (r_2) routes. The composition versus time profiles for Pd-A (**a**), Pd-B (**b**), Pd-E (**c**) and Pd-F (**d**), selected as representatives, are shown in **Figure 3.3 (I)** where the preferential formation of the target alkenol is in evidence.

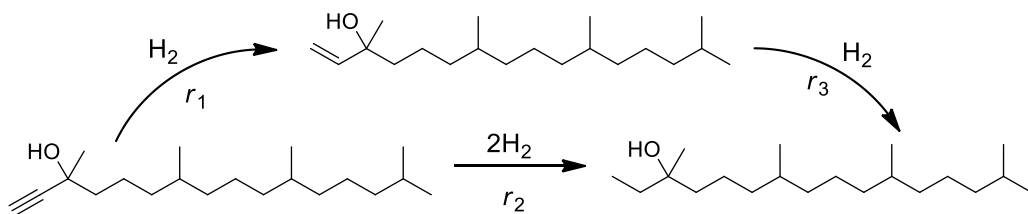


Figure 3.2. Reaction network associated with the hydrogenation of DIP to IP and HIP.

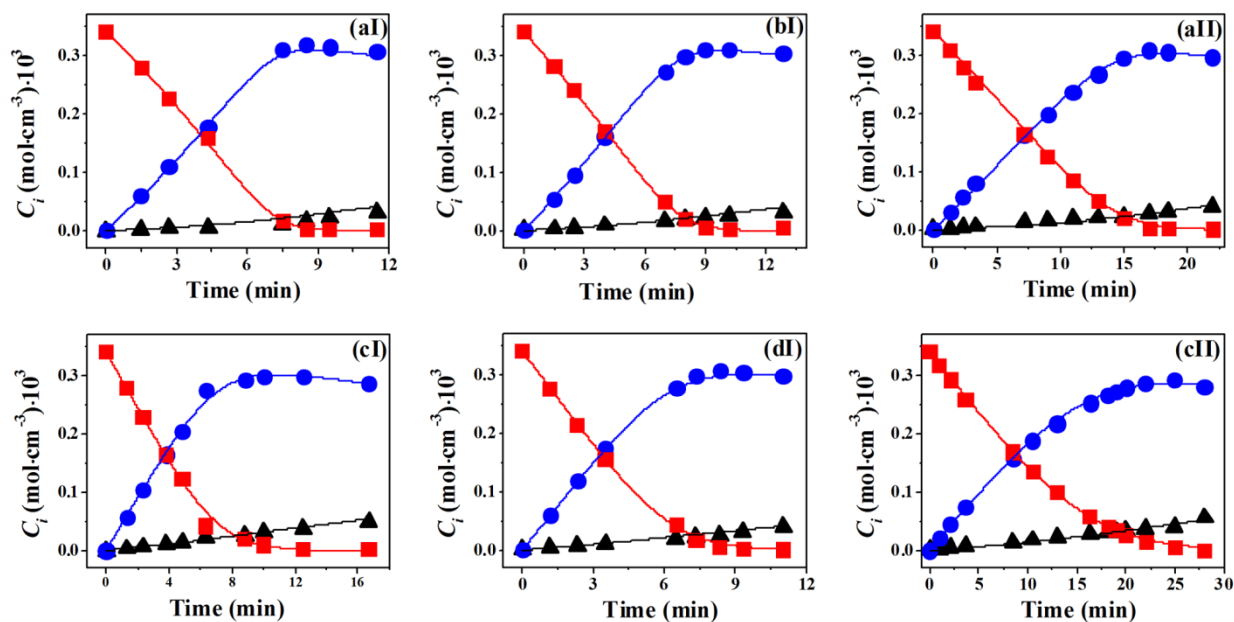


Figure 3.3. Temporal variation of DIP (■), IP (●), HIP (▲) concentration (C_i) for reaction over (a) Pd-A, (b) Pd-B, (c) Pd-E and (d) Pd-F at (I) 353 K and at (II) 333 K where symbols represent experimental data and solid lines are estimated from application of a Langmuir-Hinshelwood model, eqns 3.10 – 3.15. *Reaction*

conditions: $P_{H_2} = 4$ bar; Pd_{tot}/DIP molar ratio $\sim 7 \cdot 10^{-6}$.

Reaction pathway can be assessed from the results shown in **Figure 3.4**, where IP selectivity response ($S_{C=C}$) over Pd-A and Pd-E, as examples of "small" (≤ 3.0 nm) and "large" (≥ 3.6 nm) Pd-nanocatalysts, respectively, is presented as a function of DIP conversion ($X_{C=C}$). The data obtained in terms of $S_{C=C} < 100\%$ at low conversions suggest a parallel-consecutive reaction network, *i.e.* $C\equiv C \rightarrow C-C$ (r_2 in **Figure 3.2**) and $C\equiv C \rightarrow C=C \rightarrow C-C$ (r_1, r_3 in **Figure 3.2**).

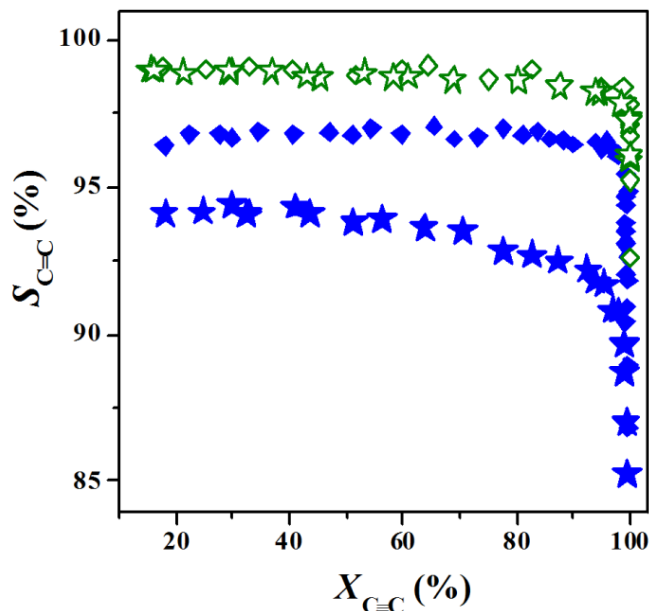


Figure 3.4. Selectivity to the IP (\blacklozenge, \star) and MBE (\blacklozenge, \star) target products ($S_{C=C}$) as a function of (DIP and MBY) alkynol conversion ($X_{C=C}$) for reaction over Pd-A ($\blacklozenge, \blacklozenge$) and Pd-E (\star, \star); Reaction conditions: $P_{H_2} = 4$ bar; $T = 353$ K; Pd/alkynol molar ratio $\sim 7 \cdot 10^{-6}$.

The favored *semi*-hydrogenation over all Pd nanocatalysts, regardless of the NP size, for metal crystallites in the range 2.1 – 9.8 nm is confirmed by the results in terms of IP selectivity at almost full conversion presented in **Table 3.2**. This can be associated with a higher $C\equiv C$ group (relative to $C=C$) adsorption strength on Pd [19, 60], *i.e.* stronger DIP adsorption on active Pd surface sites suppressing the readsorption of IP (as intermediate *semi*-hydrogenation product) on active centers which, in turn, inhibits further ($C=C \rightarrow C-C$) hydrogenation and formation of HIP [63]. It is worth noting that, in spite of the prevalent formation of the target IP, the results gathered in **Table 3.2** demonstrate that product selectivity is dependent on

metal dispersion where two clear alkenol selectivity tendencies over Pd NPs ≤ 3.0 and ≥ 3.6 nm are in evidence. Indeed, the results obtained are consistent with lower IP selectivity (91%) over larger (≥ 3.6 nm) Pd NPs while higher (and equivalent) selectivity to the target olefin product (95%) was recorded over the smaller (≤ 3.0 nm) Pd crystals.

Table 3.2. Pd nanoparticle size (d) and associated catalytic results in terms of turnover frequency (TOF) and selectivity to target IP (S_{IP}) and MBE (S_{MBE}) at $X_{C=C} = 98\%$ obtained in the hydrogenation of DIP and MBY, respectively, under equal conditions ($P_{H_2} = 4$ bar; $Pd_{tot}/alkynol$ molar ratio $\sim 7 \cdot 10^{-6}$).

Sample	d (nm)	DIP				MBY			
		$T = 353$ K		$T = 333$ K		$T = 353$ K		$T = 333$ K	
		S_{IP} (%)	TOF (s ⁻¹)	S_{IP} (%)	TOF (s ⁻¹)	S_{MBE} (%)	TOF (s ⁻¹)	S_{MBE} (%)	TOF (s ⁻¹)
Pd-A	2.1	95	714	90	386	98	813	97	449
Pd-B	2.6	95	839	-	-	98	945	-	-
Pd-C	2.8	95	908	-	-	98	1115	-	-
Pd-D	3.0	95	1059	-	-	98	1185	-	-
Pd-E	3.6	91	1152	88	572	98	1316	97	690
Pd-F	9.8	91	1577	-	-	98	1874	-	-

We can tentatively link the observed lower alkenol selectivity over larger Pd NPs to the action of Pd hydride. It is known that the formation of β -palladium hydride (β -PdH) involves room temperature H_2 diffusion ($P_{H_2} > 0.02$ bar) into the Pd crystallites to occupy available octahedral “holes” in the metal lattice [140]. The solubility isotherms and X-ray diffraction measurements clearly show the existence of a β -solution under normal conditions [141] which tends to disappear as the Pd crystal size decreases to attain a limiting value close to zero for NPs < 2.5 nm [142, 143]. Giving that β -PdH decomposes at $T \geq 365$ K for Pd crystals with associated $D \leq 25\%$ [56], in the present study (reaction temperatures in the range 333 – 353 K) the existence of β -Pd hydride in the Pd-E and Pd-F ($D \leq 28\%$; **Table 3.1**) catalysts can be expected. Although the specific role of β -PdH remains uncertain with both positive [144] and negative [18] effects in hydrogen mediated reactions, the general consensus that emerges from the open literature for alkyne hydrogenation is that unselective overhydrogenation of alkyne (to alkane) is favored by hydrogen saturated β -hydrides [60, 145]. It is important to stress that in this work 3.0 – 3.6 nm was found to be a critical NP size range and that higher IP product selectivity is obtained for smaller Pd crystal sizes. Tschan *et al.* [15], studying the same reaction over amorphous $Pd_{81}Si_{19}$ in supercritical CO_2 with various reaction modifiers (*i.e.* propyl disulfide, isopropyl disulfide, 2,2'-(ethylenedioxy)-diethanthiol) reported 100% selectivity to the IP product but we have achieved in this work a remarkable alkenol selectivity without reaction modifiers by variations in Pd NP size only.

An adequate comparison of catalytic activity for catalysts based on unsupported Pd colloids bearing different sizes is only meaningful in terms of initial (*i.e.* any contribution as a result of catalyst deactivation is negligible) intrinsic activity (per Pd surface atom; *TOF*). The initial DIP consumption rate ($-R_{\text{DIP},0}$) was determined from a linear regression of the temporal DIP concentration profiles where the *TOF* was estimated according to:

$$TOF \text{ (s}^{-1}\text{)} = \frac{-R_{\text{DIP},0}}{D} \quad (3.4)$$

The relationship between the *TOF* and mean Pd NP size for all the catalysts investigated in this work is presented in **Table 3.2**. The tendency of increasing activity (*TOF*) over larger Pd NPs (2.1 \rightarrow 9.8 nm) in the DIP hydrogenation at 353 K shows antipathetic structure sensitivity. These results are consistent with reported literature that has shown antipathetic structure sensitivity for C \equiv C hydrogenations of C₄ - C₈ molecules over NPs in the 4 – 31 nm size range [19, 48, 61, 146], but we show in here that this effect extends to long (C₁₆) hydrocarbon tail-containing molecules and metal NPs < 4 nm. It has been established [21, 52, 133] that one of the key factors determining catalytic activity is the type and amount of surface *Pd* atoms. The results presented in **Table 3.1** show that for particles in the 2.1 – 3.0 nm-size range the *Pd*_{edge} is the predominant type of surface atoms remaining almost constant (0.50 ± 0.03). Therefore, given the recorded tendency of increase *TOF* we conclude that this type of atoms cannot have a significant influence on the activity in this size range. In contrast, we can conclude that *Pd*_{plane} are the main active sites for the selective

partial alkynol (to alkenol) hydrogenation in the light of the parallel increase in activity with the proportion of Pd_{plane} (**Figure 3.5**).

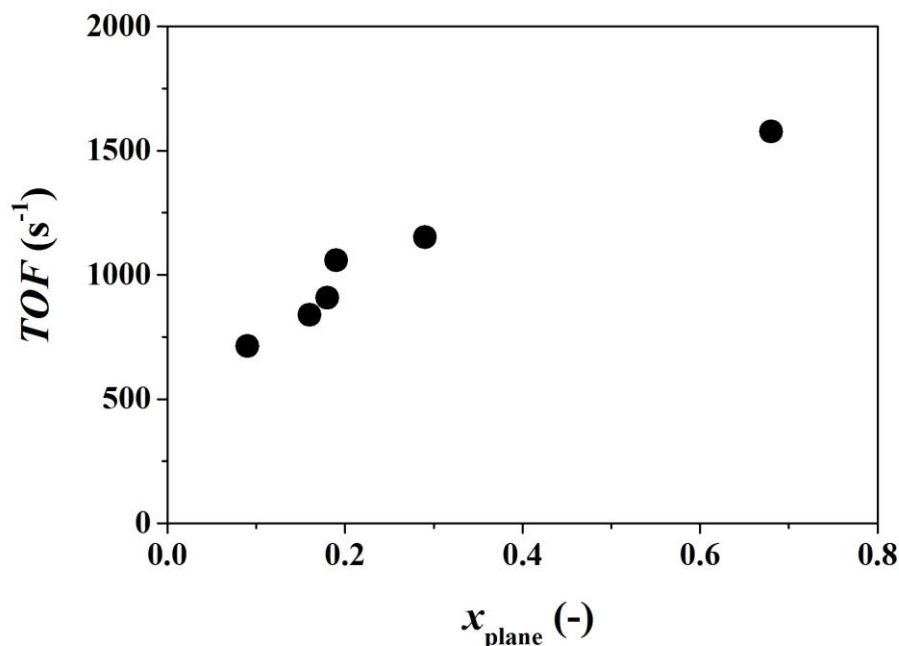


Figure 3.5. Catalyst turnover frequency (TOF) as a function of Pd_{plane} fraction (x_{plane}). *Reaction conditions:* $P_{H_2} = 4$ bar; $T = 353$ K; $Pd/alkynol$ molar ratio $\sim 7 \cdot 10^{-6}$.

It is worth noting that the results show the non-linear TOF dependence on x_{plane} when comparing Pd NPs below and above 3.6 nm. This is further supported by the two clear activity tendencies observed for particles ≤ 3.0 and ≥ 3.6 nm where the overall effect is significantly more pronounced for modifications in the smaller size range ($\Delta TOF/\Delta d \sim 383 \text{ s}^{-1} \text{ nm}^{-1}$ for $d \leq 3.0$ nm), relative to larger ($\Delta TOF/\Delta d \sim 69 \text{ s}^{-1} \text{ nm}^{-1}$ for $d \geq 3.6$ nm) Pd NPs. Indeed, for the smallest (2.1 nm) Pd NPs the fraction of Pd_{plane} is close to zero ($x_{\text{plane}} = 0.09$) and so, in this range, small modifications in size (with associated increase in the fraction of Pd_{plane}) will have a more severe impact on catalytic

response. It follows that for larger particles, *i.e.* $d \geq 3.6$ nm, there is already a significant number of Pd_{plane} and, therefore, upon the modifications in crystal size ($d = 3.6 \rightarrow 9.8$ nm; $x_{\text{plane}} = 0.29 \rightarrow 0.68$; **Table 3.1**) for reactions in which activity is controlled by this type of atoms, the effect will be less pronounced. Although the type and fraction of Pd_{surf} can impact directly on catalytic activity *via* differences in Pd NP size, there is also the possibility of a contribution through (i) variations in $\text{C}\equiv\text{C}/\text{C}=\text{C}$ adsorption energies rendering different ratio of adsorption constants on the same plane atoms, *i.e.* modifications in adsorption strength with particle size as a result of increased band width with metal particle [50, 59], and/or (ii) participation of $\beta\text{-PdH}$ [60, 145]. Our results show increased activity for larger Pd NPs which can be linked to higher amount of Pd_{plane} with possible electronic modifications, that impact on Pd electron density and $\text{C}\equiv\text{C}$ adsorption strength, and increase amount of hydrogen linked to $\beta\text{-PdH}$ formation on larger (≥ 3.6 nm) metal NPs.

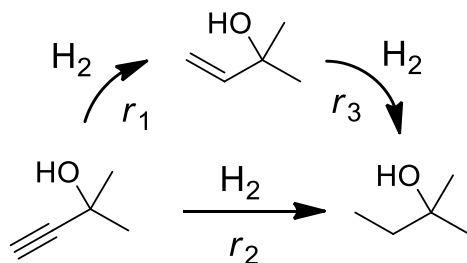


Figure 3.6. Reaction network associated with the hydrogenation of MBY to MBE and MBA.

The assessment of NP size effect was extended to an evaluation of hydrogenation of MBY with shorter alkyl chain under the same reaction conditions ($P_{\text{H}_2} = 4$ bar; $T = 353$ K). MBY hydrogenation generated solely the products resulting from partial (to MBE) and full (to 2-methyl-3-butan-2-ol (MBA)) hydrogenation. The reaction network illustrating the two main reaction pathways, *i.e.* consecutive (r_1 and r_3 with MBE as reaction intermediate) or parallel (r_2) reaction pathway is shown in **Figure 3.6**. It is important to stress that alkenol selectivity is challenging in MBY hydrogenation where, apart from the products of *semi*- and *full*-hydrogenation, oligomerization is also promoted [21, 78]. The formation of oligomers results in a permanent active site blockage and irreversible deactivation reducing drastically the catalyst life-time, a critical parameter to be considered for process scale-up. The formation of these undesired *by*-products was fully avoided over all the catalysts used in this work. This can be ascribed to the reaction conditions ($P_{\text{H}_2} = 4$ bar) as it has been demonstrated [21] that oligomerization is favored at low hydrogen partial pressures ($0.3 \text{ bar} \leq P_{\text{H}_2} \leq 1 \text{ bar}$).

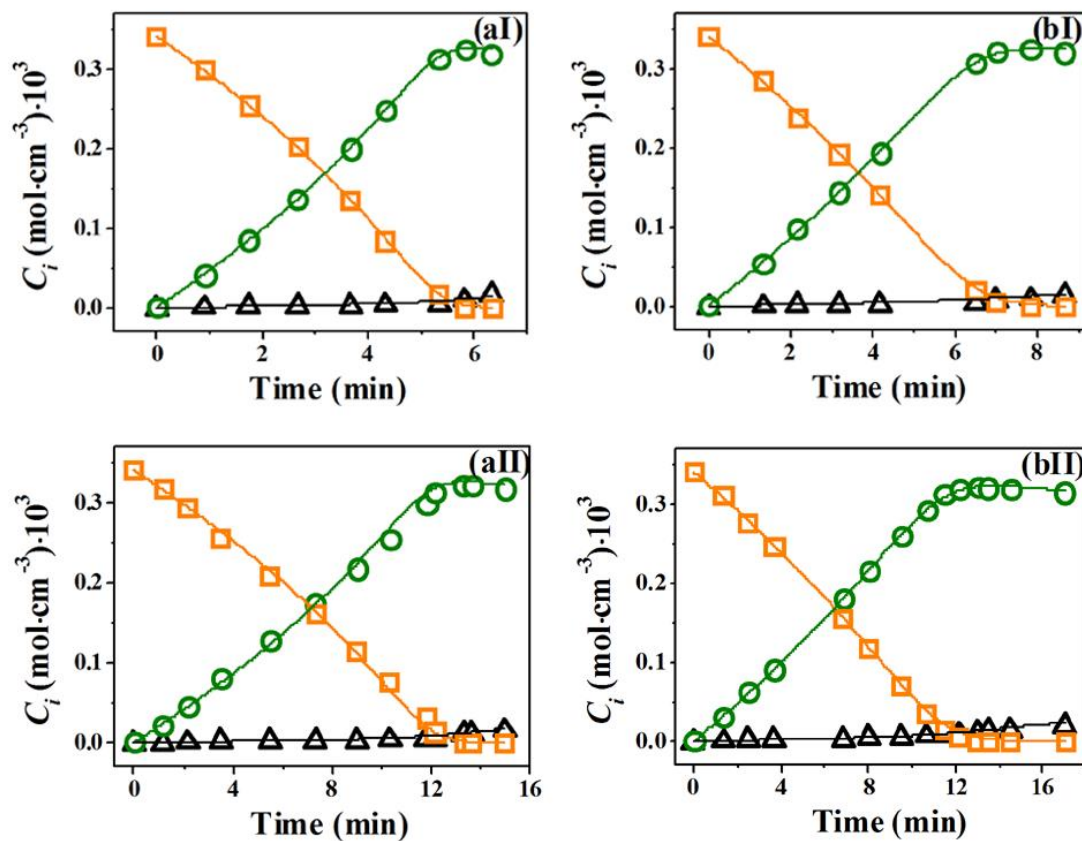


Figure 3.7. Temporal variation of MBY (\square), MBE (\circ) and MBA (\triangle) concentration (C_i) for reaction over **(a)** Pd-A and **(b)** Pd-E at **(I)** 353 K and at **(II)** 333 K where symbols represent experimental data, solid lines are estimated from application of a Langmuir-Hinshelwood model, eqns (10)-(15). *Reaction conditions:* $P_{H_2} = 4$ bar;

$$Pd_{tot}/MBY \text{ molar ratio} \sim 7 \cdot 10^{-6}.$$

As it was observed for DIP hydrogenation at 353 K, the preferential alkenol formation (**Figure 3.7 (I)** and **Figure 3.4**) was in evidence. Nonetheless, the results obtained in terms of product selectivity (**Figure 3.4** and **Table 3.2**) suggest (i) that in contrast to IP, the MBE formation is structure insensitive, *i.e.* the effect of Pd NP size on product selectivity depends on the hydrocarbon tail length and (ii) the

increased alkenol selectivity to MBE (C_1) relative to IP (C_{16}). The independence of the selectivity of Pd particle size is consistent with the reported literature [48, 61, 63] showing similar results for alkynes with the tails up to C_8 over Pd NPs in the 1 – 14 nm size range. This result suggests that while β -PdH in Pd-E and Pd-F (with $d \geq 3.6$ nm) could contribute to the unselective alkane formation [27, 60, 145] as we have pointed out for the DIP hydrogenation, the strong $C \equiv C$ adsorption must hinder this undesired overhydrogenation step. The alkyl chain in the alkynol molecule can also be adsorbed on the Pd surface *via* (weak) van der Waals forces [147]. The impact of this type of adsorption increases with the hydrocarbon chain length. As a result, the alkynol/alkenol adsorption constants ratio will decrease for alkynols with longer alkyl chain lengths, which can result in lower alkenol selectivity. This is consistent with the work of Antony *et al.* [147] who showed that activation energy of alkane desorption from Pd (111) surface increased (4.5 times) with the chain length (from C_1 = methane to C_5 = n-pentane). Parallel alignment of the molecular axes of *n*-alkanes with Pd(111) surface plane minimize CH_x group-Pd surface distance and maximize binding energy [148].

The relation between *TOF* and mean Pd NP size is presented in **Table 3.2**. Similarly to what was observed in hydrogenation of DIP at 353 K, the results obtained for MBY hydrogenation are consistent with (i) antipathetic structure sensitivity and (ii) less severe modifications in *TOF* for smaller (≤ 3.0 nm) relative to larger (≥ 3.6 nm) Pd NPs. Moreover, it is worth to stress the increased specific MBY consumption rate (relative to DIP). This can be explained in terms of steric limitations associated with

the DIP alkynol molecule with longer hydrocarbon tail as a result of adsorption on the Pd surface, *i.e.* adsorption of the long alkyl chain results in a concomitant reduction of available number of active sites, which in turn decreases the hydrogenation rate.

Catalytic response was also assessed under different reaction conditions and the effect of temperature was evaluated. As the catalytic results at 353 K have shown two tendencies for “small” (≤ 3.0 nm) and “big” (≥ 3.6 nm) particles, we selected Pd-A (2.1 nm) and Pd-E (3.6 nm) as representative samples of each group to assess the impact of reaction temperature on catalytic response. In both cases (DIP and MBY) a decrease in the temperature (from 353 K to 333 K) diminished the yield of alkene which can be ascribed to higher alkene adsorption strength at lower reaction temperatures [32, 149]. In terms of selectivity dependence on Pd NP size, the same tendency was observed at 353 K and at 333 K, *i.e.* IP selectivity decreased when particle size increased: from 95% (Pd-A) to 91% (Pd-E) and from 90% (Pd-A) to 88 % (Pd-E) at 353 K and 333 K, respectively. At the same time, the selectivity to MBE was not affected by Pd NP size at both temperatures studied. As expected, the transformation rates decreased at lower temperatures. The apparent activation energy of DIP and MBY hydrogenations over Pd-A and Pd-E was calculated using Arrhenius equation for the temperature range 313 - 353 K. The obtained values were similar (for the 4 catalysts and the 2 reactions), *i.e.* 31 ± 3 kJ mol⁻¹, and fall within the range (16 – 64 kJ mol⁻¹) [20, 21] of values quoted in the literature for acetylene alcohols.

The results presented in this section demonstrate a strong impact of Pd NP size (2.1 – 9.8 nm) on catalytic response for alkynol molecules with longer hydrocarbon

tail. Different trends were observed for NPs ≤ 3.0 and ≥ 3.6 nm, *i.e.* high activity (up to 1577 s^{-1}) over larger Pd NPs (3.6 – 9.8 nm) but increased alkene selectivity for the smaller sizes ($S_{\text{IP}} = 95\%$ for $d = 2.1 - 3.0$ nm) in the hydrogenation of DIP. Under the same reaction conditions, increased activity (up to 1874 s^{-1}) and olefin selectivity ($S_{\text{MBE}} = 98\%$) is observed in the hydrogenation of MBY (with shorter hydrocarbon tail) where the latter is insensitive to the Pd NP size for crystals in the 2.1 – 9.8 nm size-range.

3.3.4 Kinetic Model

A Langmuir-Hinshelwood model, previously used for $\text{C}\equiv\text{C}$ hydrogenations [21, 31, 32, 149, 150], was employed in order to gain a better understanding of the reaction kinetics. This model has been successfully applied to account for the observed catalytic response in MBY hydrogenation over (ZnO , TiO_2) supported Pd NPs ≥ 2.5 nm [21, 31, 78] as well as unsupported (≥ 5.5 nm) metal nanocrystals [19], but we could not find any reported work in the open literature over unsupported unimodal metal particles ≤ 3.0 nm. The development of the kinetic equations was based on a model considering a single type of active sites with bimolecular reactions between adsorbed species [19, 32, 78].

Table 3.3. Summary of the Langmuir-Hinshelwood mechanism for the hydrogenation of alkynol.

Reaction	Chemical Equation	Kinetic Expression
$Y \rightarrow E$	$Y + * \xrightleftharpoons{K_Y} Y^*$	$K_Y = \frac{\theta_Y}{C_Y \cdot \theta_*}$
	$H_2 + 2* \xrightleftharpoons{K_H} 2H^*$	$K_H = \frac{\theta_H^2}{C_H \cdot \theta_*^2}$
	$Y^* + H^* \xrightleftharpoons{K'_Y} Y'^* + *$	$K'_Y = \frac{\theta'_Y \cdot \theta_*}{\theta_Y \cdot \theta_H}$
	$Y'^* + H^* \xrightarrow{k_1} E^* + *$	$r_1 = k_1 \cdot \theta'_Y \cdot \theta_H$
	$E^* \xrightleftharpoons{K_E} E + *$	$K_E = \frac{\theta_E}{C_E \cdot \theta_*}$
$Y \rightarrow A$	$Y'^* + H^* \xrightleftharpoons{K''_Y} Y''^* + *$	$K''_Y = \frac{\theta''_Y \cdot \theta_*}{\theta'_Y \cdot \theta_H}$
	$Y''^* + H^* \xrightleftharpoons{K'''_Y} Y'''^* + *$	$K'''_Y = \frac{\theta'''_Y \cdot \theta_*}{\theta''_Y \cdot \theta_H}$
	$Y'''^* + H^* \xrightarrow{k_2} A^* + *$	$r_2 = k_2 \cdot \theta'''_Y \cdot \theta_H$
	$A^* \xrightleftharpoons{K_A} A + *$	$K_A = \frac{\theta_A}{C_A \cdot \theta_*}$
$E \rightarrow A$	$E^* + H^* \xrightleftharpoons{K'_E} E'^* + *$	$K'_E = \frac{\theta'_E \cdot \theta_*}{\theta_E \cdot \theta_H}$
	$E'^* + H^* \xrightarrow{k_3} A^* + *$	$r_3 = k_3 \cdot \theta'_E \cdot \theta_H$
	$A^* \xrightleftharpoons{K_A} A + *$	$K_A = \frac{\theta_A}{C_A \cdot \theta_*}$

The rate determining step is highlighted in bold; K_Y , K_E , K_H - adsorption constants of alkynol, alkenol and hydrogen, respectively ($\text{cm}^3 \cdot \text{mol}^{-1}$); $K_i^{n'}$ - adsorption constants of the reaction intermediates, where the superindex “ n ” is the number of hydrogen atoms attached to the molecule (-); k_i - kinetic constants of the reaction rate determining step ($\text{mol} \cdot \text{mol}_{\text{Pd}}^{-1} \cdot \text{s}^{-1}$); $\theta_i^{n'}$ - surface coverage (-).

Knowing that hydrogen dissociatively adsorbs on Pt group metals [31], the addition of a second hydrogen atom to the adsorbed organic species can be taken as the rate-determining step, whereas addition of the first atom is in quasi-equilibrium [151]. This assumption is in agreement with the observed first-order reaction towards hydrogen partial pressure established for liquid-phase $C\equiv C$ hydrogenations at $P_{H_2} = 1 - 7$ bar [32, 151]. The addition of the second hydrogen to the adsorbed alkyne has been identified as the rate limiting step as reported in various reviews [29, 30] and used to explain the experimental results obtained in the hydrogenation of alkynes [32] and alkynols [19, 21, 31].

The elementary reaction steps and associated kinetic expressions are presented in **Table 3.3** where the subscripts Y, *, E, A and H denote alkynol, active center, alkenol, alkanol and hydrogen, respectively. The mass balance of surface coverage was performed assuming a low coverage of all the intermediate species [78]:

$$1 = \theta_* + \theta_Y + \theta_E + \theta_A + \theta_H \quad (3.5)$$

Consequently, the active site coverage can be derived from equation (3.5) taking into account the surface coverage expressions for alkynol, alkenol, alkanol and hydrogen (**Table 3.3**):

$$\theta_* = \frac{1}{1 + K_Y C_Y + K_E C_E + K_A C_A + \sqrt{K_H C_H}} \quad (3.6)$$

The reaction rate expressions for the three paths (r_1 , r_2 and r_3 in **Figures 3.2** and **3.6**) of the mechanism can be developed accordingly:

$$r_1 = \frac{k_1 K_Y' K_Y K_H C_Y C_H}{\left(1 + K_Y C_Y + K_E C_E + K_A C_A + \sqrt{K_H C_H}\right)^2} \quad (3.7)$$

$$r_2 = \frac{k_2 K_Y'' K_Y'' K_Y' K_Y K_H^2 C_Y C_H^2}{\left(1 + K_Y C_Y + K_E C_E + K_A C_A + \sqrt{K_H C_H}\right)^2} \quad (3.8)$$

$$r_3 = \frac{k_3 K_E' K_E K_H C_E C_H}{\left(1 + K_Y C_Y + K_E C_E + K_A C_A + \sqrt{K_H C_H}\right)^2} \quad (3.9)$$

Equations (3.7 – 3.9) can be simplified by grouping the constants and neglecting the hydrogen [151] and alkanol [19] coverage resulting in:

$$r_1 = \frac{k_1^* K_Y C_Y}{\left(1 + K_Y C_Y + K_E C_E\right)^2} \quad (3.10)$$

$$r_2 = \frac{k_2^* K_Y C_Y}{\left(1 + K_Y C_Y + K_E C_E\right)^2} \quad (3.11)$$

$$r_3 = \frac{k_3^* K_E C_E}{\left(1 + K_Y C_Y + K_E C_E\right)^2} \quad (3.12)$$

The mass balance for alkynol, alkenol and alkanol can be then represented by the following differential equations:

$$\frac{dC_Y}{dt} = \frac{n_{Pd}}{V_R} (-r_1 - r_2) \quad (3.13)$$

$$\frac{dC_E}{dt} = \frac{n_{Pd}}{V_R} (r_1 - r_3) \quad (3.14)$$

$$\frac{dC_A}{dt} = \frac{n_{Pd}}{V_R} (r_2 + r_3) \quad (3.15)$$

Expressions (3.10 – 3.15) can be then simultaneously solved using Berkeley Madonna software [152] with Runge-Kutta method for differential equations. The results from the kinetic modeling are shown in **Figures 3.3** (DIP) and **3.7** (MBY) where the overlap between experimental (symbols) and theoretical (solid lines) values

confirm the suitability of the model. The coefficients of determination [153] calculated for all catalysts demonstrate a good correlation of predicted and experimental data ($R^2 \geq 99.5\%$). The kinetic parameters for DIP (over Pd-A, Pd-B, Pd-E and Pd-F) and MBY (for Pd-A and Pd-E, as representative samples of small (≤ 3.0 nm) and large (≥ 3.6 nm) Pd NPs, respectively) at 353 K are shown in **Table 3.4**. The k_1^*/k_2^* ratio (≥ 16) in the hydrogenation of both alkynols is indicative of a preferential stepwise (as opposed to parallel) hydrogenation route. Moreover, in terms of selectivity response, the extracted $K_Y > K_E$ (up to *ca.* 20-fold; **Table 3.4**) values for the hydrogenation of both, DIP and MBY, over all the NPs sizes investigated in this work are within the range of values (10 – 1000) reported in the literature [19, 21, 31, 78] and can account for the inhibited full hydrogenation (to alkanol) as a result of strong $C\equiv C$ adsorption [22]. The higher alkenol selectivity in the hydrogenation of MBY as compared to DIP (up to 97% and 95%, respectively) is consistent with the greater (by up to a 3-fold) K_{MBY}/K_{MBE} ratio (relative to K_{DIP}/K_{IP}), *i.e.* higher alkynol/alkenol adsorption strength for alkyne with shorter hydrocarbon tail.

Moreover, the results in **Table 3.4** demonstrate negligible difference (5%) in the K_Y/K_E ratio in the MBY hydrogenation between small and large Pd particles, which is consistent with the structure insensitive MBE selectivity response. It follows that a more significant (25%) decrease of K_Y/K_E ratio for larger particles in the DIP hydrogenation can account for the lower IP selectivity over Pd NPs ≥ 3.6 nm (see **Table 3.2**).

Table 3.4. Kinetic (k_i^*) and adsorption (K_i) parameters extracted from kinetic modeling (see eqns. 3.7 – 3.12) of DIP and MBY hydrogenation over Pd-A, Pd-B, Pd-E and Pd-F.

Alkynol reactant	T (K)	Sample	Kinetic Constants mol mol _{Pd} ⁻¹ s ⁻¹			Adsorption Constants (cm ³ mol ⁻¹) × 10 ⁻¹		K_Y/K_E
			k_1^*	k_2^*	k_3^*	K_Y	K_E	
DIP	353	Pd-A	1850±10	81±3	130±5	1330±13	160±1	8
		Pd-B	1575±11	78±3	126±4	1050±10	130±2	8
		Pd-E	1400±11	75±1	121±1	570±2	100±1	6
		Pd-F	694±4	43±1	66±1	570±1	100±1	6
	333	Pd-A	1295±10	61±1	96±2	2000±28	570±4	4
		Pd-E	775±7	46±1	75±1	910±13	370±3	3
MBY	353	Pd-A	2728±4	72±3	142±10	1790±42	90±1	20
		Pd-E	1929±16	54±1	138±3	1110±11	60±1	19
	333	Pd-A	1798±3	48±2	99±4	3124±44	293±1	11
		Pd-E	1135±3	32±2	87±2	1395±13	140±1	10

The results presented in the previous section were consistent with an increase in activity with the fraction of Pd_{plane} , which suggests that they are the active sites for alkynol hydrogenation. Nonetheless, modifications in catalytic activity with Pd dispersion could also arise from modifications in the energies of adsorption [59]. The results presented in **Table 3.4** are consistent with an inverse increase in Pd NP size and decrease in K_Y which should result in higher activity due to lower adsorption

strength [60], *i.e.* antipathetic structure sensitivity. Pd-E and Pd-F with the bigger Pd NPs sizes deviate somehow from this trend with similar K_Y values. We account for this difference in terms of negligible modifications in the electronic properties of large metal nanoparticles (≥ 3.6 nm). Likewise, Semagina *et al.* [48] and Crespo *et al.* [19] suggested no or negligible change in electronic properties and, accordingly, in adsorption constants for particles above 6 nm. We can conclude that the activity response in the DIP hydrogenation at 353 K is affected by both, changes in electronic properties of the metal NPs, which are significant in colloids ≤ 3.0 nm, and fraction of Pd_{plane} . Nonetheless, the results in **Tables 3.2** and **3.4** show an increase in activity (*TOF*) for the MBY hydrogenation (compared to that of DIP) in spite of the higher K_Y , which must arise from the steric contributions leading to the lower hydrogenation rate for DIP (with bigger hydrocarbon tail).

In order to evaluate the temperature dependence on Pd NPs crystal size, the kinetic parameters over Pd-A and Pd-E samples as representatives of “small” (≤ 3.0 nm) and “big” (≥ 3.6 nm) NPs respectively, were estimated for both DIP and MBY hydrogenation at 333 K (**Table 3.4**). High k_1^*/k_2^* (≥ 17) and k_1^*/k_3^* (≥ 10) ratios as well as higher K_Y compared to K_E (up to *ca.* 10-fold) can account for the favorable alkenol formation. The increase in both alkynol and alkenol adsorption strength and corresponding decrease of K_Y/K_E ratios at 333 K, relative to 353 K, is in line with the decrease in alkenol selectivity at lower reaction temperature (see **Table 3.4**). Moreover, our results are in agreement with the kinetic Monte-Carlo simulations performed by Mei *et al.* [25, 154] who explained the selectivity *vs.* temperature modifications from the basis of variations in the $C\equiv C/C=C$ specific surface coverage.

The IP selectivity (**Table 3.2**) decreases from 95% to 90% ($\text{Pd} \leq 3.0\text{nm}$) and from 91% to 88% ($\text{Pd} \geq 3.6\text{ nm}$) upon the temperature decrease from 353 K to 333 K which can be accounted for in terms of increased alkenol desorption at higher temperatures with an overall lower olefin surface coverage. As it happens at 353 K, the more severe modifications in the K_Y/K_E ratio for particles ≤ 3.0 and $\geq 3.6\text{ nm}$ in DIP (25%) relative to MBY (9%) can explain the structure insensitive MBE selectivity response.

The combined kinetic modeling and experimental results demonstrate that activity and alkenol selectivity response can be tuned by modifications in Pd NPs size with a critical size between 3.0 – 3.6 nm and where catalytic performance is strongly affected by electronic ($\text{C}\equiv\text{C}$ adsorption strength), structural (fraction of Pd_{plane}) and steric (alkyl chain size in the alkynol reactant) effects.

3.4 Conclusions

The results obtained during this work support the following conclusions:

- (i) Colloidal techniques using PVP as stabilizer allowed synthesizing a series of monodispersed Pd NPs in the range of 2.1 – 9.8 nm as demonstrated by HRTEM analysis.
- (ii) The liquid phase hydrogenation of DIP (with C_{16} alkyl tail) is characterized by *antipathetic structure sensitivity* with higher *TOF* over bigger Pd NPs. The formation of the target product of *semi*-hydrogenation (IP) was affected by Pd NPs size with increased selectivities ($S_{\text{IP}}; X_{\text{DIP}} = 98\% \sim 95\%$) for smaller particles (2.1 - 3.0 nm).

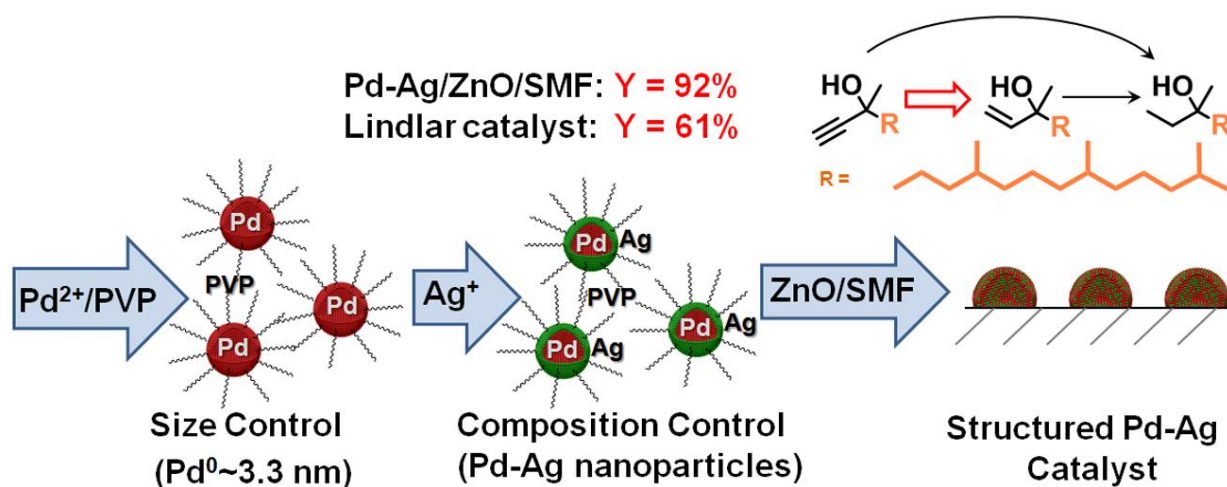
(iii) Under the same reaction conditions, higher activity and a similar *antipathetic structure sensitivity* is observed for MBY (with C₁ alkyl tail) hydrogenation with higher *TOF* over bigger Pd NPs. The selectivity to MBE was higher as compared to IP and insensitive to particle size (2.1 → 9.8 nm, S_{MBE} ; $X_{\text{MBY}} = 98\% \sim 98\%$).

(iv) A Langmuir-Hinshelwood kinetic model was consistent with the experimental results allowing to explain the differences in activity/selectivity on the basis of modifications in (i) electronic (variations in energies of adsorption), (ii) structural (increased fraction of Pd_{plane} in larger Pd NPs) and (iii) steric (short alkyl chain size in MBY versus long in DIP) effects.

In summary, we have for the first time demonstrated that during the Pd-catalyzed alkynol hydrogenation the selectivity to alkenol is favored over small Pd NPs (2.1 – 3.0 nm) but this effect depends on the alkynol structure (the length of alkyl chain). The results obtained demonstrate the viability of the *nanoscale* approach for the catalyst design and optimization towards the highest yield of the target product meeting the industrial demands.

Chapter 4

Selective Hydrogenation of Alkynols: Pd Modification with Second Metal



This chapter is based on the following publication: A. Yarulin, F. Cárdenas-Lizana, D.T.L. Alexander, L. Kiwi-Minsker, *Appl. Catal. A* 478 (2014), 186-193. Reproduced with permission of Elsevier (Copyright 2014).

Abstract

In this chapter, the further development of selective Pd-based catalyst for *semi*-hydrogenation of DIP is reported. A series of *unsupported* mono- (Pd) and bimetallic (Pd-M) nanoparticles (NPs) with Pd/M molar ratios of 1.5 – 5.0 (M = Ag or Cu) were examined as model systems. The Pd-Ag and Pd-Cu NPs with controlled crystal sizes of *ca.* 3.4 nm were prepared by Ag (Cu) electroless deposition on pre-formed PVP-stabilized Pd⁰ colloids. Bimetallic Pd-Ag NPs adopted a core (Pd)-shell (Ag) structure whereas a mixed alloy was attained in the Pd-Cu nanocrystals. A (partial) Pd surface segregation induced by reaction with H₂ was in evidence for the Pd-Ag NPs. A significant increase in selectivity up to 97% (at $X_{\text{DIP}} = 99\%$) to the target alkenol was demonstrated following the incorporation of a second metal. This result is attributed to the dilution of the surface Pd-sites by Ag (Cu) and a modification of the Pd electronic properties. Pd-Ag NPs, having shown the highest selectivity, were further deposited on a structured support based on SMF coated with ZnO. The improved selectivity achieved over the unsupported Pd-Ag colloidal NPs was retained over the structured catalytic system. The bimetallic Pd_{5.0}Ag/ZnO/SMF ($S_{\text{IP}} = 93\%$) demonstrated a drastic increase in IP selectivity relative to the monometallic Pd/ZnO/SMF ($S_{\text{IP}} = 78\%$) and state-of-the-art *Lindlar* catalyst ($S_{\text{IP}} = 62\%$) at DIP conversion $\approx 99\%$ with the stable activity during 50 h, suggesting catalyst feasibility for selective *semi*-hydrogenation of long chain alkynols with important applications in the manufacture of vitamins and fine chemicals.

4.1 Introduction

The selective *semi*-hydrogenation of long-chain ($\geq C_{20}$) alkynols (to the correspondent alkenol) is an important reaction in fine chemistry with a prominent example in DIP \rightarrow IP transformation. The latter is an intermediate in the industrial synthesis of vitamin E [131, 132] with an estimated annual worldwide production of $>30 \cdot 10^3$ tonnes [8]. Typically, IP selectivity over conventional Pd catalysts reaches *ca.* 80% at high DIP conversions [14].

Bimetallic NPs can be regarded as a more sustainable catalytic alternative relative to the lead-containing Lindlar catalyst commonly employed for alkynol hydrogenations at industrial level [8, 14, 16, 17]. Increased olefin selectivities (up to 99%) have been reported in the hydrogenation of short chain ($\leq C_{14}$) alkynols over Ag^0 [71], Cu^0 [72, 73], and Zn^0 -modified [17] Pd catalysts, although there is a dearth in the literature focused on the application of bimetallic systems for the *semi*-hydrogenation of alkynols with longer hydrocarbon chain.

The physical and chemical properties of bimetallic NPs strongly depend on the distribution of both metals within the crystal nanostructure [68, 74, 75] which, in turn, impacts on hydrogenation catalytic response [76]. The structure of bimetallic NPs is affected by a number of parameters, such as preparation technique (e.g. sequential and simultaneous reduction methods lead to the formation of $Ag_{core}Pd_{shell}$ and Ag-Pd alloy NPs, respectively [76]), the difference in atomic radii [155], surface energies [156] and/or relative amount of both metals [157, 158], NP size [159], type of

support [18, 160], and/or reaction environment (e.g. modified surface composition of Pt-Co, Rh-Pd and Pt-Pd bimetallic NPs in the presence of CO, NO, O₂, H₂ due to surface catalyst restructuring [77, 161]).

In terms of rational catalyst design, colloidal NPs represent a valuable model systems to understand the nature of the catalytic systems and optimize bimetallic catalysts [51, 129] although there is a requirement of their subsequent deposition onto a support for industrial implementation. In this respect, a ZnO-based support is a promising candidate due to its ability to form an intermetallic Pd-Zn phase upon interaction with Pd NPs under hydrogen which prevents metal leaching into the reacting mixture improving catalyst stability [31].

This chapter shows the results on the development of a stable and highly selective catalytic system for DIP (as a model molecule bearing a long-chain) *semi*-hydrogenation. We adopted the methodology of using colloidal (Pd, Pd-Ag and Pd-Cu) NPs with controlled size and composition for direct correlation with catalytic performance. Catalytic response was rationalized by characterizing catalysts using scanning transmission electron microscopy (STEM) coupled with energy-dispersive X-ray spectroscopy (EDX).

4.2 Experimental

4.2.1 Materials

Poly(N-vinyl-2-pyrrolidone) (PVP, Sigma Aldrich; $M_w \sim 50000$), palladium (II) chloride anhydrous (Sigma Aldrich; $\geq 95.0\%$), sodium chloride (Fluka; $\geq 99.5\%$),

ethanol (Sigma Aldrich; 99.8%), L-ascorbic acid (Sigma Aldrich; 99.0%), zinc acetate dihydrate (Fluka; $\geq 99.5\%$), monoethanolamine (Fluka; $\geq 99.0\%$), 3-hydroxybutynone (acetoin, mixture of monomer and dimer; Fluka; $\geq 97.0\%$), hydrazine hydrate (Fluka; 24 – 26% in water), potassium dicyanoargentate (I) (Sigma Aldrich; 99.9%), copper (II) formate (Sigma Aldrich; 97.0%), DIP (DSM Nutritional Products; $\geq 95\%$) were used as received without further purification. H_2 and N_2 were of ultra-high purity (Carbagas; $\geq 99.99\%$). FeCrAl-alloy sintered metal fibers (SMF; Cr 20%, Al 5%, Y > 1%, other elements ca. 1–2%, Fe balance) were purchased from Bekaert SA (Belgium).

4.2.2 Preparation of Mono- and Bimetallic Nanoparticles

A series of PVP-stabilized NPs were prepared by colloidal technique [100]. Pd NPs were synthesized by heating (363 K) an aqueous solution (30 cm³) containing PVP ($5.0 \cdot 10^{-3}$ mol) and ascorbic acid ($8.5 \cdot 10^{-4}$ mol) as stabilizing and reducing agents, respectively. An aqueous Na_2PdCl_4 solution ($1.0 \cdot 10^{-4}$ mol cm⁻³; PVP/Pd molar ratio = 10), prepared by dissolving $PdCl_2$ and NaCl in water (Pd/Na molar ratio = 0.5), was added to the PVP-containing solution and the mixture was stirred for 3 h at 363 K. The instantaneous dark coloration of the solution after the Pd precursor was added indicated the formation of Pd^0 NPs [92]. The NPs stabilized by PVP were separated from the solution via flocculation with acetone (1/3 v/v solution/acetone), rinsed thoroughly with acetone (3 times), centrifuged and redispersed in water attaining ca. 0.4% wt. Pd in the final solution.

Ag NPs as reference nanocatalysts were prepared by colloidal methodology following the procedure described in detail elsewhere [76]. Briefly, $AgNO_3$ ($2.3 \cdot 10^{-4}$

mol) and PVP ($2.3 \cdot 10^{-3}$ mol) were dissolved in 30 cm³ of ethylene glycol under stirring. The solution was slowly heated in a 100 cm³ min⁻¹ N₂ flow at 7 K min⁻¹ up to 393 K for 30 min to obtain a colloidal solution of Ag NPs, which were subjected to the post-treatment procedure as described above.

A catalytic electroless deposition method [115] was used for the preparation of a series of bimetallic Pd-Ag and Pd-Cu NPs (denoted in this work as Pd_xM with x defined as the Pd/M molar ratio = 5.0, 3.5, 2.0 and 1.5) where Pd acts as a catalyst for the Ag and Cu reductive deposition. A calculated amount of the second metal precursor (potassium dicyanoargentate (I) or copper (II) formate) was added to the prepared PVP-stabilized Pd⁰ colloidal solution. In the case of Pd-Ag system, *ca.* 0.3 cm³ of hydrazine hydrate (*ca.* 25% in water) as a reducing agent was added to the solution whereas the Cu precursor already contains intrinsic reducing agent – formate. The mixture was subsequently stirred for 3 hours at room temperature to promote the formation of bimetallic NPs.

4.2.3 Preparation of Supported Catalysts

SMF panels were treated in boiling toluene for 0.5 h (to remove grease [162]), dried (at room temperature in air) and oxidized (in air) at 973 K for 3 h in order to improve adhesion of ZnO [31]. Finally they were cooled down to the room temperature.

A homogeneous ZnO film was prepared by sol-gel method [31]. Monoethanolamine (18.3 g) and acetoin (12.8 g) – solubility enhancement additives that prevent ZnO crystallization in solution before deposition [31] – were dissolved in iso-propanol ($1 \cdot 10^3$ cm³) and 65.8 g of zinc acetate dihydrate were added to the solution under

continuous stirring. The SMF panels underwent a three-step procedure based on (i) dipping (into the ZnO precursor solution), (ii) drying in air at room temperature (0.5 h) and (iii) calcination in air at 873 K for 0.5 h. This multistep procedure was repeated 6 times to deposit ca. 5% wt. ZnO. The coated SMFs were post-annealed in air at 1173 K for 15 min to promote ZnO crystallization [31].

The metal NPs prepared by colloidal method were deposited by impregnation of the pre-synthesized colloidal dispersion on the 5%ZnO/SMF support followed by air-drying. The procedure was repeated twice to attain 0.2% wt. of Pd on the support. In order to ensure the anchoring of the metal NPs on the support, the PVP was removed from the particle surface by air calcination at 873 K [163] and the catalyst was then activated in H₂ flow (10% in Ar, total flow 450 cm³ min⁻¹) at 573 K (heating 10 K min⁻¹) for 2 h.

4.2.4 Catalyst Characterization

The metal (Pd, Cu and Ag) content in the synthesized colloidal solutions and powdered Lindlar catalyst was measured by atomic absorption spectroscopy (AAS) using a Shimadzu AA-6650 spectrometer with an air-acetylene flame from the diluted solutions in aqua regia (2/3 v/v HNO₃/HCl).

Metal NP size was determined by transmission electron microscopy (TEM) with a Philips CM20 instrument operated at an accelerating voltage of 200 kV and using Gatan Digital Micrograph 3.4 for data treatment. The specimens were prepared by NPs dispersion in ethanol and their deposition on a holey carbon/Cu grid (300 Mesh).

Up to 500 individual NPs were counted for each sample and the mean particle diameter (d) was calculated from:

$$d \text{ (nm)} = \frac{\sum_i n_i d_i}{\sum_i n_i} \quad (4.1)$$

Annular dark-field (ADF) imaging and EDX mapping were performed in STEM mode using a sub-nm probe with a FEI Tecnai Osiris microscope operated at 200 kV, equipped with high brightness XFEG gun and Super-X EDX technology (4 SDD detectors and 0.9 sr solid angle). EDX map data were calculated by integrating the areas of deconvoluted Pd L α , Ag L α and Cu K α peaks, and were processed with a smoothing function to reduce noise.

4.2.5 Catalytic Hydrogenation

Liquid-phase hydrogenation reactions ($P_{H_2} = 4$ bar; $T = 353$ K) were carried out in a *semi*-batch stirred stainless steel reactor (150 cm³ autoclave; Buchi AG, Uster, Switzerland) equipped with a heating jacket and a hydrogen supply system. Hydrogen consumption was monitored *on-line* with a press gas flow controller (BPC-6002, Büchi, Switzerland). A stainless steel 6-blade disk turbine impeller (equipped with a self-gassing hollow shaft) provided effective agitation. A recirculator (HAAKE B-N3) was used to stabilize the reaction temperature within ± 1 K using water as the heating medium. Reactions over unsupported NPs were carried out with ethanol as a solvent. At the beginning of each experiment the reactor was charged with DIP/ethanol solution (80 cm³) and a colloidal solution of NPs ($C_{DIP} = 3.4 \cdot 10^{-4}$ mol cm⁻³, Pd/DIP

(Ag/DIP for monometallic Ag NPs) molar ratio $\sim 10^{-5}$). The supported ZnO/SMF-based catalysts were placed between two grids fixed on a self-gassing hollow shaft stirrer (the powdered Lindlar catalyst was added directly to DIP) and tested in a solvent-free system ($C_{\text{DIP}} = 2.7 \cdot 10^{-3} \text{ mol cm}^{-3}$, $\text{Pd/DIP} \sim 10^{-5}$). Before the experiment, the reactor was flushed three times with N_2 under constant agitation in order to remove O_2 . The temperature was set and allowed to stabilize (*ca.* 30 min). Hydrogen was then introduced and the system was pressurized (time $t = 0$ for reaction). In a series of blank tests, reactions carried out in the absence of catalyst or over the support (ZnO/SMF) alone did not result in any measurable conversion. The absence of external diffusion limitations was determined experimentally by measuring the catalytic activity as a function of reaction mixture stirring speed. It was found that at stirrer rotations above 1500 rpm the reaction rate was independent of mixture agitation intensity ensuring sufficient turbulence. The absence of internal mass transfer limitations under similar reaction conditions was previously shown [78] and is attributed to the SMF open structure and thin ZnO layer (*ca.* 1.5 μm) resulting in a small depth of the pores [31]. A non-invasive liquid sampling system allowed a controlled removal of aliquots ($\leq 0.5 \text{ cm}^3$) from the reactor.

The composition of the reaction mixture was analyzed using a Perkin-Elmer Auto System XL gas chromatograph equipped with a programmed split/splitless injector and a flame ionization detector employing a Stabilwax (Cross-bond Carbowax-PEG, Restek, USA) capillary column (i.d. = 0.32 mm, length = 30 m, film thickness = 0.25 μm). Data acquisition/manipulations were performed using the TotalChrom Workstation Vers. 6.3.2. (for Windows) chromatography data system and the

concentration of organic species in the bulk liquid phase were determined from the total mass balance in the reaction mixture. The conversion of DIP is defined as

$$X_{\text{DIP}} (\%) = \frac{C_{\text{DIP},0} - C_{\text{DIP}}}{C_{\text{DIP},0}} \cdot 100 \quad (4.2)$$

and selectivity with respect to IP, as the target product, is given as

$$S_{\text{IP}} (\%) = \frac{C_{\text{IP}}}{C_{\text{DIP},0} - C_{\text{DIP}}} \cdot 100 \quad (4.3)$$

4.3 Results and Discussion

4.3.1 Characterization of Mono- and Bimetallic Nanocatalysts

Mono- and bimetallic NPs were synthesized by colloidal technique using PVP as a stabilizing agent. The stabilization of the metal nanocrystals is achieved *via* interaction between the carbonyl groups in the PVP molecules and the metal surface atoms [91, 133] *i.e.* NPs agglomeration is avoided. The results presented in **Figure 4.1 (IA)** are consistent with the formation of small Pd NPs (mean size = 3.3 nm) with a narrow size distribution (**Figure 4.1 (IB)**). This is in agreement with reported literature [100] showing that the combined use of PVP (as stabilizer) and L-ascorbic acid (as reducing agent) results in the formation of small (≤ 8 nm) Pd NPs. The spherical shape is indicative of a cubo-octahedral particle morphology, the most thermodynamically favorable crystal geometry [100].

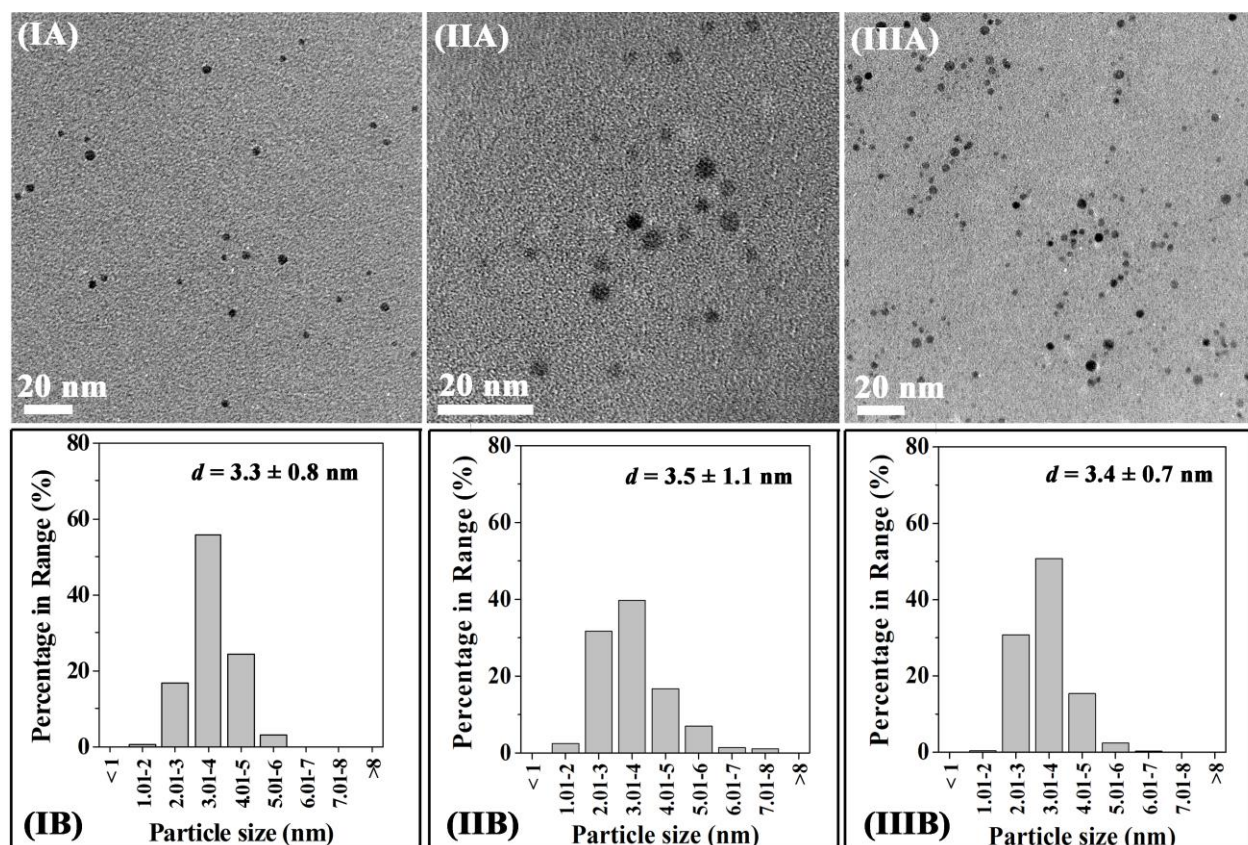


Figure 4.1. Representative **(A)** TEM images and associated **(B)** metal particle size distributions of PVP-stabilized mono- **(I)** Pd and bimetallic **(II)** Pd_{1.5}Ag and **(III)** Pd_{1.5}Cu nanoparticles.

Bimetallic nanocatalysts were prepared by electroless deposition [108] of Ag or Cu from a precursor on pre-formed Pd NPs. This preparation technique can be regarded as selective deposition of a second metal by a controlled catalytic (Pd) surface reaction [164]. The concomitant high complex formation constant ($\log_{10}\beta = 21.1$) and associated negative standard reduction potential ($E_0 = -0.31$ V) of the $[\text{Ag}(\text{CN})_2]^-$ anion impart high stability to the Ag precursor [164] which, together with the preferential Pd-activation of hydrazine (reducing agent) [165], ensures the selective reduction of the

silver precursor on the Pd surface. Copper (II) formate is also catalytically decomposed generating metallic Cu on the Pd surface [166].

Representative TEM images **(A)** and associated metal size distributions **(B)** of bimetallic Pd_{1.5}Ag **(II)** and Pd_{1.5}Cu **(III)** NPs with the highest content of Ag and Cu are presented in **Figure 4.1**. The bimetallic nanocrystals show a homogeneous distribution with quasi-spherical morphology that is close to that of the starting Pd colloids, *i.e.* there is only a small degree of redispersion and/or agglomeration upon incorporation of the second metal. A similar NP size (variations ± 0.6 nm) was also observed for Pd, Ni and Pd_xNi alloyed NPs ($x = 0.1 - 9.0$) [167]. The similar NP size of the mono- and bi-metallic samples can be attributed to the low amount of the second metal. Indeed, an increase in size of *ca.* 2 atomic layers can be expected for Pd NPs of 3.3 nm after the incorporation of a second metal (M) with a Pd/M molar ratio of 1.5 (the highest ratio in this work) according to surface statistics applying the non-ideal fcc cubo-octahedral crystal model proposed by van Hardeveld and Hartog [53]. This is in agreement with the results shown by Tedsree *et al.* [76] where the deposition of Pd on Ag NPs (Ag/Pd ratio = 1) resulted in a shell thickness increase of 1-2 atomic layers.

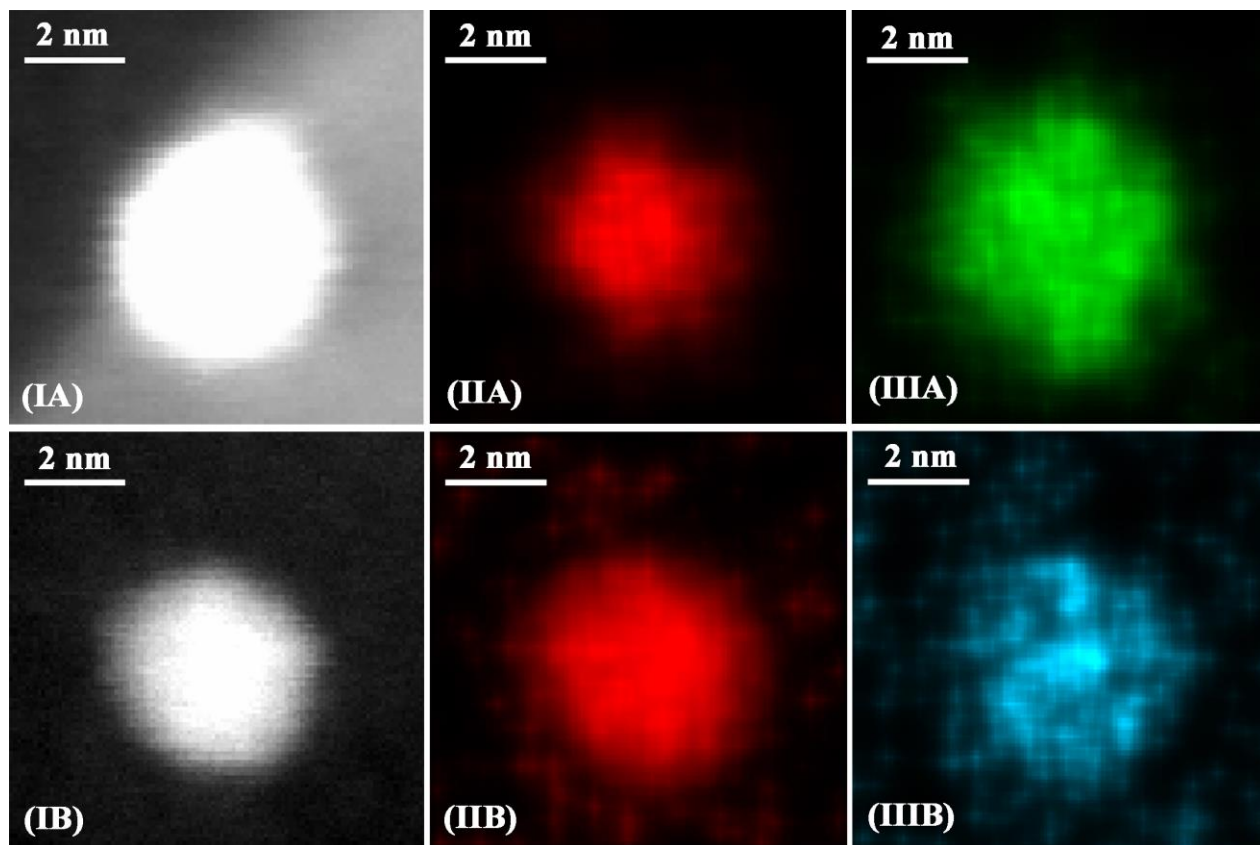


Figure 4.2. Representative STEM-EDX analyses of **(A)** Pd_{1.5}Ag and **(B)** Pd_{1.5}Cu NPs; **(I)** ADF image with EDX elemental maps illustrating the distribution of **(II)** Pd, **(IIIA)** Ag and **(IIIB)** Cu in the metal nanocrystals.

The structure of the bimetallic NPs (Pd_{1.5}Ag and Pd_{1.5}Cu) was further assessed by means of STEM-EDX elemental mapping. A representative measurement for Pd_{1.5}Ag **(A)** and Pd_{1.5}Cu **(B)** is shown in **Figure 4.2**, which includes the ADF image of the sample area **(I)** that was mapped with the associated distribution of Pd **(II)** and second metal (Ag or Cu) **(III)**. EDX mapping of Pd_{1.5}Ag suggests an Ag surface enrichment with Pd in the core of the bimetallic crystal structure, *i.e.* an outer Ag layer of *ca.* 0.6 nm equivalent to *ca.* 2 atomic layers (atomic radius of silver $r_{\text{Ag}} = 0.144$

nm [67]) consistent with the surface statistics. This result is also in line with the preparation method [168] and the lower Ag surface energy ($\gamma_{\text{Ag}} = 1.25 \text{ J m}^{-2}$) relative to Pd ($\gamma_{\text{Pd}} = 2.10 \text{ J m}^{-2}$) [169]. Moreover, the slightly larger Ag atoms (atomic radius of palladium $r_{\text{Pd}} = 0.137 \text{ nm}$ [67]) induce less strain at the surface than in the subsurface that renders stability to the bimetallic structure [170]. The similar structure with a Ag-rich shell can be expected for the rest of Pd-Ag systems with modified Ag content where, giving that for Pd/Ag ratios > 3 the amount of Ag is too low to fully cover the Pd NP and on the basis of the van Hardeveld and Hartog NP model [53], we can propose an open-shell NP structure. In the case of Pd-Cu NPs, EDX mapping points to alloy formation with both metals randomly distributed in the metal crystal structure, *i.e.* similar distribution areas for Pd **(IIB)** and Cu **(IIIB)** in **Figure 4.2**, a result that extends to the rest of the Pd-Cu NPs with different Pd/Cu molar ratios. The Pd-Cu bimetallic structure is determined, on one hand, by the smaller Cu atomic size ($r_{\text{Cu}} = 0.128 \text{ nm}$ [67]) compared to Pd that results in Pd segregation to the NP surface [155, 169], on the other hand, by a slightly lower Cu surface energy ($\gamma_{\text{Cu}} - \gamma_{\text{Pd}} = -0.25 \text{ J m}^{-2}$ [169]) which suggests partial Cu surface segregation. It has been shown elsewhere [171] that partial segregation of Cu leads to a mixed alloy structure in bimetallic NPs with 12-28% mol. Pd on the surface, an effect that is prevalent even at high Cu/Pd ratios (up to 2.0). Bradley *et al.* [96] have shown that the reaction between Pd NPs and Cu precursor resulted in the reduction of Cu^{II} (to Cu^0) on the Pd surface followed by diffusion of Cu atoms into the NP subsurface region to maximize Pd-Cu bond formation by gaining the highest possible coordination number for Cu atoms with Pd. These results were also supported by theoretical calculations reporting the

lowest energy atomic configuration for a mixed alloy structure with Pd-rich surface [158].

The results in this section are consistent with the formation of highly dispersed homogeneous *mono*- (Pd) and *bimetallic* (Pd-Ag and Pd-Cu) NPs with similar NP size (*ca.* 3.4 nm). EDX mapping has revealed core-shell and alloy structures in the bimetallic Pd-Ag and Pd-Cu nanocatalysts, respectively, regardless of the relative amounts of both metals.

4.3.2 Catalytic Results over Unsupported Nanoparticles

The synthesized mono- and bimetallic Pd-containing colloidal nanocatalysts were tested in the liquid-phase DIP hydrogenation. The product distribution was monitored as the conversion increased with time, and representative behavior over Pd (**I-II**), Pd-Ag (**I**) and Pd-Cu (**II**) nanocatalysts is shown in **Figure 4.3**. The preferential formation of the target alkenol (*i.e.* $90\% \leq S_{IP} \leq 94\%$) over monometallic Pd NPs is in evidence for DIP conversions up to 99%. The remarkable performance of Pd in $C\equiv C$ bond hydrogenation reactions is well-known [10, 59] where high selectivity to the $C=C$ product has been attributed to a higher triple bond (relative to double bond) adsorption strength [60]; stronger ($C\equiv C$ bond containing) DIP adsorption on Pd surface diminishes the adsorption of IP (a *semi*-hydrogenation $C=C$ product) on the active sites and hence diminishes further ($C=C \rightarrow C-C$) hydrogenation and formation of HIP [172].

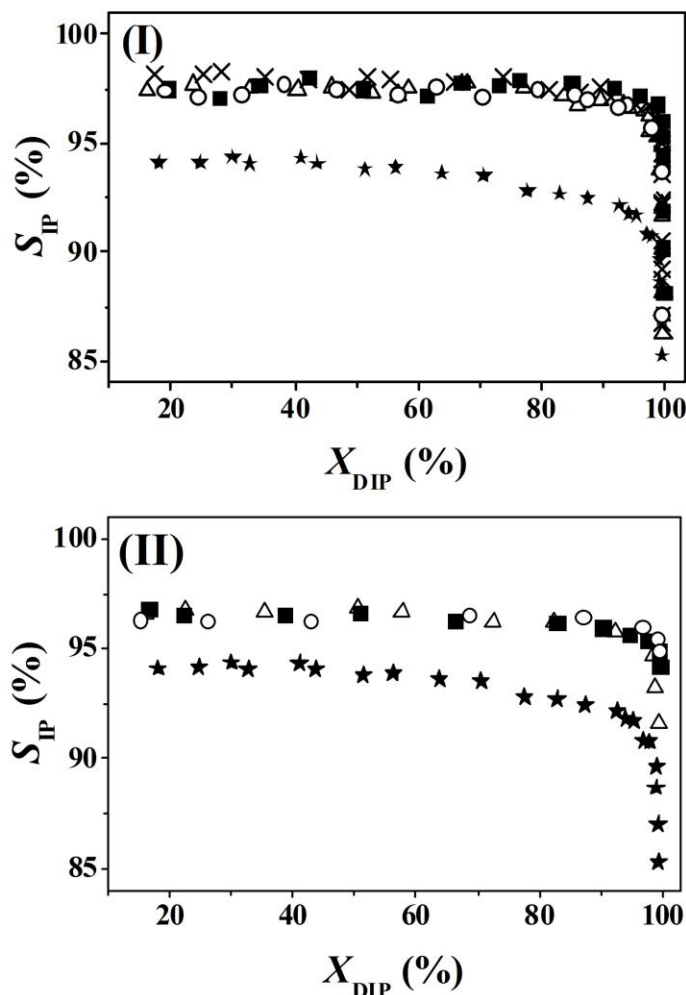


Figure 4.3. Selectivity to IP (S_{IP}) as a function of DIP conversion (X_{DIP}) for reaction over PVP-stabilized Pd-M NPs: **(I)** M = Ag, **(II)** M = Cu with Pd/M molar ratios

equal to (★) ∞ , (△) 5.0, (■) 3.5, (×) 2.0 and (○) 1.5. *Reaction conditions:*

$P_{H_2} = 4$ bar; $T = 353$ K; $C_{DIP} = 3.4 \cdot 10^{-4}$ mol cm $^{-3}$; Pd/DIP molar ratio $\sim 10^{-5}$.

The results in **Figure 4.3** show a significant increase in IP selectivity for Pd NPs modified with Ag ($97\% \leq S_{IP} \leq 98\%$) and Cu ($95\% \leq S_{IP} \leq 97\%$) at DIP conversions up to 99%. The improved selectivity over the bimetallic Pd-M systems (M = Ag or Cu) can be attributed to a modification of electronic properties of surface Pd owing to its

interaction with neighboring Ag (Cu) atoms. This change in electronic properties, in particular the shift in *d*-band center, can affect the adsorption strength of substrate and product resulting in an overall decrease in the ratio of DIP/IP adsorption energies suppressing the IP over-hydrogenation. Moreover, a charge transfer from Ag to Pd in bimetallic NPs has been shown elsewhere both theoretically [173] and experimentally [174] whereas the electronic influence of Cu on Pd is still a matter of debate [60]. Nonetheless, a selectivity change can be also a result of a modified surface composition since mixing two metals affects the number of Pd active sites and the DIP adsorption mode due to surface dilution with Ag (Cu) that is crucial for IP selectivity [20, 60]. Indeed, the STEM/EDX elemental mapping analyses show the presence of Ag and Cu on the surface of the bimetallic NPs diminishing the surface concentration of Pd active sites (geometric effect). The favored Pd-Ag (as compared to Pd-Cu) nanocatalyst performance in terms of higher IP selectivity can be attributed to the stronger electronic [169] effect of Ag on Pd.

The results presented in **Figure 4.3** show that, at values close to full conversion, the IP selectivity decreases drastically for all the catalysts while the formation of HIP is promoted. This can be attributed to the low DIP coverage at $X_{\text{DIP}} > 99\%$ allowing IP readsorption with further over-hydrogenation towards HIP. A similar rationale was provided by Bennett *et al.* [175] to account for the decrease in butenediol selectivity at high conversions in the hydrogenation of butynediol.

It is worth flagging that the results show that alkenol selectivity is not affected by the amount of the modifier in both Pd-Ag and Pd-Cu systems. Moreover, the bimetallic nanocatalysts are equally selective even for concentrations of the second metal at

which Pd should be fully covered by Ag (*e.g.* Pd_{1.5}Ag). This result is striking giving that, although Ag was shown to be able to catalyze gas-phase alkyne hydrogenation [176], it has low capacity for H₂ uptake/activation [64, 177] and so, the catalytic activity for Pd-Ag with high Ag content on the surface suggests catalyst restructuring with Pd segregation to the NP surface. In order to confirm this possibility additional experiments over monometallic Ag NPs were conducted under similar reaction conditions. The lack of activity recorded further confirms that Pd is the active phase for the reaction where Ag promotes electronic/geometric changes that impact on catalytic response. Moreover, given that after electroless deposition Ag is located on the NP surface, Pd must migrate to the surface and become available for the adsorption/activation of the reactants.

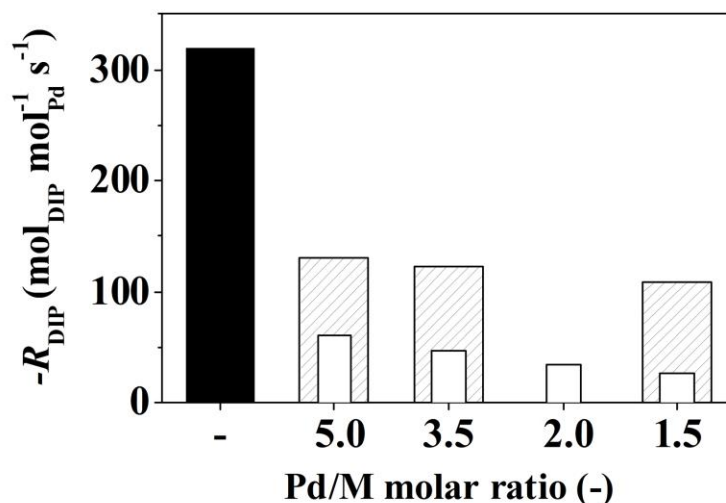


Figure 4.4. Initial DIP transformation rate ($-R_{\text{DIP}}$) as a function of Pd/M molar ratio (M = Ag or Cu), for reaction over monometallic Pd (solid bar), Pd-Ag (open bars) and Pd-Cu (hatched bars). *Reaction conditions:* $P_{\text{H}_2} = 4$ bar; $T = 353$ K;

$$C_{\text{DIP}} = 3.4 \cdot 10^{-4} \text{ mol cm}^{-3}; \text{Pd/DIP molar ratio } \sim 10^{-5}.$$

In terms of activity, the initial DIP transformation rate ($-R_{\text{DIP}}$) was determined from a linear regression of the temporal DIP concentration profiles at low ($\leq 15\%$) conversions (not shown). The modification by Ag and Cu resulted in an 8- and 3-fold average decrease in the activity, respectively (see **Figure 4.4**). This is in agreement with reported literature on alkyne hydrogenation where a 5-fold loss in activity was observed upon Cu-modification of Pd in 3-hexyn-ol hydrogenation [73]. Similarly, acetylene hydrogenation rate showed a *ca.* 7-fold decrease over Pd-Ag (relative to monometallic Pd) attributed to the presence of inactive Ag [178]. The activity loss can be attributed to a geometric effects (diminished concentration of active Pd sites on the surface due to dilution by Ag and Cu atoms), that is consistent with the surface presence of Ag and Cu extracted from EDX mapping analyses. Higher activity over Cu- (compared to Ag-) modified Pd NPs can be explained by the differences in the distribution of both metals within the bimetallic NPs: for the same Pd/M molar ratio, the NP surface bears a higher amount of the active metal (Pd) in an alloy compared to a core-shell structure. It is worth noting that the Pd-Ag nanocatalysts fully covered by Ag demonstrated no activity during the initial period of the reaction although the hydrogenation rate increased with time. We focus then our attention on elucidating the source of such catalytic behavior and the results for the unconverted fraction of hydrogen f_{H_2} as a function of time over the Pd_xAg catalysts, where $1.5 \leq x \leq 5.0$, are presented in **Figure 4.5**. It can be clearly seen that, in the case of the $\text{Pd}_{1.5}\text{Ag}$ (with the highest Ag content) sample, no conversion was observed during the first 30 minutes. This period of time with no activity during which the bimetallic NPs undergo

structural modifications to generate the active sites can be defined as *induction period* [50, 179] and depends on the amount of surface Ag, *i.e.* increase induction periods for higher Ag contents (see **Figure 4.5**). We account for this phenomenon based on lack of available (surface) Pd active sites in Pd-Ag NPs at the beginning of the reaction, which results in lack of activity. As the reaction progresses a surface restructuring takes place resulting in the migration of Pd to the NP surface and hydrogen begins to be consumed (*i.e.* the decrease of f_{H_2} in **Figure 4.5**). This hypothesis was confirmed by EDX analysis of the samples post-reaction, *i.e.* surface Pd enrichment relative to the sample pre-reaction. Pd migration to the surface under H_2 atmosphere has been reported for supported Pd-Rh [77], Pd-Pt [77] and Pd-Ag [180-182] bimetallic systems and attributed to the decrease in NP surface energy due to strong Pd-hydrogen interaction as a result of H_2 adsorption. The experimental results were supported by density functional calculations showing up to 15-fold stronger binding energy of hydrogen with Pd than that with Ag [183] resulting in a *ca.* 40 kJ mol⁻¹ gain in energy due to Pd surface segregation (despite the intrinsically lower Ag surface energy of clean surfaces without adsorbed hydrogen) [170, 184].

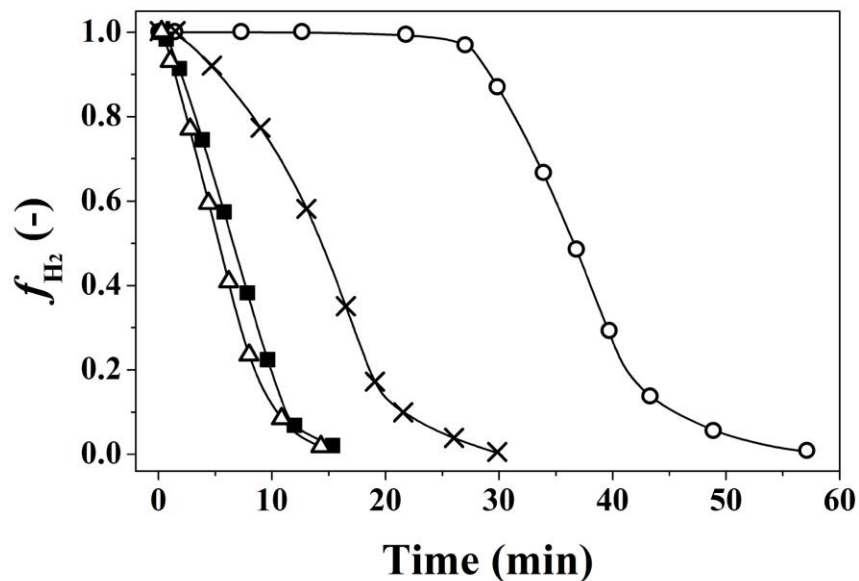


Figure 4.5. Temporal variation of unconverted fraction of hydrogen (f_{H_2}) for reaction over PVP-stabilized Pd-Ag NPs: Pd/Ag molar ratio equal to (Δ) 5.0, (\blacksquare) 3.5, (\times) 2.0 and (\circ) 1.5. *Reaction conditions:* $P_{H_2} = 4$ bar; $T = 353$ K; $C_{DIP} = 3.4 \cdot 10^{-4}$ mol cm $^{-3}$; Pd/DIP molar ratio $\sim 10^{-5}$.

In an attempt to confirm that the Pd-Ag restructuring is linked to Pd-H interaction, a series of additional experiments were conducted over Pd $_{1.5}$ Ag (bearing the highest Ag content) pre-treated in H $_2$ for 30 min in ethanol solution (the time required for appearance of catalytic activity and so linked to the induction period observed for Pd $_{1.5}$ Ag, **Figure 4.5**).

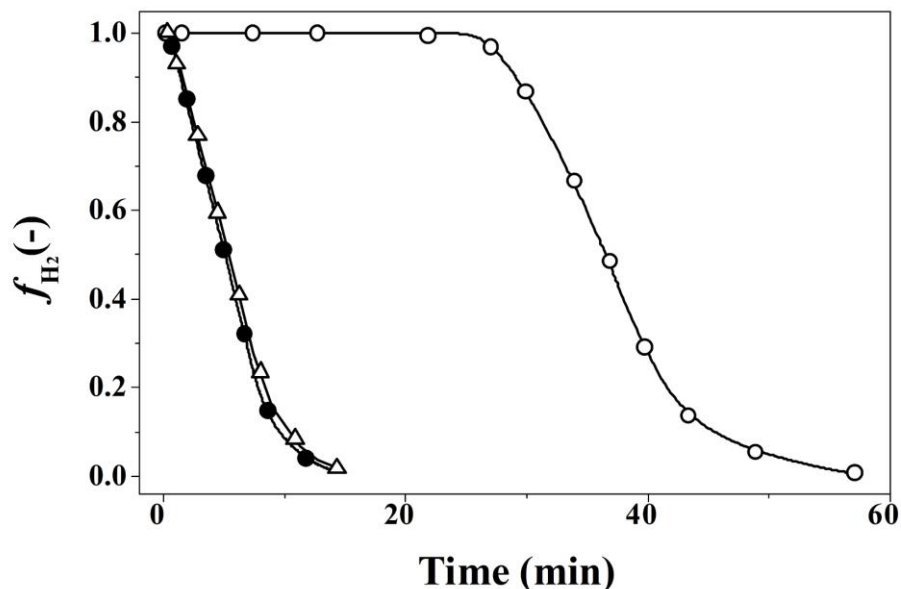


Figure 4.6. Temporal variation of unconverted fraction of hydrogen (f_{H_2}) over bimetallic Pd_{1.5}Ag (non-treated (○) and after hydrogen pre-treatment (●)) and Pd_{5.0}Ag (△) nanoparticles. *Reaction conditions:* $P_{H_2} = 4$ bar; $T = 353$ K;

$$C_{DIP} = 3.4 \cdot 10^{-4} \text{ mol cm}^{-3}; \text{Pd/DIP molar ratio } \sim 10^{-5}.$$

A comparison of activity (expressed as temporal variation of f_{H_2}) for the fresh and H₂-treated Pd_{1.5}Ag is presented in **Figure 4.6** and it is consistent with a lack of induction period for the latter. Moreover, there is an overlap between the f_{H_2} curves over the H₂-treated Pd_{1.5}Ag and fresh Pd_{5.0}Ag (with the lowest Ag content), diagnostic of similar surface properties for both types of NPs characterized by the presence of accessible surface Pd. The results therefore provide a solid evidence of the crucial role of hydrogen in the restructuring. It is worth noting that, to the best of our knowledge, this is the first report showing the restructuring of *unsupported* metal NPs during a *liquid-phase* reaction. It is nonetheless worth flagging the work of Abkhalimov *et al.*

who observed an induction period during liquid-phase hydrogenation of methylviologene over Pt-Ag catalyst that was attributed to hydrogen diffusion through the Ag shell towards the Pt core [179]. However, here we provide the first clear evidence of hydrogen-driven diffusion of Pd to the particle surface to initiate catalytic reaction after the induction period at the beginning of the process.

4.3.3 Catalytic Results over Supported Catalyst

In order to evaluate the potential of the model catalyst formulation (*i.e.* unsupported bimetallic NPs) developed for industrial implementation, *solvent-free* DIP hydrogenation was carried out over monometallic Pd and bimetallic Pd-Ag NPs supported on structured ZnO/SMF prepared by a recently-patented manufacturing technology [16]. We selected Pd_{5.0}Ag as a representative system given that it showed the combined highest activity and selectivity among all the unsupported NPs tested. In order to fully evaluate the performance of Pd-Ag/ZnO/SMF, we compared the catalytic response with that over the benchmark Lindlar catalyst under the same reaction conditions. The variation of IP selectivity as a function of DIP conversion is presented in **Figure 4.7**. On one hand, both ZnO/SMF-supported catalysts showed higher IP selectivity than Lindlar catalyst. The superior performance of Pd/ZnO/SMF over commercial catalyst can be attributed to the support effect as was previously shown for alkynol hydrogenation [78]. However, a salient feature of the data generated is the drastic difference in IP selectivity for the bimetallic Pd_{5.0}Ag/ZnO/SMF ($S_{IP} = 93\%$) relative to the monometallic Pd/ZnO/SMF ($S_{IP} = 78\%$) and *Lindlar* catalyst ($S_{IP} = 62\%$) at high DIP conversion ($\approx 99\%$). This result shows

that the promising olefin selectivity response achieved over the model (unsupported NPs) extends to the supported systems through the combined modifier/support effect under solvent-free conditions.

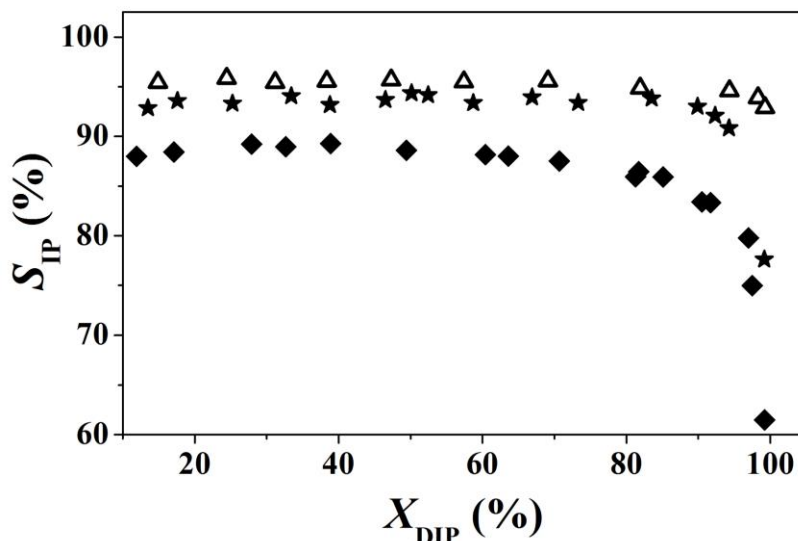


Figure 4.7. Selectivity to IP (S_{IP}) as a function of DIP conversion (X_{DIP}) for reaction over supported Lindlar (◆), Pd/ZnO/SMF (★) and Pd_{5.0}Ag/ZnO/SMF (△) catalysts.

Reaction conditions: $P_{H_2} = 4$ bar; $T = 353$ K; $C_{DIP} = 2.7 \cdot 10^{-3}$ mol cm⁻³; Pd/DIP molar ratio $\sim 10^{-5}$.

The tests over the unsupported NPs indicate that Pd modification with Ag, although results in higher selectivity, is not stable, as the restructuring happens upon the nanocatalyst interaction with hydrogen. On the other hand, the catalyst deactivation is commonly attributed to the active metal poisoning, sintering and/or leaching from the support [64]. In order to evaluate the stability of the supported system, the catalytic performance of Pd_{5.0}Ag/ZnO/SMF in DIP hydrogenation was

monitored over consecutive reaction cycles (50 h in total) and the results are presented in **Figure 4.8**. The data demonstrate a durability where both activity ($-R_{\text{DIP}} = 1.2 \text{ mol}_{\text{DIP}} \text{ mol}_{\text{Pd}}^{-1} \text{ s}^{-1}$) and selectivity ($S_{\text{IP}; X_{\text{DIP}}=50\%} = 96\%$) were constant over 50 h on-stream. The improved stability, relative to the unsupported Pd-Ag NPs, was attributed to the strong anchoring of Pd-containing NPs to ZnO due to partial ZnO reduction with Pd-Zn alloy formation [78].

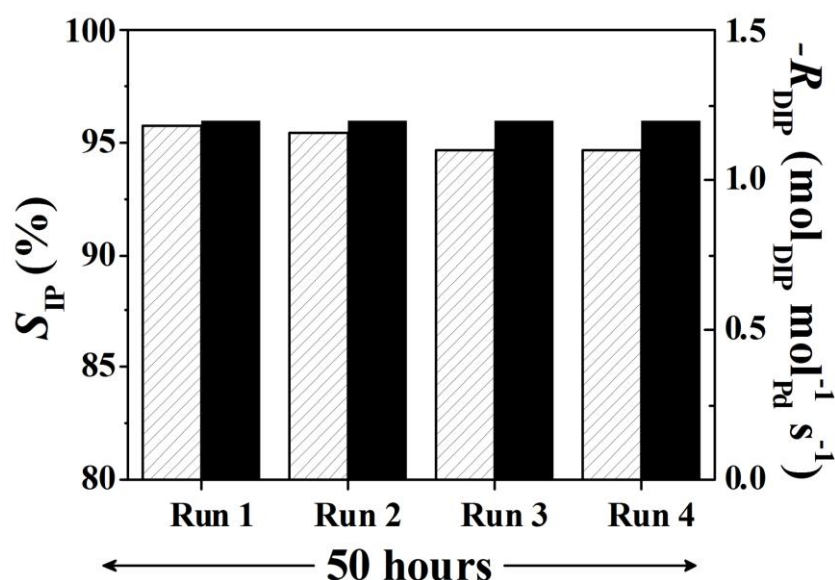


Figure 4.8. Selectivity to IP (hatched bars, $X_{\text{DIP}} = 50\%$) and initial DIP transformation rate (solid bars) for reaction over $\text{Pd}_{5.0}\text{Ag}/\text{ZnO}/\text{SMF}$ catalyst over consecutive runs. *Reaction conditions:* $P_{\text{H}_2} = 4 \text{ bar}$; $T = 353 \text{ K}$; $C_{\text{DIP}} = 2.7 \cdot 10^{-3} \text{ mol cm}^{-3}$; Pd/DIP molar ratio $\sim 10^{-5}$.

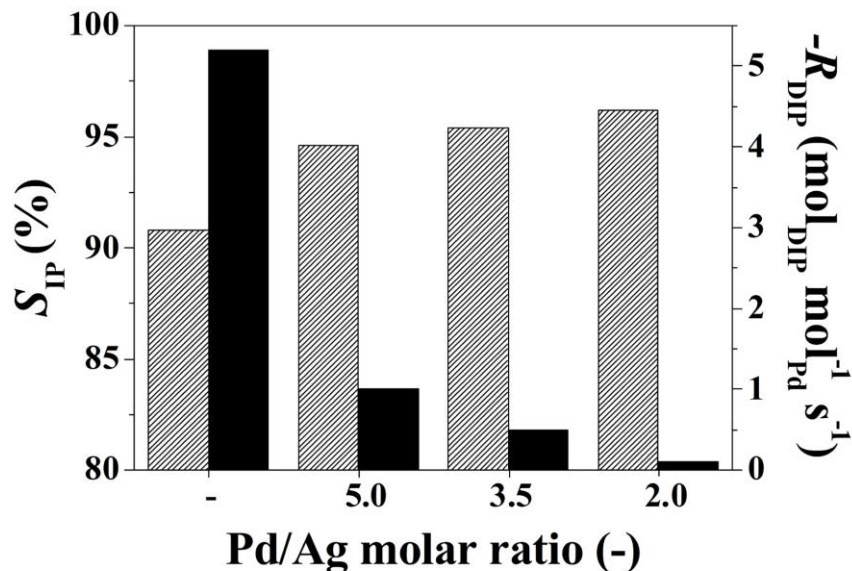


Figure 4.9. Selectivity to IP (hatched bars, $X_{DIP} = 95\%$) and initial DIP transformation rate (solid bars) for reaction over Pd/ZnO/SMF and Pd_xAg/ZnO/SMF where $x = 2.0, 3.5$ and 5.0 . *Reaction conditions:* $P_{H_2} = 4$ bar; $T = 353$ K; $C_{DIP} = 2.7 \cdot 10^{-3}$ mol cm⁻³; Pd/DIP molar ratio $\sim 10^{-5}$.

Given that Ag modification remained after long-term reaction we then evaluated the optimal Pd/Ag ratio and the results obtained in terms of DIP consumption rate and IP selectivity (at $X_{DIP} = 95\%$) are shown in **Figure 4.9**. Higher selectivity over all bimetallic Pd-Ag/ZnO/SMF systems (94 – 96%) as compared to monometallic Pd/ZnO/SMF (91%) was observed where the highest value was obtained using the Pd_{2.0}Ag/ZnO/SMF catalyst (with the highest amount of the Ag). Density functional theoretical (DFT) calculations showed that C≡C/Pd and C=C/Pd binding energies become progressively weaker with increasing Ag content as a result of Ag → Pd charge transfer [185]. A decrease in alkenol adsorption energy inhibits its further

hydrogenation to the corresponding alkanol. In terms of activity, the reaction rates dropped from 5.2 to 0.1 mol_{DIP} mol_{Pd}⁻¹ s⁻¹ at increased Ag contents due to partial blockage of Pd active sites [11]. Accordingly, a good compromise between high selectivity and reasonable activity (1.2 mol_{DIP} mol_{Pd}⁻¹ s⁻¹ was obtained over Lindlar catalyst under the same reaction conditions) could be found by varying the Ag content, the optimum being between Pd/Ag = 3.5-5.0.

4.4 Conclusions

We have studied the Ag⁰ and Cu⁰ promoting effect on both (model) unsupported and (real) ZnO/SMF supported Pd NPs in the selective *semi*-hydrogenation of DIP (as a model alkynol molecule with long ($\geq C_{20}$) hydrocarbon chain). A series of monodispersed mono- (Pd) and bi-metallic Pd-M NPs (M = Ag or Cu) with a wide range of Pd/M molar ratios (1.5, 2.0, 3.5, 5.0) were prepared by colloidal method. A similar metal NPs size is confirmed by STEM for the mono- and bi-metallic NPs (3.4 ± 0.1 nm) regardless of the relative amount of both metals. EDX mapping is consistent with the formation of core-shell and alloy structures for Pd-Ag and Pd-Cu NPs, respectively. A Pd surface segregation was demonstrated for Pd-Ag NPs upon reaction with H₂. Reaction over the unsupported metal NPs reveals an increase in IP alkynol selectivity up to 97% at $X_{DIP} = 99\%$ after Pd modification with Ag.

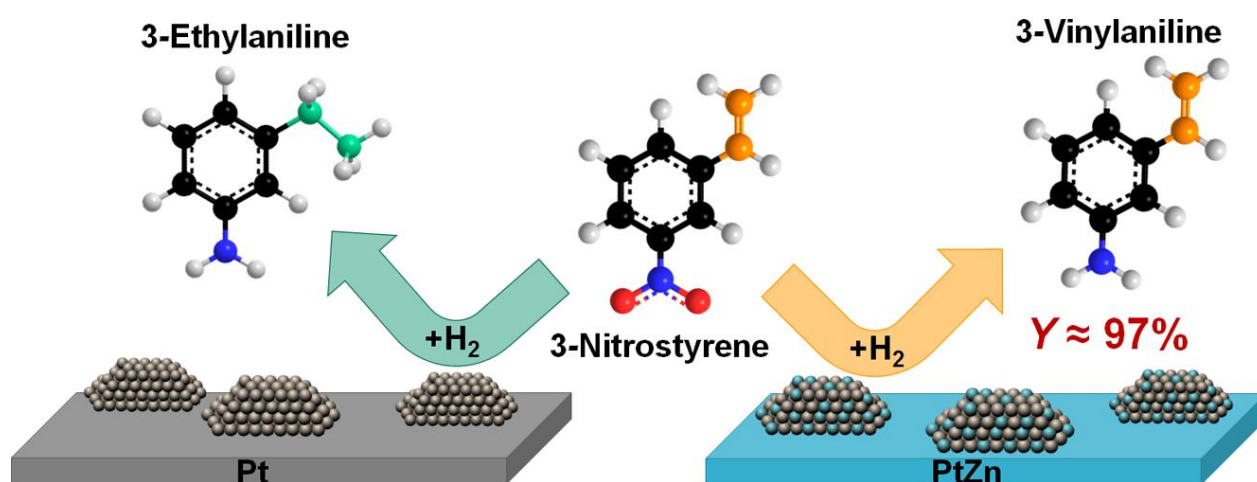
With a view of industrial implementation, the optimized Pd-Ag NPs were deposited on a structured ZnO/SMF support. The drastic increase in IP selectivity for the bimetallic Pd_{5.0}Ag/ZnO/SMF ($S_{IP} = 93\%$) relative to the monometallic Pd/ZnO/SMF

($S_{IP} = 78\%$) and state-of-the-art *Lindlar* catalyst ($S_{IP} = 62\%$) at DIP conversion $\approx 99\%$ with the stable activity during 50 h was demonstrated in *solvent-free* hydrogenation.

The developed structured catalyst is considered suitable for industrial selective *semi*-hydrogenation of long chain alkynols with important applications in the manufacture of vitamins and fine chemicals.

Chapter 5

Hydrogenation of 3-Nitrostyrene: Pt Modification with the Zn



This chapter is based on the following publication: A. Yarulin, C. Berguerand, A. Olasolo-Alonso, I. Yuranov, L. Kiwi-Minsker, *Catal. Today* (Submitted).

Abstract

In this chapter, the promoting effect of Zn on Pt was studied for the liquid-phase 3-NS hydrogenation. Pt/ZnO catalyst containing monodispersed Pt NPs (*ca.* 2.3 nm) promoted the target 3-VA formation ($S_{3-VA} = 97\%$ at $X_{3-NS} \approx 100\%$). Such catalytic performance was attributed to the intermetallic Pt-Zn phase formed *via* reactive metal (Pt) – support (ZnO) interaction during reductive calcinations. Neither of the reference catalysts (Pt/Al₂O₃, Pt/C, Pt/MgO and Pt/TiO₂) provided such high selectivity under the same reaction conditions. The solvent effect was studied showing the highest activity ($TOF = 64 \text{ min}^{-1}$) and 3-VA selectivity ($S_{3-VA} = 97\%$ at $X_{3-NS} \approx 100\%$) in ethanol. The obtained activation energy ($E_a = 40 \text{ kJ mol}^{-1}$) is in agreement with the literature results reported for nitroarenes hydrogenation. The variation of H₂ partial pressure had no significant effect on the products distribution while increasing reaction rate in accordance to the first-order kinetics.

5.1 Introduction

As discussed in Chapter 2, supported Pt catalysts demonstrate high activity in NS hydrogenation [38]. However, in order to achieve high selectivity to VA, an addition of modifiers (H_3PO_2 , $\text{N}(\text{CH}_3)_4\text{Cl}$, FeCl_2) to the reaction mixture is required [3, 37]. More sustainable way to improve Pt selectivity is a modification of the catalyst active phase by a second metal during catalyst preparation or through a metal-support interaction [38]. Pt and Pd supported on ZnO were successful systems to suppress $\text{C}=\text{C} \rightarrow \text{C}-\text{C}$ transformation in hydrogenations of crotonaldehyde, 2-methyl-3-butyn-2-ol, 1-pentyne, 1,3-butadiene [21, 31, 186-188]. However, to the best of our knowledge, there have been no reports demonstrating the modification of Pt catalyst for selective hydrogenation of NS to VA by Pt (active metal) – ZnO (support) interaction.

Another practical way to control activity/selectivity to the desired product is to choose an appropriate solvent [88]. Catalytic response is defined by a solubility of reactants, competitive adsorption and/or mutual interactions of solvent and substrate molecules as well as a solvent-induced catalyst deactivation [37, 189]. NS hydrogenation is typically carried out in toluene or tetrahydrofuran [40, 43, 65]. However, in the light of minimizing the environmental impact, there is a marked trend towards using alcohols and esters [190] as inexpensive solvents, with the added advantage of being readily biodegradable and environmentally attractive for chemical reactions [191, 192].

In this chapter, we report high performance of Pt/ZnO catalyst in selective hydrogenation of 3-NS in comparison with Pt-based benchmark catalysts. The catalyst modification by means of a bimetallic Pt-Zn alloy formation during the catalyst activation was characterized by X-ray photoelectron spectroscopy (XPS), X-ray diffraction (XRD), temperature programmed reduction (TPR) and CO chemisorption. The reaction conditions were optimized in terms of temperature, H₂ pressure and the suitable solvent.

5.2 Experimental

5.2.1 Materials

The following chemicals were used as received without further purification: chloroplatinic acid hexahydrate (Sigma Aldrich; $\geq 99.9\%$), zinc oxide (Sigma Aldrich; $>99.0\%$), magnesium oxide (Fluka; $\geq 98.0\%$), cerium oxide (Acros; 99.9%), iron oxide (Fluka; $>99\%$), titanium oxide (Sigma Aldrich; $\geq 99.0\%$), 3-nitrostyrene (Acros; 97%), dodecane (Acros, 99%), ethanol (Sigma Aldrich; $\geq 99.8\%$), toluene (Sigma Aldrich; $\geq 99.8\%$), isopropanol (Sigma Aldrich; $\geq 99.7\%$), acetonitrile (Sigma Aldrich; $\geq 99.9\%$), methanol (Sigma Aldrich; $\geq 99.8\%$), tetrahydrofuran (Sigma Aldrich; $\geq 99.0\%$), butanol (Acros; $>99\%$). All used gases (H₂, N₂, He, Ar, CO) were of ultra-high purity ($\geq 99.99\%$, Carbogas). The benchmark catalysts: 1% w/w Pt/Al₂O₃ (Alfa Aesar) and 1% w/w Pt/C (Johnson Matthey) were reduced a H₂ flow at 623 K and sieved. A fraction of $<63\ \mu\text{m}$ particle size was used in the experiments.

5.2.2 Catalyst Preparation

The Pt/ZnO catalyst was prepared by an ion-exchange method. An aqueous solution (5 cm³) of H₂PtCl₆ · 6H₂O (1.0 · 10⁻³ mol) was added to 100 cm³ of an aqueous suspension containing 10 g of ZnO and the mixture was stirred for 24 hours at room temperature. Then, the solid was filtered, washed thoroughly with water and ethanol, and dried overnight at room temperature. Pt on MgO and TiO₂ supports was deposited by the same procedure. Prior to use, all catalysts were activated in a stream of H₂ (10 vol. % in Ar, total flow 450 cm³ min⁻¹) at 10 K min⁻¹ to a final temperature in a range of 473 – 773 K, which was maintained for 2 h.

5.2.3 Catalyst Characterization

The Pt content in the catalysts was measured by atomic absorption spectroscopy (AAS) using a Shimadzu AA-6650 spectrometer with an air-acetylene flame after catalyst dissolving in aqua regia (1/3 v/v HNO₃/HCl).

The metal particle size was determined by a transmission electron microscopy (TEM) with a Philips FEI CM12 instrument operated at an accelerating voltage of 120 kV and using Gatan Digital Micrograph 1.82 for data acquisition/manipulation. The specimens were prepared by deposition of a powder dispersion in ethanol on a holey carbon/Cu grid (300 Mesh). Up to 500 individual Pt nanoparticles were counted for each sample and the average diameter (d) was calculated from:

$$d \text{ (nm)} = \frac{\sum_i n_i d_i}{\sum_i n_i} \quad (5.1)$$

where n_i is the number of particles of diameter d_i . The size limit for the detection was *ca.* 1 nm.

Temperature programmed reduction (TPR) in H_2 as well as CO chemisorption were carried out using a commercial AutoChem II (Micromeritics) unit. The samples were loaded into a U-shaped Quartz cell and heated in 10% v/v H_2/N_2 flow ($20\text{ cm}^3\text{ min}^{-1}$) at 5 K min^{-1} to 573 K. The effluent gas passed through a liquid nitrogen/isopropanol trap, and the H_2 consumption were monitored by a thermal conductivity detector (TCD) with data acquisition/manipulation using the Autochem II 2920 V3.03 software. The reduced samples were maintained at the final temperature in the H_2 flow until the TCD signal returned to baseline, swept with a N_2 flow ($65\text{ cm}^3\text{ min}^{-1}$) for 1.5 h, cooled to 323 K, and subjected to CO chemisorption using a pulse (0.3 cm^3) titration procedure. In a blank test, the chemisorption measurements carried out for the ZnO support did not result in any detectable CO uptake.

Powder X-ray diffractograms (XRD) were recorded on a Bruker/Siemens D500 incident X-ray diffractometer (Cu K α radiation) and identified against JCPDS-ICDD standards. The samples were scanned at a rate of $0.02^\circ\text{ step}^{-1}$ over the range $20^\circ \leq 2\theta \leq 90^\circ$ (scan time = 1 s step^{-1}).

X-ray photoelectron spectroscopy (XPS) analyses were conducted using an Axis Ultra instrument (Kratos Analytical) under ultra-high vacuum conditions ($<10^{-11}$ bar) with a monochromatic Al K α X-ray source (1486.6 eV). The source power was maintained at 150 W and the emitted photoelectrons were sampled from a $750 \times 350\text{ }\mu\text{m}^2$ area at a take-off angle = 90° . The analyzer pass energy was 80 eV for survey spectra (0 – 1000 eV) and 40 eV for high-resolution spectra (Pt 4f $_{5/2}$ and 4f $_{7/2}$). The

adventitious carbon 1s peak was calibrated at 284.5 eV and used as an internal standard to compensate any charging effects [193]. Spectra curve fitting and quantification were performed with the CasaXPS software, using relative sensitivity factors provided by Kratos.

5.2.4. Catalytic Hydrogenation

The hydrogenation reactions ($T = 313 - 393$ K; $P_{H_2} = 1 - 15$ bar) were carried out in a commercial semi-batch stirred stainless steel reactor (100 cm³ autoclave, Büchi AG, Uster, Switzerland) equipped with a heating jacket and a pressure controlled H₂ supply system (büchi press-flow gas controller bpc 6002, Büchi AG, Uster, Switzerland). A stainless steel 6-blade disk turbine impeller (equipped with a self-gassing hollow shaft) provided effective agitation at 1500 rpm. A heat exchanger with cooling system (Haake B-N2) was used to control the reaction temperature within ± 1 K using oil (Shell Thermia; thermal conductivity = $0.45 \text{ kJ m}^{-1} \text{ h}^{-1} \text{ K}^{-1}$; specific heat = $2.4 \text{ kJ kg}^{-1} \text{ K}^{-1}$) as a thermal medium. At the beginning of each experiment, a mixture of 3-NS, n-dodecane as internal standard, ethanol (75 cm³) and activated catalyst ($C_{3-NS} = 2.2 \cdot 10^{-5} \text{ mol cm}^{-3}$, $3-NS/Pt \sim 10^2 \text{ mol}_{3-NS} \text{ mol}_{Pt}^{-1}$) were charged into the reactor and flushed three times with N₂ under constant agitation in order to remove O₂. The system was then heated up to the reaction temperature under continuous stirring (ca. 500 rpm). Hydrogen was then introduced, the system was pressurized, and intensive stirring (2000 rpm) was engaged to avoid any external mass transfer limitations [194] (time $t = 0$ for reaction). A noninvasive liquid sampling system via a syringe with in-line filters allowed a controlled withdrawing of aliquots ($\leq 0.25 \text{ cm}^3$) from the reactor.

Repeated reaction runs with the same catalyst batch delivered conversion/selectivity values that were reproducible within $\pm 5\%$. In a series of blank tests, reactions carried out in the absence of the catalyst and/or with the support alone did not result in any measurable conversion.

The composition of the reaction media was analyzed by gas chromatography using a Perkin-Elmer Clarus 500 chromatograph equipped with a programmed split/splitless injector and a flame ionization detector, employing a Stabilwax (Cross-bond Carbowax-PEG, Restek, USA) capillary column (i.d. = 0.32 mm, length 30 m, film thickness = 0.25 μm). Data acquisition/manipulation was performed using the TotalChrom Workstation (Version 6.3.2 for Windows) data system. The concentration of the organic species in the liquid phase was determined from the total mass balance of the reaction mixture.

The conversion of 3-NS ($X_{3\text{-NS}}$) was defined as:

$$X_{3\text{-NS}} (\%) = \frac{C_{3\text{-NS},0} - C_{3\text{-NS}}}{C_{3\text{-NS},0}} \cdot 100. \quad (5.2)$$

The selectivity towards 3-VA ($S_{3\text{-VA}}$) as target product was calculated as

$$S_{3\text{-VA}} (\%) = \frac{C_{3\text{-VA}}}{C_{3\text{-NS},0} - C_{3\text{-NS}}} \cdot 100. \quad (5.3)$$

The catalyst activity was quantified in terms of the initial 3-NS consumption rate ($-R_{3\text{-NS},0}$) determined from a linear regression of the temporal 3-NS concentration profile:

$$-R_{3\text{-NS},0} (\text{mol}_{3\text{-NS}} \text{mol}_{\text{Pt}}^{-1} \text{min}^{-1}) = \frac{(C_{3\text{-NS},0} - C_{3\text{-NS}}) \cdot V}{n_{\text{Pt}} \cdot t_{\text{R}}}. \quad (5.4)$$

$C_{3\text{-NS}}$ and $C_{3\text{-VA}}$ represent 3-NS and 3-VA concentrations, respectively; n_{Pt} – number of moles of Pt, V – reaction mixture volume and t_{R} – reaction time

The specific rate of hydrogenation per active site (turnover frequency, TOF) was obtained from the following equation:

$$\text{TOF} (\text{min}^{-1}) = \frac{-R_{3\text{-NS},0}}{D}, \quad (5)$$

where D (-) is the Pt metal dispersion measured by CO chemisorption.

5.3. Results and Discussion

5.3.1 Catalyst Characterization

The ion-exchange method used in this work to synthesize the Pt/ZnO catalyst allows formation of small monodispersed NPs due to a controlled immobilization of metal precursor anions (PtCl_6^{2-}) on the basic support (ZnO) [50, 59]. A representative TEM micrograph of Pt/ZnO after the reductive treatment at 573 K (**I**) with an associated Pt particle size distribution (**II**) is shown in **Figure 5.1**, confirming the formation of small NPs (*ca.* 2.3 nm) with a narrow size distribution (± 0.7 nm). On the other hand, the Pt particle size determined by CO chemisorption showed a slightly higher mean value (*ca.* 2.8 nm). A small deviation from the TEM results can be linked

to a change of CO/Pt ratio as a result of Pt-Zn alloy formation [195] during H₂-reduction treatments [196, 197].

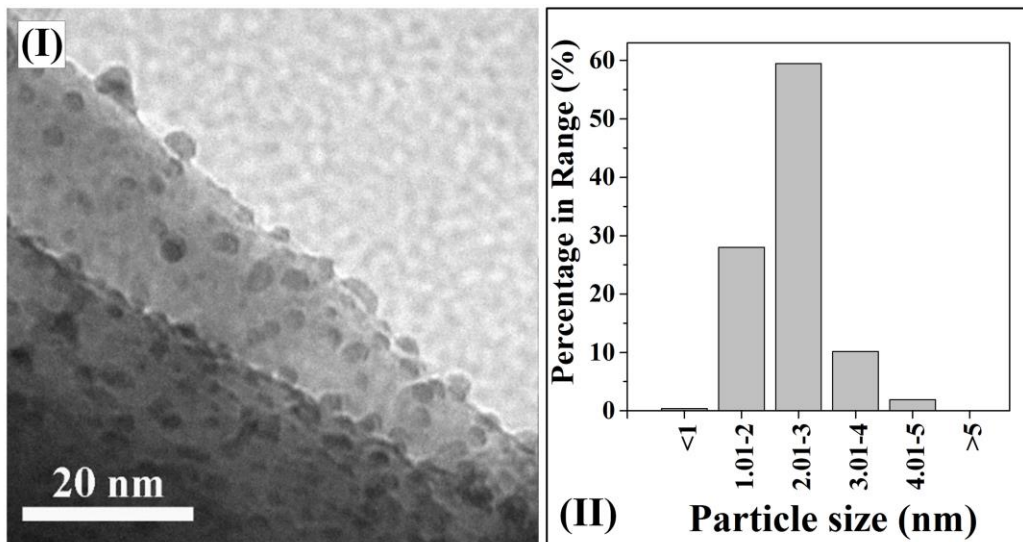


Figure 5.1. Representative TEM image **(I)** with particle size distribution **(II)** of 2 wt.% Pt/ZnO.

In order to corroborate this hypothesis, additional analyses were carried out. The TPR profile recorded for Pt/ZnO catalyst is presented in **Figure 5.2**. A sharp reduction peak with a maximum at 406 K can be attributed to Pt⁰ formation, being within the temperature range (373 – 503 K) assigned to the reduction of oxidized Pt species [198, 199]. The measured amount of consumed H₂ (H₂/Pt molar ratio *ca.* 3) suggests a full Pt⁴⁺ → Pt⁰ transformation, consistent with the results reported for Pt/ZnO and Pt/Al₂O₃ systems [196]. A broad H₂ consumption peak between 450 and 550 K (inset in **Figure 5.2**) can be assigned to the reduction of ZnO that is in contact with Pt [186, 198]. It is worth to note that no significant H₂ consumption/release was observed on a pure ZnO support (**Figure 5.2**). The obtained results clearly indicate a

Pt-catalyzed ZnO reduction, which serves as a reliable sign of the reactive metal (Pt) – support (ZnO) interactions. This is in line with reported literature suggesting catalytic ZnO reduction over Pt and Pd [200, 201].

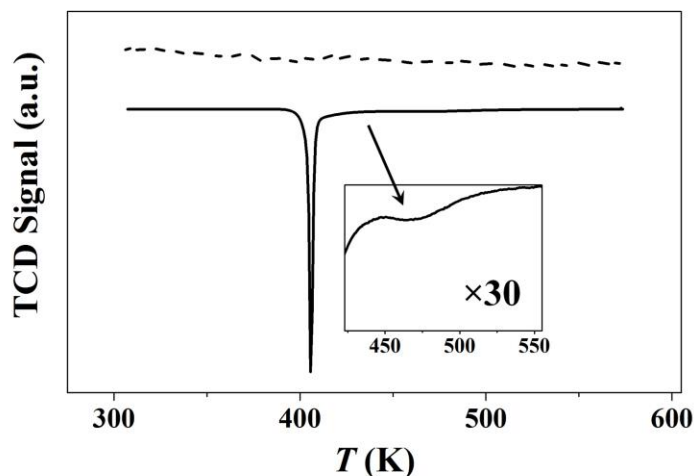


Figure 5.2. TPR profiles obtained for 2 wt.% Pt/ZnO (continuous line) and ZnO (dashed line) at the heating rate of 5 K min⁻¹.

In order to gain insight into the character of Pt-ZnO interaction, we conducted an XRD analysis of this system. A diffractogram of the 2 wt.% Pt/ZnO catalyst activated at 573 K is shown on **Figure 5.3 (I)**. The XRD pattern of ZnO is consistent with the reference table JCPDS-ICDD 036-145. The positions of Pt and Pt-Zn alloy peaks correspond to JCPDS-ICDD 001-1190 and JCPDS-ICDD 006-0604 standards, respectively. Low Pt (and Pt-Zn) peaks intensity is caused by the small particle size and low metal concentration [202]. In order to overcome these limitations, the prepared samples with a higher Pt loading (up to 5 wt. % Pt) were activated at elevated temperatures (up to 773 K). Indeed, high metal content and harsh catalyst treatment conditions are reported to result in larger metal particles [38, 88, 196]. The

recorded XRD patterns corresponding to a Pt-Zn alloy are presented in **Figure 5.3 (II)**. The peak at 41° characteristic of Pt-Zn phase is evidenced for 5% Pt/ZnO reduced at 573 K and is particularly visible for the sample reduced at 773 K. The alloy formation at temperature ≥ 573 K is in agreement with the results reported in literature [81, 203]. Furthermore, Pt-Zn (and Pd-Zn) alloy was previously demonstrated by X-ray absorption spectroscopy (XAS) [187], scanning transmission electron microscopy (STEM) coupled with energy-dispersive X-ray spectroscopy (EDX) [204], Fourier transform infrared spectroscopy (FTIR) of adsorbed CO [201].

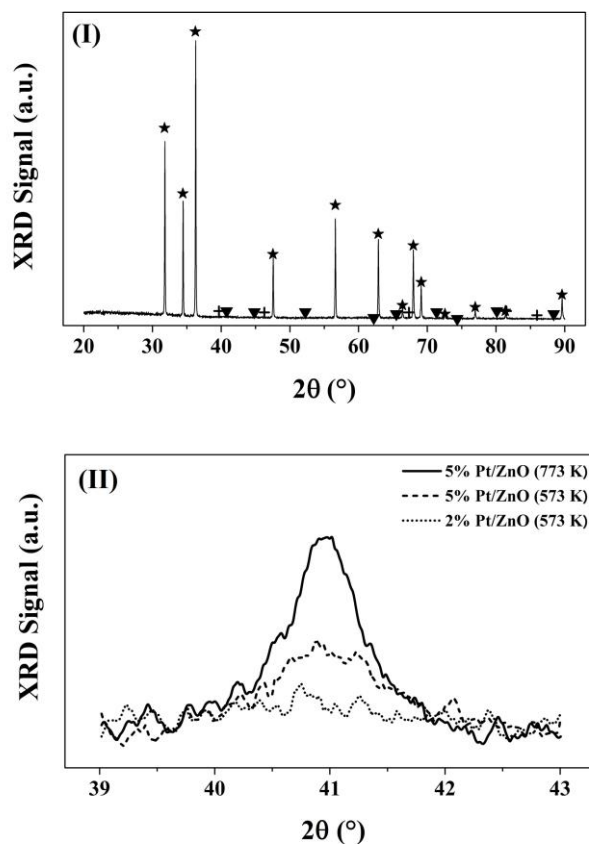


Figure 5.3. (I) XRD spectrum of 2 wt.% Pt/ZnO reduced at 573 K. The symbols represent the JCPDS-ICDD standards for ZnO (★), Pt (●), and PtZn (▼). (II) XRD spectra corresponding to Pt-Zn alloy for Pt/ZnO reduced at 573 and 773 K.

Finally, to shed more light on the electronic properties of the catalytically active phase, the XPS analysis was carried out. It is known that the support can have an effect on the electronic nature of metal NPs [205, 206]. The overview XPS spectrum (not shown) revealed the presence of Pt, Zn, O, and Cl on the catalyst. Given full Pt reduction (based on TPR), O is mostly ascribed to the ZnO support, while traces of Cl can be originated from the Pt precursor. The profile of Pt 4f region for Pt/ZnO reduced at 573 K is shown on **Figure 5.4**. The XPS response is characterized by a doublet with a core level binding energy (BE) equal to 71.4 eV (Pt 4f_{7/2}) and 74.7 eV (Pt 4f_{5/2}). The Pt 4f_{7/2} spectrum suggests the presence of two distinct surface Pt species. The main component shows a BE (71.3 eV) close to the reference for zerovalent Pt (71.1 ± 0.2 eV) [66, 207] whereas the second component exhibits a signal shifted to higher BE (by 0.5 eV) and can be attributed to an intermetallic Pt-Zn phase [208], consistent with our TPR and XRD results.

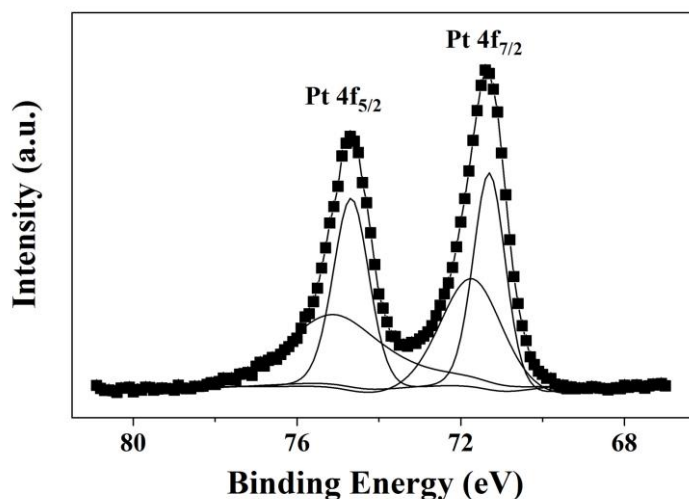


Figure 5.4. XPS spectrum over the Pt 4f region for 2 wt.% Pt/ZnO catalyst.

In summary, monodispersed Pt NPs (*ca.* 2.3 nm) catalyze a partial reduction of ZnO support by H₂ at elevated temperatures (450 – 550 K) followed by incorporation of Zn atoms into Pt NPs (alloying). The combination of TPR, XRD and XPS techniques points to the reactive Pt-ZnO interaction rendering bimetallic Pt-Zn NPs on the ZnO surface.

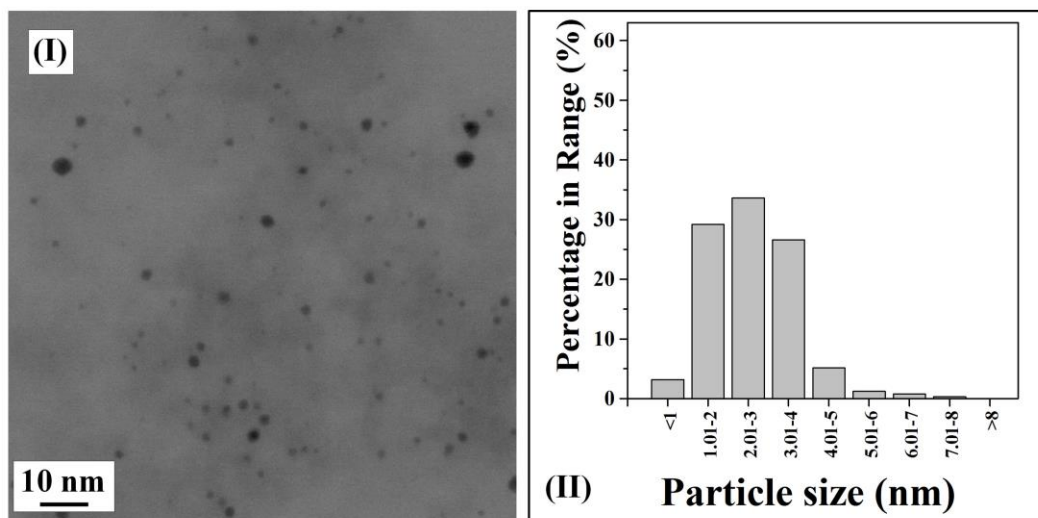


Figure 5.5. (I) Representative TEM image with (II) metal particle size distributions of the benchmark 1 wt.% Pt/C catalyst.

Additionally, the reference commercial (Pt/C and Pt/Al₂O₃) and homemade (Pt/TiO₂ and Pt/MgO) catalysts were tested to establish support characteristics critical for Pt activity and selectivity. TEM analysis of commercial catalysts revealed a spheroidal shape of Pt NPs that is consistent with a cubo-octahedral crystal morphology – the most thermodynamically favorable crystal geometry [66]. A representative micrograph (I) with the corresponding particle size distribution (II) of Pt/C is presented in **Figure 5.5**. The Pt dispersion in the commercial catalysts (confirmed by

CO chemisorption) is close to that of Pt/ZnO, whereas the homemade catalysts contain NPs of 1.4 nm (Pt/TiO₂) and 3.1 nm (Pt/MgO) as revealed by CO chemisorption analysis (Table 5.1).

5.3.2. Influence of Metal-Support Interaction on Catalyst Performance

The catalytic response in 3-NS hydrogenation was tested over Pt-based catalysts under the following reaction conditions: $T_R = 348$ K; $P_{H_2} = 10$ bar; $C_{3-NS} = 2.2 \cdot 10^{-5}$ mol cm⁻³; 3-NS/Pt $\sim 10^2$. The main reaction pathways associated with the catalytic reduction of 3-NS are presented in Figure 2.3. The concentration-time profiles obtained over Pt/ZnO catalyst are shown in Figure 5.6.

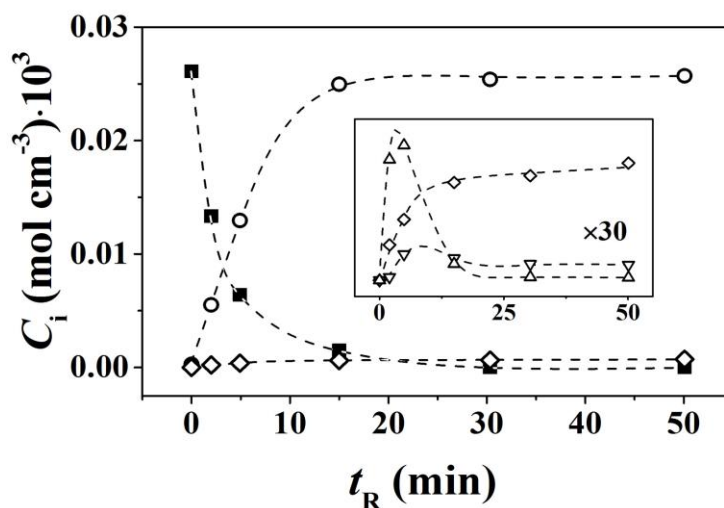


Figure 5.6. Concentration (C_i) - time (t_R) profiles of 3-NS (\blacksquare), 3-VA (\circ), 3-EA (\diamond), 3-ENB (∇) and CP (\triangle) in 3-NS hydrogenation over 2 wt.% Pt/ZnO reduced at 573 K. Reaction conditions: $T = 348$ K; $P_{H_2} = 10$ bar; $C_{3-NS} = 2.2 \cdot 10^{-5}$ mol cm⁻³; 3-NS/Pt $\sim 10^2$.

The results point to a preferential formation of the target 3-VA, while over-hydrogenation to 3-EA is suppressed even after full 3-NS conversion. However, the presence of traces of 3-ENB and CP at moderate 3-NS conversions suggests a complex reaction pathway as shown in **Figure 2.3**. Even though nitroso- and hydroxylaminoarenes were not detected probably due to their thermal instability under the GC analysis conditions [209], we supposed their presence at moderate 3-NS conversions based on the mass balance. It should be noted that all intermediates were further hydrogenated to give 3-VA and/or 3-EA as the only final products.

Regarding the catalytic response exhibited by all catalysts tested (**Table 5.1**), two groups emerge: (I) Pt on carbon and on non-reducible metal oxides (MgO, Al₂O₃), and (II) Pt on reducible oxides (ZnO, TiO₂). The first group promotes exclusively 3-EA formation ($S_{3-VA} = 0$; $X_{3-NS} \approx 100\%$). In marked contrast, the catalysts of the second group demonstrate >50% selectivity towards the target 3-VA at full 3-NS conversion. Notably, reducible supports are known to promote the catalyst performance [196] due to the electronic interaction with the active metal [89], modification of its surface morphology [50] or creation of specific active sites at the metal-support interphase [46]. The promotion is even stronger when the combination of the above-mentioned effects takes place [210]. In this respect, the outstanding results achieved over Pt/ZnO ($S_{3-VA} = 97\%$; $X_{3-NS} \approx 100\%$) correlate well with the characterization results pointing to electronic (XPS) and geometric (CO chemisorption) effects due to the Pt-ZnO interaction. The former effect results in a shift of the electron density from Zn to Pt [211] responsible for a suppressed C=C group adsorption, while the geometric modification of the Pt surface implies the (partial) blocking of the most active but

unselective Pt sites by Zn [11, 195]. This is a very significant finding because, to the best of our knowledge, there have been no reports demonstrating such high VA selectivity in NS hydrogenation over Pt catalysts without addition of any soluble modifiers to the reaction mixture.

Table 5.1. Pt NP size (d_{NP}) and associated results in terms of 3-VA selectivity ($S_{3\text{-VA}}$) at $X_{3\text{-NS}} \approx 100\%$, initial 3-NS consumption rate ($-R_{3\text{-NS},0}$) and turnover frequency (TOF) measured for the supported Pt catalysts. *Reaction conditions:* $T = 348 \text{ K}$; $P_{\text{H}_2} = 10 \text{ bar}$; $C_{3\text{-NS}} = 2.2 \cdot 10^{-5} \text{ mol cm}^{-3}$; $3\text{-NS/Pt} \sim 10^2$.

Catalyst	d_{NP} (nm)	$S_{3\text{-VA}}$ (%)	$-R_{3\text{-NS},0}$ ($\text{mol}_{\text{NS}} \text{mol}_{\text{Pt}}^{-1} \text{min}^{-1}$)	TOF (min^{-1})
Pt/ZnO	2.3 ^a ; 2.8 ^b	97	26	64
Pt/TiO ₂	1.4	53	23	29
Pt/MgO	3.1	0	43	117
Pt/Al ₂ O ₃	2.5 ^a ; 2.7 ^b	0	40	96
Pt/C	2.6 ^a ; 2.8 ^b	0	33	81

Particle size determined by ^aTEM, ^bCO chemisorption.

The catalytic results in terms of the hydrogenation activity are presented in **Table 5.1**. The 3-NS consumption rates calculated for Pt deposited on the non-reducible supports ($33 - 43 \text{ mol}_{\text{NS}} \text{mol}_{\text{Pt}}^{-1} \text{min}^{-1}$) are higher than those calculated over Pt/ZnO ($26 \text{ mol}_{\text{NS}} \text{mol}_{\text{Pt}}^{-1} \text{min}^{-1}$) and Pt/TiO₂ ($23 \text{ mol}_{\text{NS}} \text{mol}_{\text{Pt}}^{-1} \text{min}^{-1}$) catalysts (**Table 5.1**). The difference can be ascribed to a lesser amount of active sites on the modified catalyst

due to the partial Pt surface coverage by Zn or TiO_x [38, 212]. However, a direct comparison of activity over catalysts bearing metal NPs of different sizes is meaningful in terms of the turnover frequency (*TOF*) – a specific reaction rate calculated per active site [66]. The calculated *TOF* values (**Table 5.1**) suggest a general trend of the increased specific activity ($29 \rightarrow 117 \text{ min}^{-1}$) with an increase in Pt NP size ($1.4 \rightarrow 3.1 \text{ nm}$). Given that nitroarenes hydrogenations are commonly considered as structure-sensitive reactions [37], *i.e.*, a catalytic response is controlled by the metal dispersion, the obtained results are consistent with the reaction antipathetic structure sensitivity shown previously by our group for *p*-chloronitrobenzene hydrogenation over Pt catalysts [66]. A distinct response related to the particle size effect is based on the significant changes in the surface structure, *i.e.*, in the relative ratio between surface atoms (*e.g.* corner, edge, plane) having different activities that attend the change in the particle size [19, 59]. Remarkably, we observed different *TOFs* over Pt/ZnO (64 min^{-1}) and benchmark Pt/ Al_2O_3 (96 min^{-1}) and Pt/C (81 min^{-1}) catalysts having similar Pt particle size (*ca.* 2.8 nm based on CO chemisorption). The lower activity over the former catalyst can be invoked by the influence of the reducible support: a shift of the electron density ($\text{Zn}^{\delta+} \rightarrow \text{Pt}^{\delta-}$) results in a modified strength of 3-NS binding to the catalyst surface [196] and, therefore, in a diminished *TOF*, according to the “volcano” curve depicting the metal activity as a function of the adsorption strength [60, 213]. It should be mentioned, that the activity demonstrated by Pt/ZnO is significantly (*ca.* 8 – 300-fold) higher than that reported in literature for NS hydrogenation over the catalysts with similar high selectivity (*i.e.* $S_{3\text{-VA}} = 95 - 99\%$) [40, 43, 46, 65].

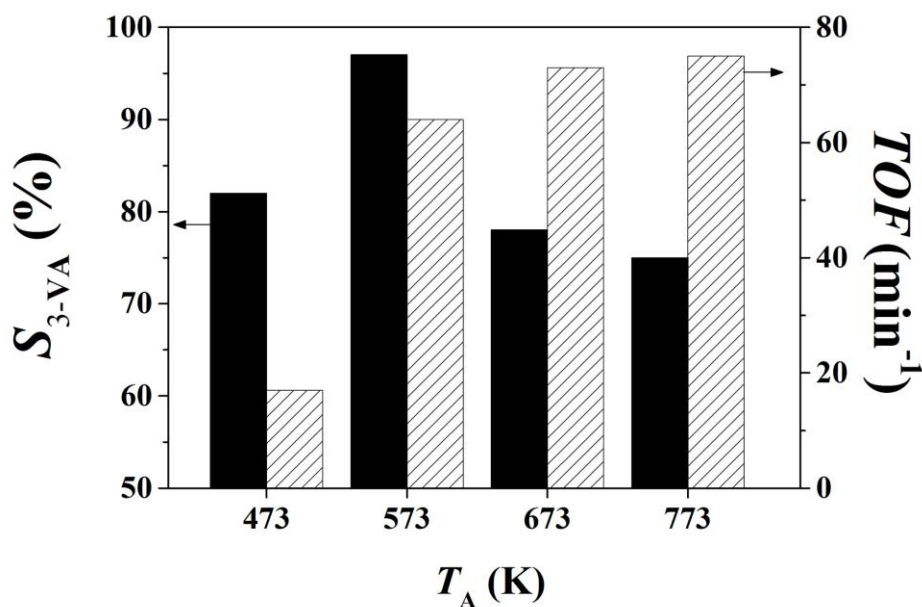


Figure 5.7. Selectivity to 3-VA (S_{3-VA}) at $X_{3-NS} \approx 100\%$ (solid bars) and TOF (hatched bars) as a function of 2%wt. Pt/ZnO activation temperature (T_A). *Reaction conditions:* $C_{3-NS} = 2.2 \cdot 10^{-5} \text{ mol cm}^{-3}$; $3-NS/Pt \sim 10^2$; (I) $P_{H_2} = 10 \text{ bar}$; (II) $T_R = 348 \text{ K}$.

In order to establish the effect of catalyst activation on the catalytic response exhibited by Pt/ZnO, the samples were reduced by H_2 at different temperatures ($T_A = 473 - 773 \text{ K}$). The CO chemisorption analysis showed the concomitant decrease of the Pt dispersion ($0.76 \rightarrow 0.15$) with raising catalyst activation temperature (T_A). A diminution of the Pt specific surface area upon heating is typically ascribed to (I) its partial blockage by Zn due to the alloy formation [11], (II) metal sintering as a result of NPs migration over the catalyst surface [175]. Both effects take place simultaneously as shown by our TEM + CO chemisorption and XRD analyses of Pt/ZnO ($T_A = 573$ and 773 K) (**Figures 5.1 and 5.3 (II)**). The catalytic results of Pt/ZnO ($T_A = 473 - 773 \text{ K}$) point to a maximum of the 3-VA selectivity ($S_{3-VA} = 97\%$;

$X_{3\text{-NS}} \approx 100\%$) over the sample activated at 573 K (**Figure 5.7**). As was evidenced by TPR (inset in **Figure 5.2**), the catalytic ZnO reduction takes place in the range of 450 – 550 K, *i.e.* Pt/ZnO ($T_A = 573$ K) is expected to have a higher degree of intermetallic Pt-Zn phase than Pt/ZnO ($T_A = 473$ K). Therefore, the increase in $S_{3\text{-VA}}$ with activation temperature ($T_A = 473 \rightarrow 573$ K) can be ascribed to the incremental alloy formation. A promotion of the Pt-Zn phase formation at higher catalyst reduction temperatures has been also accounted for the higher selectivity to crotyl alcohol in Pt/ZnO-catalyzed crotonaldehyde hydrogenation [196]. Nevertheless, a further increase of the activation temperature ($T_A = 573 \rightarrow 773$ K) generated NPs with bigger sizes, while not affecting significantly the amount of Pt-Zn alloy (**Figure 5.2**). Therefore, a decrease of $S_{3\text{-VA}}$ with $T_A = 573 \rightarrow 773$ K (**Figure 5.7**) can be attributed to a NP size effect, *i.e.* a variation in the specific hydrogenation rates of C=C- ($TOF_{\text{C=C}}$) and NO₂- (TOF_{NO_2}) groups of 3-NS with the Pt dispersion. Comparing the relative activities of Pt catalyst in styrene and nitrobenzene hydrogenations, Corma *et al.* [38] established that the C=C group hydrogenation is more structure sensitive (compared to NO₂ group), *i.e.* more pronounced increase of $TOF_{\text{C=C}}$ than TOF_{NO_2} with the Pt NP size is determined. Therefore, the lower 3-VA selectivity observed at $T_A > 573$ K can be explained by a rise of $TOF_{\text{C=C}}/TOF_{\text{NO}_2}$ ratio. Regarding the overall TOF measured for the differently activated Pt/ZnO catalysts, a typical antipathetic structure sensitivity is observed: bigger Pt NPs formed at higher T_A demonstrate a higher TOF , suggesting a larger fraction of available active sites on the NP surface.

5.3.3 Effect of Reaction Conditions on Activity and Selectivity

Along with the optimization of the catalyst formulation, a careful choice of the reaction conditions (solvent, reaction temperature and H_2 partial pressure) is crucial for a process development [37, 43]. In the present work, in addition to toluene [46, 88, 214] and tetrahydrofuran [39, 44, 65] commonly used in NS hydrogenation, we employed more “green” solvents (methanol, ethanol, i-propanol and n-butanol) following Pfizer solvent selection guide [191]. The results in terms of 3-VA selectivity and 3-NS consumption rate are presented in **Table 5.2**. A significant increase in target product formation ($S_{3-VA} = 75 \rightarrow 98\%$; $X_{3-NS} \approx 100\%$) was observed following the trend: toluene < tetrahydrofuran < i-propanol \leq n-butanol < ethanol \leq methanol. The results can be tentatively correlated with the solvent polarity. The latter is expressed by the normalized empirical parameter (E_T^N) obtained from spectroscopic measurements that provides accurate characterization data [215] (**Table 5.2**). The E_T^N values are defined as the molar electronic transition energies of dissolved pyridinium N-phenolate betaine dye and range from 0.000 for tetramethylsilane (non-polar molecule) to 1.000 for water (the most polar molecule) [216]. The variation of E_T^N with the type of solvent follows the same trend as S_{3-VA} , *i.e.* the formation of the target product is favored in more polar solvents. This phenomenon has been previously explained by polarization/activation of NO_2 -group of nitroarene on the catalyst surface invoked by the polar solvent, which facilitates its interaction with the adsorbed hydrogen [217].

Table 2: Selectivity to 3-VA ($S_{3\text{-VA}}$) at $X_{3\text{-NS}} \approx 100\%$ and initial consumption rate of 3-NS ($-R_{3\text{-NS},0}$) over Pt/ZnO for 3-NS hydrogenation in solvents with different polarities (E_{T}^{N}).
Reaction conditions: $T = 348 \text{ K}$; $P_{\text{H}_2} = 10 \text{ bar}$; $C_{3\text{-NS}} = 2.2 \cdot 10^{-5} \text{ mol cm}^{-3}$; $3\text{-NS/Pt} \sim 10^2$.

Solvent	$E_{\text{T}}^{\text{N}} \cdot 10^2$ (-)	$S_{3\text{-VA}}$ %	$-R_{3\text{-NS},0}$ ($\text{mol}_{\text{NS}} \text{mol}_{\text{Pt}}^{-1} \text{min}^{-1}$)
Toluene	9.9	75	10
Tetrahydrofuran	20.7	81	7
i-Propanol	57.3	83	11
n-Butanol	60.4	84	14
Ethanol	65.6	97	26
Methanol	76.5	98	13

Regarding the catalyst activity, the values between 7 (in tetrahydrofuran) and 26 (in ethanol) $\text{mol}_{\text{NS}} \text{mol}_{\text{Pt}}^{-1} \text{min}^{-1}$ were established, with no link to any solvent properties. Indeed, the interpretation of solvent effect in catalytic hydrogenations is often complicated due to a combination of various properties involved [215, 218]. Those affecting solvent interactions with substrate and/or catalyst are deemed crucial [215, 219]. For example, Mukherjee *et al.* in the detailed study of solvent effect on Pt-catalyzed citral hydrogenation established the variation of adsorption energies of

substrate, H_2 and solvent, depending on the choice of the latter [220]. Similarly, the calculations of Cárdenas-Lizana *et al.* showed the increase in kinetic constants of chloronitrobenzene hydrogenation in alcohols from pentanol to ethanol, attributed to a competitive solvent *vs.* reactant adsorption on the catalyst [221]. Bertero *et al.* correlated the hydrogenation activity with interactions between the molecules of substrate and solvent [222]. They attributed higher reaction rates obtained in ethanol and 1-propanol (compared to toluene and methanol) to optimal solvent-substrate interactions resulting in low activation energy.

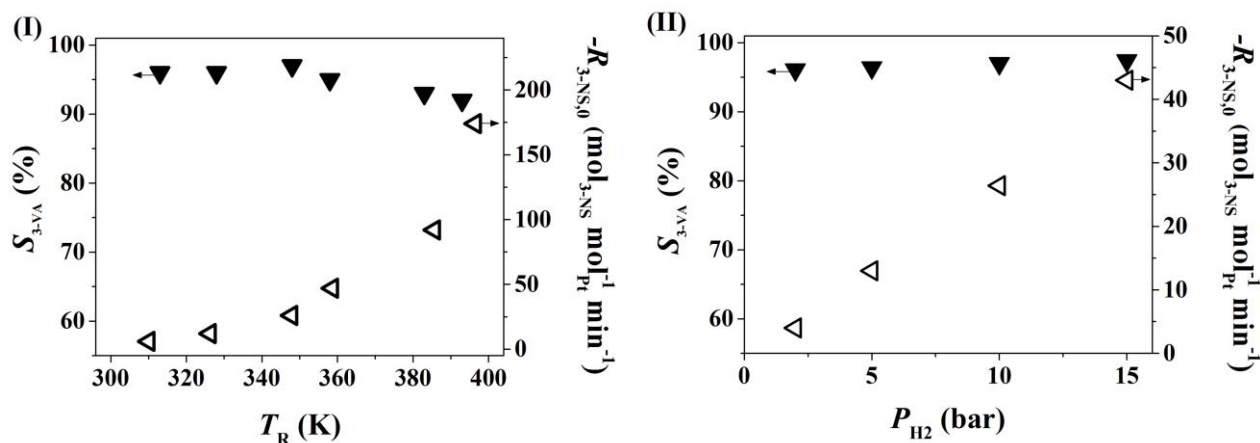


Figure 5.8. Selectivity to 3-VA (S_{3-VA}) at $X_{3-NS} \approx 100\%$ (solid symbols) and initial consumption rate of 3-NS ($-R_{3-NS,0}$; open symbols) for Pt/ZnO as a function of **(I)** reaction temperature (T_R) and **(II)** H_2 partial pressure (P_{H_2}). *Reaction conditions:* $C_{3-NS} = 2.2 \cdot 10^{-5} \text{ mol cm}^{-3}$; $3-NS/Pt \sim 10^2$; **(I)** $P_{H_2} = 10 \text{ bar}$; **(II)** $T_R = 348 \text{ K}$.

The dependence of the catalyst performance on reaction temperature (T_R) was studied in the range of 313 – 393 K. The data obtained in terms of product selectivity point to a slight decrease of S_{3-VA} ($97 \rightarrow 92\%$) at elevated temperatures (**Figure 5.8**

(I)). This is in line with the results reported for 3-NS hydrogenation over Au/TiO₂ ($S_{3\text{-VA}}$ 96.2 \rightarrow 95.9%) and Pt/TiO₂ ($S_{3\text{-VA}}$ 93.1 \rightarrow 69.7%) catalysts at 313 – 393 K [43]. Such catalytic response can be tentatively ascribed to a higher activation barrier of C=C (relative to NO₂) group hydrogenation over bimetallic catalysts, according to the density functional calculations of 3-NS adsorption on Au-TiO_x interfaces [46]. Moreover, preferential 3-VA formation as a result of NO₂-group activation in 3-NS molecule over Pt/ZnO reported herein brings to the same conclusion. Therefore, an increase in T_R would have a stronger effect on C=C group hydrogenation resulting in a greater formation of the 3-EA product and so lower $S_{3\text{-VA}}$. In terms of catalyst activity, higher 3-NS consumption rates were expectedly observed with increasing T_R (**Figure 5.8 (I)**). The apparent activation energy of 3-NS hydrogenation was calculated using the Arrhenius equation. The obtained value (40 kJ mol⁻¹) falls within the range (25 – 49 kJ mol⁻¹) quoted in the literature for hydrogenation of functionalized nitroarenes [47, 223].

The effect of hydrogen partial pressure (P_{H_2}) on the catalyst activity and selectivity in 3-NS hydrogenation was then evaluated. The results shown in **Figure 5.8 (II)** are consistent with constant $S_{3\text{-VA}}$ (97%; $X_{3\text{-NS}} \approx 100\%$) in the P_{H_2} range of 2 – 15 bar. The selectivity independence of P_{H_2} is in a good agreement with the literature where similar catalytic response at full conversion was reported for hydrogenation of functionalized nitroarenes over Pt-based catalysts [224]. This result suggests that while the increase in P_{H_2} brings about a higher H₂ concentration in solution (according to Henry's law) [225] and on a catalyst surface, it contributes little to undesired hydrogenation due to favorable 3-NS adsorption through the NO₂-group. On the other

hand, in terms of activity, the increased H_2 surface concentration results in accelerated 3-NS transformation, as evidenced in **Figure 5.8 (II)**. A monotonic increase of transformation rate with H_2 pressure suggests first reaction order with respect to hydrogen, which is in line with the literature results reported for liquid-phase hydrogenations over supported metal catalysts [43, 225].

In summary, we developed a Pt/ZnO catalyst with the highest combined activity and selectivity for 3-NS hydrogenation. Regarding a potential of industrial implementation, the proposed catalyst outperformed the commercial benchmark Pt/ Al_2O_3 and Pt/C showing 97% yield to the target product with activity close to that of the industrial catalysts.

5.4 Conclusions

The results presented in this chapter support the following conclusions:

(i) Pt deposition on ZnO by ion exchange allowed formation of small NPs (2.3 nm) upon reductive (in H_2) calcination at 573 K. Pt-Zn intermetallic phase was formed *via* alloying as a result of the reactive metal-support interactions, as evidenced by TPR, XRD and XPS analyses.

(ii) The resulting Pt/ZnO catalyst showed an exceptional performance in the liquid-phase 3-NS hydrogenation as compared to the benchmark Pt catalysts, delivering high selectivity towards 3-VA (97%; $X_{3\text{-NS}} \approx 100\%$).

(iii) The catalytic response of Pt/ZnO depends on the catalyst reductive calcination temperature (T_A). The degree of Pt-Zn alloying as well as particle size depend on the T_A and play a crucial role in catalyst performance.

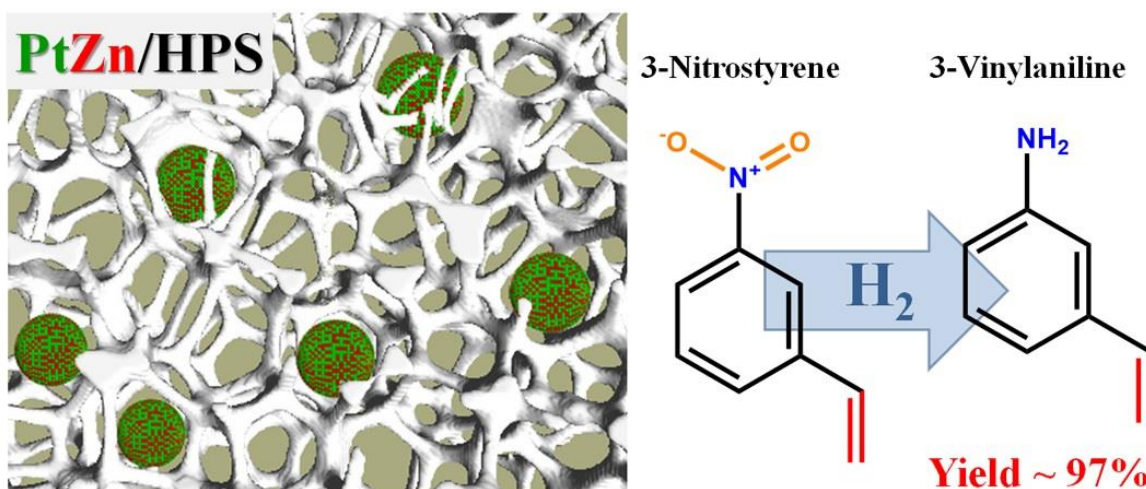
(iv) Ethanol as a solvent and optimal reaction conditions in 3-NS hydrogenation allowed the best results in terms of activity ($26 \text{ mol}_{\text{NS}} \text{ mol}_{\text{Pt}}^{-1} \text{ min}^{-1}$) and 3-VA selectivity (97%; $X_{3\text{-NS}} \approx 100\%$).

(v) The effect of reaction temperature revealed the activation energy of 40 kJ mol^{-1} . The increase of H_2 partial pressure resulted in a higher transformation rate in accordance with a first reaction order.

In summary, a high potential of the developed Pt/ZnO catalyst has been demonstrated and could find multiple applications for selective hydrogenations of functionalized nitroarenes containing vinyl groups.

Chapter 6

Hydrogenation of 3-Nitrostyrene: Pt-Zn Nanoparticles Supported on Porous Polymeric Matrix



This chapter is based on the following publication: A. Yarulin, C. Berguerand, I. Yuranov, F. Cárdenas-Lizana, I. Prokopyeva, L. Kiwi-Minster, *J. Catal.* 321 (2015), 7-12. Reproduced with permission of Elsevier (Copyright 2014).

Abstract

Following the promotion effect of Zn on Pt for 3-NS hydrogenation reported in Chapter 5, the mono- (Pt) and bimetallic (Pt-Zn; Pt/Zn molar ratio = 0.5 – 5.0) NPs were prepared within the HPS support. The nanoporous structure of HPS allows a size control of Pt-Zn NPs by confining them in the cavities (*ca.* 4 – 5 nm) of the polymeric matrix. The TEM analysis showed that the mean size of the resulted metal particles (4.7 nm) corresponds to the HPS pore size. The DRIFTS analysis using CO as a probe molecule suggested the modification of Pt surface and electronic structure invoked by Zn incorporation. Pt/HPS promoted preferential C=C hydrogenation ($S_{3-VA} = 16\%$). Under the same reaction conditions, the formation of 3-VA as a main product was observed over all bimetallic Pt-Zn/HPS catalysts. An increase in Zn content in the bimetallic catalysts resulted in a decrease of activity but enhanced 3-VA selectivity (up to 97%). The stability of Pt-Zn/HPS under reaction conditions was confirmed over repeated reaction runs. Our results demonstrate the Pt modification with Zn as effective means to control 3-VA selectivity, whereas HPS serves as a suitable support to control NP size and avoid metal leaching.

6.1 Introduction

As seen in Chapter 5, ZnO-supported Pt NPs provide a significant suppression of $\text{C}=\text{C} \rightarrow \text{C}-\text{C}$ hydrogenation with concomitant increase of 3-VA selectivity (up to 97% at complete 3-NS conversion). However, while the active phase modification through the metal-support interaction is a successful approach in terms of catalytic results, ZnO as a catalyst carrier has limited applications due to the low specific surface area ($\text{SSA}_{\text{ZnO}} \sim 10 \text{ m}^2 \text{ g}^{-1}$). The support SSA as well as the active metal content determine the average distance between metal particles and therefore their propensity for agglomeration, *i.e.* low support SSA and high metal loading facilitate NPs sintering [59]. A 6-fold increase in Pt particle size ($3 \rightarrow 18 \text{ nm}$) was observed for similarly prepared ZnO-supported catalysts when Pt loading was increased from 1 to 5% [196, 226]. Moreover, higher Pt content ($0.5 \rightarrow 5\%$) resulted in a significantly broader particle size distribution [38]. Given that nitroaromatic compounds hydrogenation is a structure-sensitive (*i.e.* NP size dependent) reaction [66], control over metal dispersion is crucial to the catalytic performance.

The alternative approach of a catalyst design would be an immobilization of Zn-modified Pt NPs on the support devoid of the above-mentioned drawbacks. Cárdenas-Lizana *et al.* [66] demonstrated earlier that monometallic Pt/HPS is an excellent catalytic system for hydrogenation of functionalized nitroaromatic compounds not containing vinyl groups.

In this chapter, Pt-Zn/HPS catalysts with controlled size (4 – 5 nm) and a wide range of Pt/Zn molar ratios were prepared and characterized by critical techniques, such as transmission electron microscopy (TEM) and diffuse reflectance infrared Fourier transform spectroscopy (DRIFTS). The catalysts activity, selectivity and stability over the multiple runs were tested in 3-NS hydrogenation. Our findings over the monodispersed NPs establish the basis for the development of supported Pt catalysts for the selective production of vinylanilines where the product distribution can be controlled by tuning the Pt catalyst properties through the incorporation of a second metal (Zn) and selection of a suitable support.

6.2 Experimental

6.2.1 Materials

Chloroplatinic acid hexahydrate (Sigma Aldrich; $\geq 99.9\%$), zinc nitrate hexahydrate (Sigma Aldrich; $\geq 99.0\%$), n-dodecane (Acros; $\geq 99\%$), ethanol (Sigma Aldrich; $\geq 99.8\%$), acetonitrile (Sigma Aldrich; $\geq 99.9\%$), 3-nitrostyrene (Acros; $\geq 97\%$) were used as received without further purification. All the gases used in this study (H_2 , N_2 , He, Ar) were of ultra-high purity (Carbagas; $\geq 99.99\%$). Beads of hypercross-linked polystyrene (HPS; diameter = 300–900 μm) were supplied by Sigma Aldrich, manufactured by Dow Chemical USA (Optipore V-493).

6.2.2 Catalyst Preparation

The Pt-Zn/HPS catalysts were prepared by incipient wetness impregnation. HPS beads were crashed in a centrifugal ball (2 cm; ágata) mill (Fritsch Pulverisette 6) working with a rotation speed of *ca.* 90 rpm and sieved into a batch of <63 μm average particle diameter. HPS (2 g) was well mixed with 5 cm^3 of an acetonitrile solution containing $\text{H}_2\text{PtCl}_6 \cdot 6\text{H}_2\text{O}$ ($2.1 \cdot 10^{-4}$ mol) as Pt precursor and $\text{Zn}(\text{NO}_3)_2 \cdot 6\text{H}_2\text{O}$ as ZnO precursor and dried in air. The Pt/Zn molar ratio was varied from 0.5 to 5.0. Additionally, Zn-free Pt/HPS catalyst was prepared by the similar procedure. Prior to use, the catalysts were activated in a stream of H_2 (10 vol. % in Ar) heated at 10 K min^{-1} to a final temperature of 573 K which was maintained for 2 h.

6.2.3. Catalyst Characterization

BET area was determined using the Sorptomatic 1990 (Carlo Erba). Prior to analysis, the sample was outgassed at 523 K for 2 h under vacuum ($<5 \cdot 10^{-2}$ Torr). BET area was obtained by N_2 adsorption at 77 K.

The metal (Pt, Zn) loading of HPS was measured by atomic absorption spectroscopy (AAS) using a Shimadzu AA-6650 spectrometer with an air-acetylene flame from the diluted solutions in aqua regia (2/3 v/v HNO_3/HCl).

Metal NP size was determined by transmission electron microscopy (TEM) with a Philips CM20 instrument operated at an accelerating voltage of 200 kV and using Gatan Digital Micrograph 3.4 for data treatment. The specimens were prepared by the deposition of (Pt/HPS, Pt-Zn/HPS) powder on a holey carbon/Cu grid (300 Mesh).

Up to 500 individual NPs were counted for each sample and the mean particle diameter (d) was calculated from:

$$d \text{ (nm)} = \frac{\sum_i n_i d_i}{\sum_i n_i} \quad (6.1)$$

where n_i is the number of particles of diameter d_i .

The properties of Pt/HPS and Pt-Zn/HPS were further studied by Diffuse Reflectance Infrared Fourier Transform Spectroscopy (DRIFTS), using CO as a probe molecule. The spectra were recorded on a Nicolet 8700 spectrometer, equipped with a high-temperature DRIFTS cell and a MCT/A detector with a spectral resolution of 4 cm^{-1} . Prior to CO adsorption, the samples were pre-treated *in situ* in He at 373 K for 1 h and then cooled down to room temperature. An initial infrared spectrum was recorded and was used as a background for further spectra. 5% CO in He was introduced in the cell and the samples were exposed to increasing CO partial pressure (up to a maximum of 20 mbar) followed by evacuation for 40 minutes to remove physisorbed CO. Spectra of adsorbed CO were recorded at 293 K. Each reported spectrum is an average of 128 scans.

6.2.4 Catalytic Hydrogenation

Liquid-phase hydrogenation reactions ($T = 348 \text{ K}$; $P_{\text{H}_2} = 10 \text{ bar}$) were carried out in a commercial semi-batch stirred stainless steel reactor (100 cm^3 autoclave, Büchi AG, Uster, Switzerland) equipped with a heating jacket and a pressure controlled H_2 supply system. Hydrogen consumption in the reactor vessel was monitored online with a gas press-flow controller (BPC-6002, Büchi, Switzerland), and a stainless steel

6-blade disk turbine impeller (equipped with a self-gassing hollow shaft) provided effective agitation at 2000 rpm. A bath recirculator (HAAKE B-N2) was used to stabilize the reaction temperature to within ± 1 K using oil (Shell Thermia; thermal conductivity = $0.45 \text{ kJ m}^{-1} \text{ h}^{-1} \text{ K}^{-1}$; specific heat = $2.4 \text{ kJ kg}^{-1} \text{ K}^{-1}$) as the thermal medium. Before each experiment, a mixture of 3-NS, dodecane as internal standard and the activated catalyst in ethanol (75 cm^3) were charged ($C_{3\text{-NS}} = 2.2 \cdot 10^{-5} \text{ mol cm}^{-3}$, 3-NS/Pt molar ratio $\sim 10^2$) and flushed three times with N_2 under constant agitation in order to remove O_2 . The temperature was set and allowed to stabilize (*ca.* 30 min) under gentle stirring (*ca.* 500 rpm). Hydrogen was then introduced, the system was pressurized, and stirring (at 2000 rpm) was engaged (time $t = 0$ for reaction).

In a series of blank tests, reactions carried out in the absence of catalyst and/or with the support alone did not result in any measurable conversion. The reactions were conducted under conditions that insure the absence of mass and heat transfer limitations as established by the Madon-Boudart test [227]. The catalyst stability was assessed in a sequence of reaction runs. After each cycle, the reactor was cleaned with ethanol and dried. The catalyst was filtered from the reaction mixture, cleaned with ethanol and dried. In order to evaluate possible leaching, after each run the reaction mixture was analyzed by AAS (the procedure is similar to that described above) and the blank test was carried out in the absence of catalyst. Additionally, the catalyst subjected to the stability test was analyzed by AAS.

A liquid sampling system *via* a syringe with in-line filters allowed a controlled withdrawing of aliquots ($\leq 0.25 \text{ cm}^3$) from the reactor. The composition of the reaction/product mixtures was determined using a Perkin-Elmer Clarus 500

chromatograph equipped with a programmed split/splitless injector and a flame ionization detector, employing a Stabilwax (Cross-bond Carbowax-PEG, Restek, USA) capillary column (i.d. = 0.32 mm, length = 30 m, film thickness = 0.25 μm). Data acquisition/manipulation was performed using the TotalChrom Workstation Vers. 6.3.2. (for Windows) chromatography data system. The concentration of the organic species in the liquid phase was determined from the total mass balance of the reaction mixture with n-dodecane as internal standard. The conversion of 3-NS is defined as

$$X_{3\text{-NS}} (\%) = \frac{C_{3\text{-NS},0} - C_{3\text{-NS}}}{C_{3\text{-NS},0}} \cdot 100 \quad (6.2)$$

and selectivity with respect to VA, as the target product, is given as

$$S_{3\text{-VA}} (\%) = \frac{C_{3\text{-VA}}}{C_{3\text{-NS},0} - C_{3\text{-NS}}} \cdot 100 \quad (6.3)$$

In terms of activity, the initial 3-NS transformation rate ($-R_{3\text{-NS}}$) was determined from a linear regression of the temporal 3-NS concentration profiles at low ($\leq 15\%$) conversion:

$$-R_{3\text{-NS}} (\text{mol}_{3\text{-NS}} \text{mol}_{\text{Pt}}^{-1} \text{s}^{-1}) = \frac{(C_{3\text{-NS},0} - C_{3\text{-NS}})V}{n_{\text{Pt}} \cdot t_{\text{R}}} \quad (6.4)$$

where $C_{3\text{-NS}}$ and $C_{3\text{-VA}}$ are the 3-NS and 3-VA concentrations, respectively; n_{Pt} is the number of moles of Pt, V is the reaction mixture volume and t_{R} is the reaction time.

6.3 Results and Discussion

6.3.1 Catalyst Characterization

The commercial HPS used as a catalyst support in this study presents a high SSA ($1065 \text{ m}^2 \text{ g}^{-1}$) and narrow pore size distribution characterized by the predominant presence of small cavities (*ca.* 4 – 5 nm) [66]. The measured HPS surface area did not change after the thermal treatment, consistent with the thermal stability of the hypercross-linked polymer at T up to 623 K reported by the manufacturer [66]. The HPS pore structure determines the active metal dispersion where the broadness of the NPs size distribution depends on homogeneity of the HPS pores. This is illustrated in **Figure 6.1**, where a representative TEM image **(I)** and NPs size distribution **(II)** associated with Pt-Zn/HPS catalyst (Pt/Zn = 1) are shown. The measured metal NPs size is in a good agreement with the pore size of the HPS support. The catalyst exhibits a narrow size distribution of small spherical Pt-Zn NPs with the average diameter of 4.7 nm where significant amount of particles (>60%) falls in the range of 3 – 5 nm. A similar average particle size and distribution was observed for the remaining HPS-supported Pt and Pt-Zn catalysts (Pt/Zn = 0.5, 2.0, 5.0), a result that further confirms that HPS pore size controls metal NP diameter.

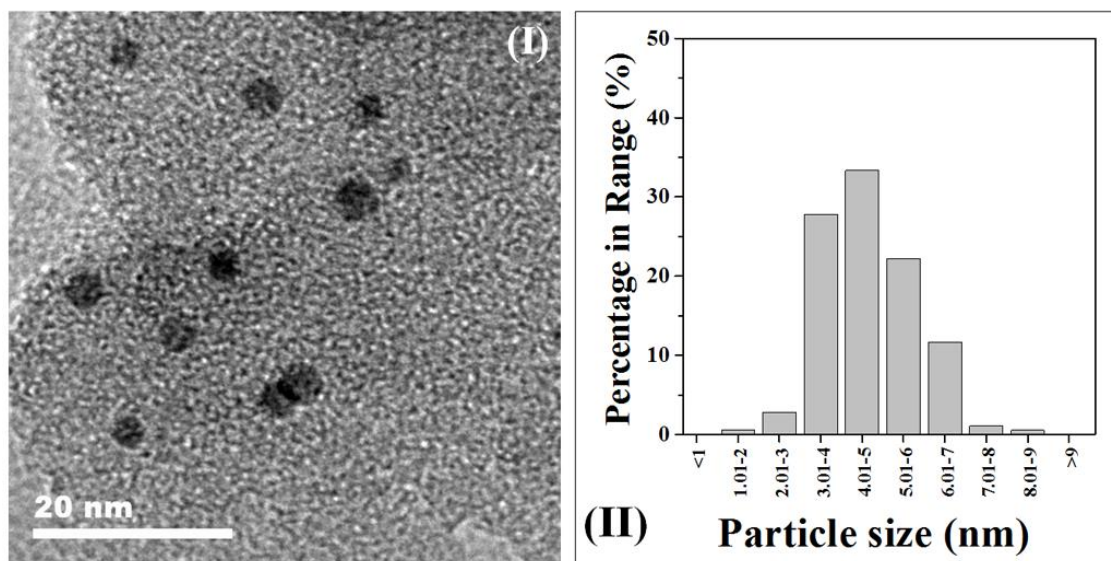


Figure 6.1. (I) Representative TEM image with (II) particle size distribution of 2 wt.% Pt-Zn/HPS.

Prior to the reaction, the catalysts were activated at 573 K under H_2 flow. It was shown in the literature that (i) the $Pt^{4+} \rightarrow Pt^0$ transformation, (ii) Pt-catalyzed ZnO reduction and (iii) Pt-Zn alloying take place at $T \leq 573$ K [204, 228]. The alloy formation was demonstrated in Chapter 5 by XPS and XRD analyses of Pt/ZnO catalyst. In this part, the Pt-Zn NPs bimetallic structure was further assessed by means of IR spectroscopy analysis using CO as a probe molecule. The profile obtained for pure HPS (not shown) was featureless with no evidence of CO adsorption on the support. The spectra of CO adsorption bands in the $2300 - 1800\text{ cm}^{-1}$ region for the selected P_{CO} , as representatives, recorded on Pt/HPS (I) and Pt-Zn/HPS (Pt/Zn molar ratio = 1) (II) are shown in **Figure 6.2**.

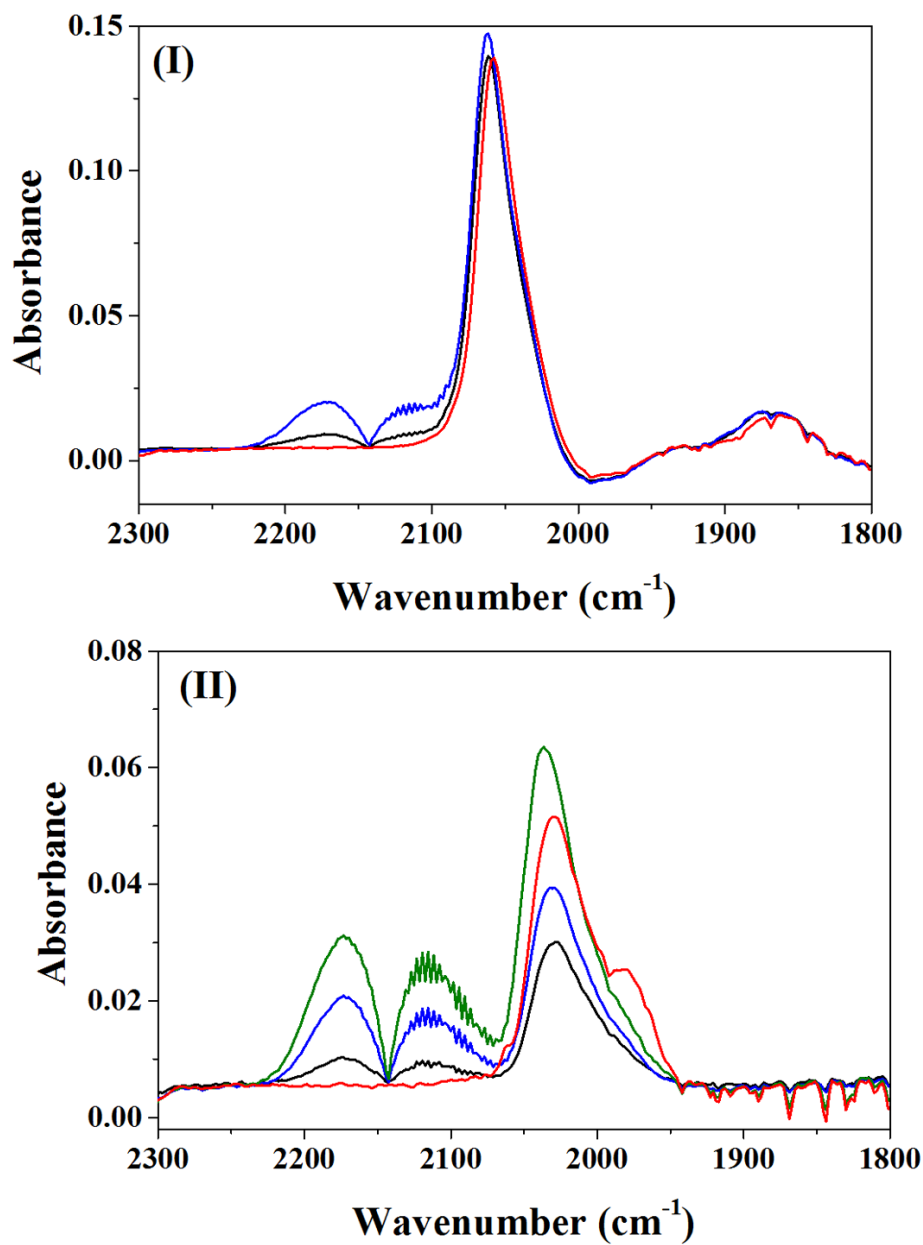


Figure 6.2. DRIFTS spectra of CO adsorbed on **(I)** 2 wt.% Pt/HPS and **(II)** 2 wt.% Pt-Zn/HPS recorded at CO pressure of 2 (—), 8 (—) and 20 (—) mbar as well as after 40 min of CO evacuation (—).

The spectra of the monometallic Pt/HPS catalyst (**Figure 6.2 (I)**) exhibit a high intensity peak at 2061 cm^{-1} characteristic of linearly adsorbed CO [229-231]. The broad peak between 1980 and 1810 cm^{-1} can be ascribed to the multiple-coordinated CO adsorption on the Pt surface [195, 229, 231, 232], while two branches at 2143 cm^{-1} can be associated with CO rotational bands in the gas phase [232]. It is important to note that an increase in CO pressure above 8 mbar did not reveal significant changes of peak intensity indicating a saturation of the Pt surface by adsorbed CO. The evacuation at 293 K resulted in a disappearance of the peaks corresponding to gas phase CO and in a 3 cm^{-1} shift of the main band to the lower frequency zone with a slight decrease (*ca.* 5%) of intensity. The frequency shift can be explained by diminished dipole-dipole coupling interactions between carbonyl groups at adjacent Pt sites as a result of lower CO concentration [195, 232].

The spectra recorded on the bimetallic Pt-Zn/HPS catalyst (**Figure 6.2 (II)**) are characterized by a main peak at 2027 cm^{-1} that shifts towards 2036 cm^{-1} at maximum CO pressure due to increased dipole-dipole interactions [195, 232]. The displacement to lower CO vibration frequency recorded for Pt-Zn/HPS (2036 cm^{-1}) relative to Pt/HPS (2061 cm^{-1}) can be attributed to differences in the back donation of Pt *d* electrons to π^* antibonding orbital of CO [196, 233]. Given that an increase in Pt \rightarrow CO back donation will result in a decrease of the CO bond strength [196], *i.e.* downturn in CO vibration frequency, our results suggest the presence of more electron-rich Pt atoms in the bimetallic Pt-Zn/HPS compared to Pt/HPS. Another possible explanation could be linked to the dilution of surface Pt atoms. The incorporation of Zn atoms into Pt NPs leads to the lower CO frequency in the IR spectrum because of diminished dipole-

dipole coupling interactions of CO adsorbed on isolated Pt sites [195]. Both effects can take place [60, 197] simultaneously as it was reported elsewhere for similar bimetallic systems [11, 15]. Taking this into account, the lower intensity of the main peak and higher ratio of gas-phase/adsorbed CO on Pt-Zn/HPS (relative to Pt/HPS) suggests a modification of surface Pt atoms available in the bimetallic catalyst. Given that particle size is similar in both catalysts, Pt surface depletion can be ascribed to its partial coverage by Zn [114]. This is consistent with reported literature [195] establishing that the formation of inter-metallic compounds involving Pt and another metal (Zn) with a lower enthalpy of sublimation is expected to produce particles in which Zn should occupy the higher energy (*i.e.* lower coordinated) surface sites to reduce the overall surface free energy of the particles. On the other hand, the higher CO saturation pressure (20 mbar) and loss of the main peak intensity after CO evacuation (15%) over Pt-Zn/HPS compared to Pt/HPS (8 mbar and 5%, respectively) suggest lower CO adsorption energy on the former catalyst [231]. The weakening of the CO adsorption strength can be ascribed to $\text{Zn}^{\delta+} \rightarrow \text{Pt}^{\delta-}$ electron transfer [196, 234]. This is in agreement with the work of Rodriguez and Kuhn [203] who showed that the electronic perturbations induced by Zn on Pt reduce its CO chemisorption strength. The broad band of CO adsorption on Pt/HPS in a 1980 – 1810 cm^{-1} region is indicative of heterogeneity in the adsorption sites (*e.g.* bridged/triple mode of CO adsorption on Pt planes and edges), while Pt-Zn/HPS sample shows only a small shoulder at 1980 cm^{-1} after CO evacuation ascribed to bridged CO species on Pt planes [196, 229, 232]. Such deviations in the spectra confirm the different surface structure of the metal NPs in

both catalysts, *i.e.* the NP surface in Pt/HPS is composed of atoms ensembles that are absent on the NP surface of Pt-Zn/HPS.

The results presented suggest the formation of mono- (Pt) and bi-metallic (Pt-Zn) NPs with diameter controlled by the pore size of the HPS support (*ca.* 4.7 nm). The incorporation of Zn results in an increase in Pt electron density (as a result of Zn \rightarrow Pt electron transfer) and amount of surface Pt atoms (from DRIFTS analysis).

6.3.2 Catalytic Results

The catalytic response over mono- (Pt) and bimetallic (Pt-Zn) NPs supported on HPS was tested under the same reaction conditions ($T = 348$ K; $P_{\text{H}_2} = 10$ bar; $C_{3\text{-NS}} = 2.2 \cdot 10^{-5}$ mol cm $^{-3}$; 3-NS/Pt $\sim 10^2$). Hydrogenation of substituted nitroarenes follows a complex reaction mechanism with multiple elementary steps and products distribution that depends on the catalyst and reaction conditions [214, 235, 236] (**Figure 2.3**). Typical products for Pt-catalyzed 3-NS hydrogenation [36, 38] are shown in a simplified reaction scheme (**Figure 6.3**). The formation of the undesired 3-EA can proceed by two routes, *i.e.* through the target 3-VA generation (reaction 1) followed by its over-hydrogenation (reaction 3), or *via* the 3-NS transformation to 3-ENB (reaction 2) leading further to 3-EA (reaction 4) as the fully hydrogenated product.

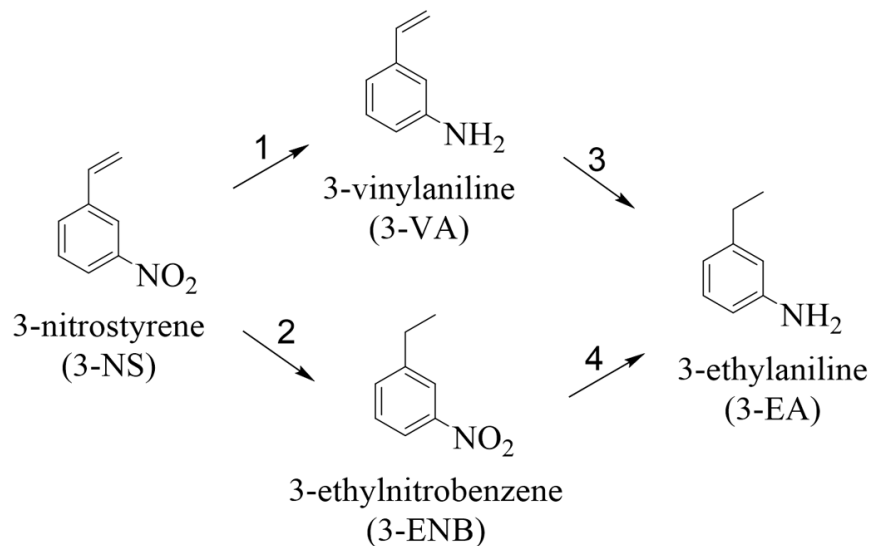


Figure 6.3. Simplified reaction scheme associated with hydrogenation of 3-NS.

The obtained composition *vs.* time profiles for both Pt/HPS (**I**) and Pt-Zn/HPS with a Pt/Zn molar ratio = 1 (**II**), selected as representatives, are shown in **Figure 6.4**. It is worth noting that *ca.* 30% of 3-ENB, azo/azoxyaromatic compounds, nitroso- and hydroxylaminoarenes at $X_{3-NS} \approx 50\%$ were estimated during the course of the reaction based on mass balance (not shown in the graph). Nevertheless, all intermediates were further hydrogenated entirely to one of the two final products (3-VA, 3-EA) as seen in **Figure 6.4**.

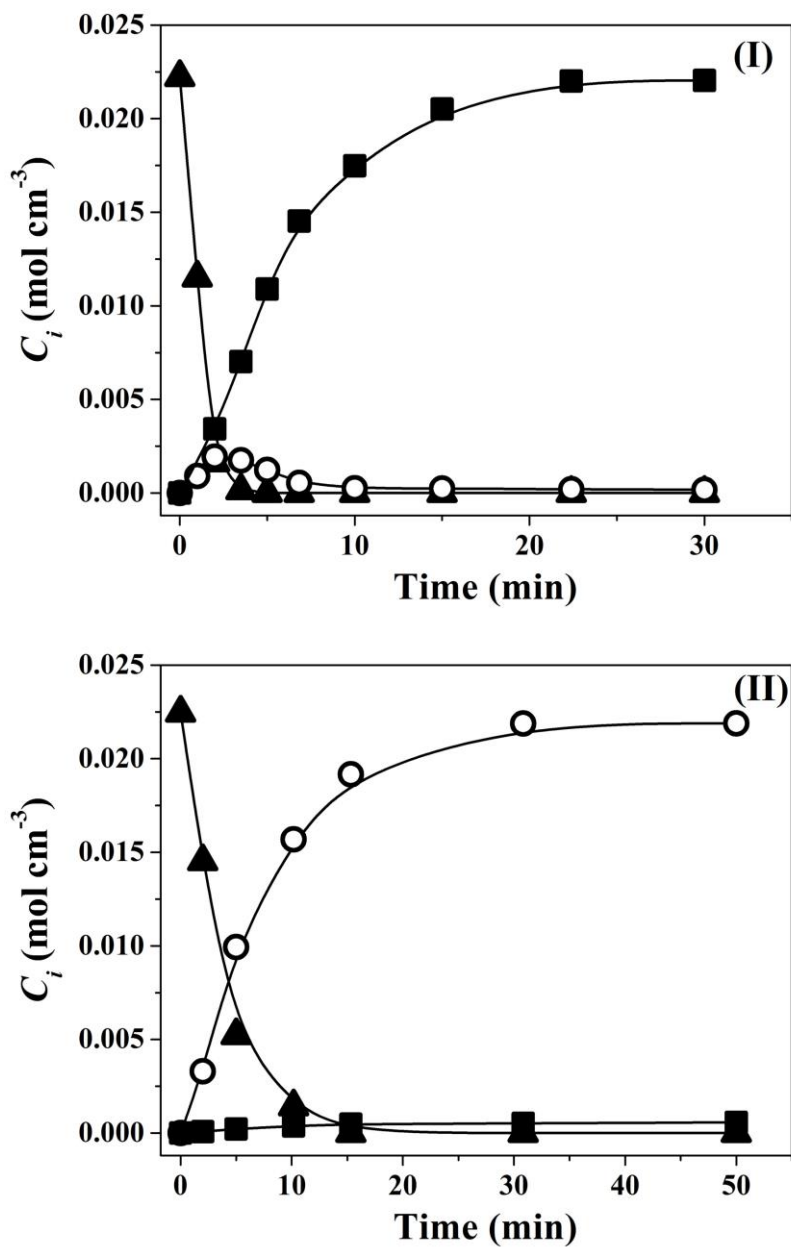


Figure 6.4. Concentrations of 3-NS (▲), 3-VA (○) and 3-EA (■) as a function of time for reaction over (I) 2 wt.% Pt/HPS and (II) 2 wt.% Pt-Zn/HPS. *Reaction conditions:* $T = 348$ K; $P_{H_2} = 10$ bar; $C_{3-NS} = 2.2 \cdot 10^{-5}$ mol cm⁻³; 3-NS/Pt $\sim 10^2$.

The results obtained over the catalysts point to a critical difference in the products distribution. Pt/HPS promotes the over-hydrogenation to 3-EA while the preferential formation of the target 3-VA is observed over Pt-Zn/HPS. We can attribute the remarkable high chemoselectivity over the bimetallic catalyst to the electronic and/or geometric modifications induced by the incorporation of the Zn component. One of the key points in the interpretation of the electronic effects lies in the interplay between the *d*-band orbitals of the metal surface sites with the molecular orbitals of reactants and products [60]. Increased electron density on Pt owing to the coordination with the neighboring Zn atoms (from DRIFT analyses) can lower the adsorption strength of electron-rich vinyl groups inhibiting the C=C reduction step and promoting the formation of 3-VA. A similar rationale has been provided elsewhere to account for the higher selectivity to the target alkene [46, 78, 237] and crotyl alcohol [237] over Zn-modified Pt catalysts. Nonetheless, the increase in 3-VA selectivity can be also linked to modifications in surface composition. The surface of small metal particles is formed by different types of sites (*e.g.* planes, edges, corners) that can have different reactivity [110]. Studies of CO adsorption on Pt showed the strongest bonding on low coordination atoms located on the edges of NP [229]. It follows that the strong adsorption of electron rich unsaturated carbon-carbon bonds can be expected on the low-coordination edge atoms which will lead to a decrease in olefin selectivity [19]. Regarding the 3-NS molecule, adsorption of both nitro- and vinyl-groups on the edge sites was demonstrated theoretically [46]. The increase in selectivity to C=C bond over metal catalysts was attributed to the blocking of the least selective sites by the modifier [15, 18]. Modification of the Pt NPs surface morphology invoked by Zn

incorporation was shown by DRIFTS analysis (**Figure 6.2**). We can therefore associate the increased catalytic performance (up to 97% at $X_{3\text{-NS}} \approx 100\%$) over Pt-Zn/HPS to the contribution of the geometric effect along with the alteration of Pt electronic properties as a result of Zn incorporation.

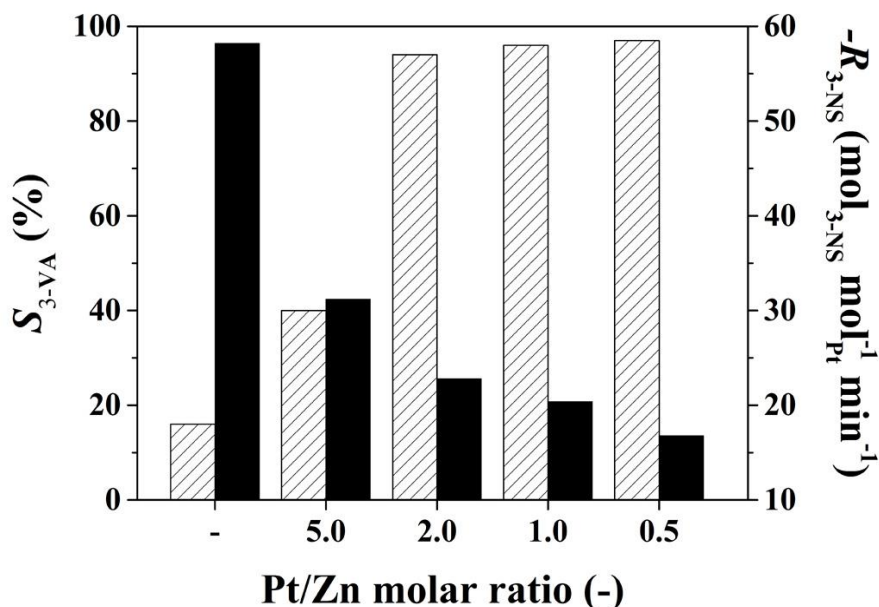


Figure 6.5. Selectivity to 3-VA ($S_{3\text{-VA}}$; hatched bars) at $X_{3\text{-NS}} \approx 100\%$ and initial 3-NS transformation rate ($-R_{3\text{-NS}}$; solid bars) as a function of Pt/Zn molar ratio.

Reaction conditions: $T = 348 \text{ K}$; $P_{\text{H}_2} = 10 \text{ bar}$; $C_{3\text{-NS}} = 2.2 \cdot 10^{-5} \text{ mol cm}^{-3}$; $3\text{-NS/Pt} \sim 10^2$.

Given that Zn modification of Pt promoted 3-VA formation, we then evaluated the catalytic response over the bimetallic catalysts with the extended range of Pt/Zn molar ratios (0.5 – 5.0). The results obtained in terms of 3-VA selectivity (at close to full 3-NS conversion) and 3-NS consumption rates are shown in **Figure 6.5**. While 3-NS hydrogenation over monometallic Pt/HPS results in preferential formation of 3-EA ($S_{3\text{-VA}} = 16\%$; $X_{3\text{-NS}} \approx 100\%$), an increase in Zn content in the bimetallic catalysts shifts

the product distribution towards the formation of 3-VA, to reach 97% for the sample with the lowest Pt/Zn molar ratio (0.5), *i.e.* with the highest Zn content. Based on these results, we can conclude that a rise of Zn amount promotes a stronger shift of electron density towards Pt and/or blocks a larger amount of unselective Pt surface sites. This is supported by density functional theoretical calculations carried out for C=C bond adsorption on Pd [185], that demonstrate the progressive weakening of binding energy with increasing the Ag content in the bimetallic system. Consequently, a decrease in C=C bond adsorption energy inhibits its further (C=C \rightarrow C-C) hydrogenation [210], which is in line with our results shown in **Figure 6.5**.

Regarding the activity, a 3-fold drop of the initial 3-NS transformation rate ($-R_{3-NS} = 58 \rightarrow 17 \text{ mol}_{3-NS} \text{ mol}_{Pt}^{-1} \text{ min}^{-1}$) was observed following the increase amount of Zn (**Figure 6.5**). This is in agreement with the results reported in literature where a loss in activity was observed for nitroarenes hydrogenation upon Pt modification with Ti [38] and Au [43]. The decrease in surface Pt active sites as a result of dilution by inactive Zn can account for the lower catalyst activity [238].

Deactivation of Pt-containing catalysts in nitroarene hydrogenations has been previously reported and was ascribed to metal leaching [66] or restructuring of the bimetallic NPs [13]. Therefore, in order to assess the stability of Pt-Zn/HPS (Pt/Zn = 0.5) catalyst, a series reactions were carried out over four consecutive cycles. The obtained data (**Figure 6.6**) demonstrate constant transformation rate ($-R_{3-NS} \approx 17 \text{ mol}_{NS} \text{ mol}_{Pt}^{-1} \text{ min}^{-1}$) and selectivity towards 3-VA ($S_{3-VA} \approx 97\%$; $X_{3-NS} \approx 100\%$) after four hydrogenation runs. This combination of mechanical and structural stability as well

as high selectivity represents a significant result in terms of potential industrial application of Pt-Zn/HPS.

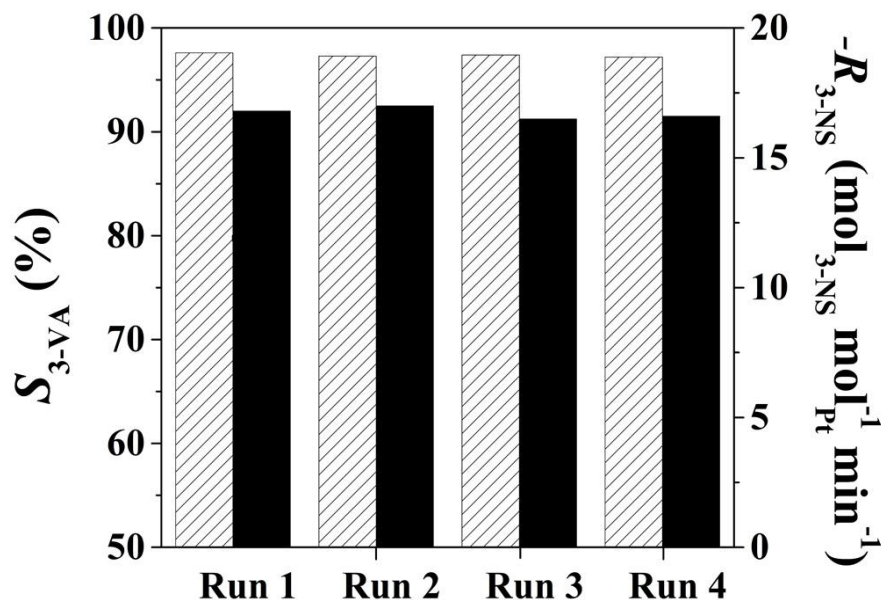


Figure 6.6. Selectivity to 3-VA (S_{3-VA} ; hatched bars) at $X_{3-NS} \approx 100\%$ and initial 3-NS transformation rate ($-R_{3-NS}$; solid bars) for reaction on 2 wt.% Pt-Zn/HPS catalyst over consecutive runs. *Reaction conditions:* $T = 348$ K; $P_{H_2} = 10$ bar; $C_{3-NS} = 2.2 \cdot 10^{-5} \text{ mol cm}^{-3}$; $3-NS/Pt \sim 10^2$.

Our experimental and characterization results demonstrate that activity and selectivity to 3-VA can be tuned by Pt modification with Zn *via* electronic (C=C adsorption strength) and geometric (Pt surface sites separation) effects. The nanoporous HPS ensures strong stabilization of monodispersed Pt-Zn NPs within support avoiding their leaching and rendering stability over consecutive runs.

6.4 Conclusions

The results shown in this chapter support the following conclusions:

(i) Bimetallic Pt-Zn NPs with a narrow particle size distribution (4.7 ± 1.0 nm as confirmed by HRTEM) are prepared within HPS pores.

(ii) Upon addition of Zn to Pt, a significant increase in 3-VA selectivity (from 16% up to 97% at $X_{3-NS} \approx 100\%$) is attained. This is attributed to the Pt^0 surface sites separation by Zn^0 (geometric effect) with concomitant modification of the electronic properties ($Zn^{\delta+} \rightarrow Pt^{\delta-}$) as suggested by the DRIFTS of adsorbed CO-probe molecule.

(iii) Pt-Zn/HPS shows high performance over repeated reaction runs without detectable catalyst deactivation or metal leaching.

In summary, HPS is a suitable support allowing a strict size-control over NPs embedded into its pore network. The developed Pt-Zn/HPS catalyst is highly selective and stable being a potential candidate for selective production of vinylanilines at industrial scale.

Chapter 7

General Conclusions and Outlook

This chapter summarizes the outcome of the study and presents general conclusions and outlook.

7.1 Achieved Results

The concept of sustainability has become the focus of considerable attention in the last decades. Chemical processing is undergoing a progressive redefinition in response to increasing restrictions imposed by environmental legislation. As a result, there is now a pressing demand for the development of alternative cleaner routes to target products, where catalysis is established as a fundamental tool. The results presented in this thesis contribute to the development of a strategy for the design of sustainable catalytic processes.

In the first step, the effect of NP size on the catalyst performance was analyzed for a series of monodispersed Pd colloidal NPs (2.1 – 9.8 nm) as model catalysts in the liquid-phase hydrogenation of DIP and MBY. This study extended the boundaries of structure sensitivity towards smaller metal particles with a special emphasis on the less studied 2 – 3 nm region. The structural changes of the NP surface are the most pronounced in this critical size range, which has the highest impact on the catalytic response. Indeed, an increase of NP size from 2.1 to 3.0 nm resulted in a 1.5-fold higher *TOF*, whereas a further 3.0 → 9.8 nm raise gave the same 1.5-fold increase in activity. The distinct size effect on hydrogenation performance for both α -alkynols is associated with modifications in the adsorption strength linked to the hydrocarbon chain length, as was confirmed by a kinetic modeling based on a Langmuir-Hinshelwood mechanism.

Another tool for modifying surface/electronic structure of the active phase is the incorporation of the second metal. The bimetallic nanocatalysts were prepared by electroless deposition of Ag or Cu on the pre-formed Pd NPs. The Pd-Ag and Pd-Cu model systems were tested in DIP hydrogenation and demonstrated a significant increase in IP selectivity as compared to monometallic Pd NPs (90 → 97% at $X_{\text{DIP}} = 99\%$). This result is attributed to the dilution of the Pd surface sites by Ag or Cu and/or to the modification of Pd electronic properties. In addition to the marked catalytic results, a reaction-driven restructuring of $\text{Pd}_{\text{core}}\text{Ag}_{\text{shell}}$ NPs induced by Pd-H interactions represents a significant finding. This is the first report showing the restructuring of *unsupported* metal NPs during a *liquid-phase* reaction.

The final step of catalyst optimization for alkynol hydrogenation was the deposition of developed NPs on a support, *i.e.* a switch from model systems to a real heterogeneous catalyst. Given that Pd-Ag NPs showed superior results in terms of selectivity, they were deposited on a structured ZnO/SMF support. The drastic increase in IP yield for the bimetallic Pd-Ag/ZnO/SMF ($Y_{IP} = 92\%$) relative to the monometallic Pd/ZnO/SMF ($Y_{IP} = 77\%$) and state-of-the-art *Lindlar* catalyst ($Y_{IP} = 61\%$) with the stable activity during 50 h was demonstrated in *solvent-free* hydrogenation. The outstanding catalyst performance prompted DSM Nutritional Products AG to patent the technology of catalyst manufacturing (*patent WO 2013/060821 A1*).

The development of another catalyst was performed for the selective 3-NS hydrogenation, where Pt was modified by Zn through alloying *via* reactive interaction with ZnO support or by formation of bimetallic Pt-Zn NPs confined within the polymeric matrix of HPS. The resulted Pt/ZnO and Pt-Zn/HPS catalysts demonstrated a boosted 3-VA yields ($0 \rightarrow 97\%$) as compared to the benchmark Pt catalysts. This is attributed to the Pt surface dilution by Zn and modifications of the electronic properties ($Zn^{\delta+} \rightarrow Pt^{\delta-}$) as suggested by a series of characterization techniques (XRD, XPS, DRIFTS). Given the highest combined activity/selectivity achieved over the Pt/ZnO and Pt-Zn/HPS as well as stability over the multiple consecutive runs, these catalysts serve as viable candidates for industrial applications.

7.2 Further Development

Systematic catalyst optimization should address reactions of increased complexity with respect to selectivity, leading to the ultimate development of industrially important target products. Therefore, looking at the broader context, complementary studies should be carried out to extend the limit of catalytic applications towards other classes of reactions (*e.g.* partial hydrogenation of molecules containing $C\equiv C$ groups conjugated with $C=C$ groups), where both high chemo- and stereo-selectivities should be targeted.

With regard to the structure of the bimetallic catalysts, the promotion of catalytic properties is directly related to the spatial distribution of two metals. A very important aspect will be the clear identification of the active site architecture in order to choose the most appropriate synthesis/treatment route, which will selectively yield the specific active sites in the catalytic material. Moreover, the observation of structural evolution of bimetallic NPs under real reaction conditions suggests the importance of *in situ* studies of catalyst surfaces.

Finally, the catalyst development should aim to cover the gap between the laboratory and industrial applications. The research-for-industry should be focused on methods that provide the relevant information in a short time frame, *e.g.* by combining rational catalyst design and high throughput technologies. Although much work has been conducted in this field, the evolving pace of technology development is opening new and exciting ways toward catalyst customization for safer commercial processes.

References

- [1] R.A. van Santen, *Catalysis in Perspective: Historic Review*, in: M. Beller, A. Renken, R.A. van Santen (Eds.), *Catalysis. From Principles to Applications*, Wiley-VCH, Weinheim, 2012, pp. 561-628.
- [2] P. Anastas, N. Eghbali, *Chem. Soc. Rev.* 39 (2010) 301-312.
- [3] H.-U. Blaser, C. Malan, B. Pugin, F. Spindler, H. Steiner, M. Studer, *Adv. Synth. Catal.* 345 (2003) 103-151.
- [4] H.-U. Blaser, *Catal. Today* 60 (2000) 161-165.
- [5] R.A. Sheldon, H.-U. Blaser, *Adv. Synth. Catal.* 345 (2003) 413-413.
- [6] F. Roessler, *Chimia* 57 (2003) 791-798.
- [7] F. Ferrante, A. Prestianni, D. Duca, 118 (2014) 551-558.
- [8] W. Bonrath, J. Medlock, J. Schütz, B. Wüstenberg, T. Netscher, *Hydrogenation in the Vitamins and Fine Chemicals Industry – An Overview*, in: I. Karamé (Ed.), *Hydrogenation*, InTech, Rijeka, 2012, pp. 69-90.
- [9] K. Imamura, K. Nakanishi, K. Hashimoto, H. Kominami, *Tetrahedron* 70 (2014) 6134-6139.
- [10] B. Chen, U. Dingerdissen, J.G.E. Krauter, H.G.J. Lasink Rotgerink, K. Möbus, D.J. Ostgard, P. Panster, T.H. Riermeier, S. Seebald, T. Tacke, H. Trauthwein, *Appl. Catal. A* 280 (2005) 17-46.

- [11] N. López, C. Vargas-Fuentes, *Chem. Commun.* 48 (2012) 1379-1391.
- [12] A. Prestianni, M. Crespo-Quesada, R. Cortese, F. Ferrante, L. Kiwi-Minsker, D. Duca, *J. Phys. Chem. C* 118 (2014) 3119-3128.
- [13] T. Mallat, A. Baiker, *Appl. Catal. A* 200 (2000) 3-22.
- [14] J. Rajaram, A.P.S. Narula, H.P.S. Chawla, S. Dev, *Tetrahedron* 39 (1983) 2315-2322.
- [15] R. Tschan, M.M. Schubert, A. Baiker, W. Bonrath, H. Lansink-Rotgerink, *Catal. Lett.* 75 (2001) 31-36.
- [16] W. Bonrath, T. Mueller, L. Kiwi-Minsker, A. Renken, I. Iouranov, WO2011092280-A1, DSM IP Assets B.V.
- [17] W. Bonrath, L. Kiwi-Minsker, I. Iouranov, WO2012001166-A1, DSM IP Assets B.V.
- [18] M. Crespo-Quesada, F. Cárdenas-Lizana, A.-L. Dessimoz, L. Kiwi-Minsker, *ACS Catal.* 2 (2012) 1773-1786.
- [19] M. Crespo-Quesada, A. Yarulin, M. Jin, Y. Xia, L. Kiwi-Minsker, *J. Am. Chem. Soc.* 133 (2011) 12787-12794.
- [20] E.M. Sulman, *Usp. Khim.* 63 (1994) 981-994.
- [21] E.V. Rebrov, E.A. Klinger, A. Berenguer-Murcia, E.M. Sulman, J.C. Schouten, *Org. Process Res. Dev.* 13 (2009) 991-998.
- [22] Á. Molnár, A. Sárkány, M. Varga, *J. Mol. Catal. A: Chem.* 173 (2001) 185-221.
- [23] I. Horiuti, M. Polanyi, *Trans. Faraday Soc.* 30 (1934) 1164-1172.

-
- [24] P. Baumeister, M. Studer, F. Roessler, *Handbook of Heterogeneous Catalysis*, VCH, Weinheim, 1997.
- [25] D. Mei, P.A. Sheth, M. Neurock, C.M. Smith, *J. Catal.* 242 (2006) 1-15.
- [26] Y. Segura, N. López, J. Pérez-Ramírez, *J. Catal.* 247 (2007) 383-386.
- [27] M. García-Mota, B. Bridier, J. Pérez-Ramírez, N. López, *J. Catal.* 273 (2010) 92-102.
- [28] P.A. Sheth, M. Neurock, C.M. Smith, *J. Phys. Chem. B* 107 (2003) 2009-2017.
- [29] A.N.R. Bos, K.R. Westerterp, *Chem. Eng. Process.* 32 (1993) 1-7.
- [30] A. Borodzinski, G.C. Bond, *Catal. Rev.: Sci. Eng.* 50 (2008) 379-469.
- [31] N. Semagina, M. Grasemann, N. Xanthopoulos, A. Renken, L. Kiwi-Minsker, *J. Catal.* 251 (2007) 213-222.
- [32] J.A. Alves, S.P. Bressa, O.M. Martinez, G.F. Barreto, *Chem. Eng. J.* 125 (2007) 131-138.
- [33] C. Berguerand, I. Yuranov, F. Cárdenas-Lizana, T. Yuranova, L. Kiwi-Minsker, *J. Phys. Chem. C* 118 (2014) 12250-12259.
- [34] J.H. Kim, J.H. Park, Y.K. Chung, K.H. Park, *Adv. Synth. Catal.* 354 (2012) 2412-2418.
- [35] P. Luo, K. Xu, R. Zhang, L. Huang, J. Wang, W. Xing, J. Huang, *Catal. Sci. Technol.* 2 (2012) 301-304.
- [36] M. Stratakis, H. Garcia, *Chem. Rev.* 112 (2012) 4469-4506.
- [37] H.-U. Blaser, H. Steiner, M. Studer, *ChemCatChem* 1 (2009) 210-221.
- [38] A. Corma, P. Serna, P. Concepción, J.J. Calvino, *J. Am. Chem. Soc.* 130 (2008) 8748-8753.

- [39] A. Corma, C. González-Arellano, M. Iglesias, F. Sánchez, *Appl. Catal. A* 356 (2009) 99-102.
- [40] K.-i. Shimizu, Y. Miyamoto, A. Satsuma, *J. Catal.* 270 (2010) 86-94.
- [41] T. Mitsudome, Y. Mikami, M. Matoba, T. Mizugaki, K. Jitsukawa, K. Kaneda, *Angew. Chem. Int. Ed.* 51 (2012) 136-139.
- [42] P.M. Reis, B. Royo, *Tetrahedron Lett.* 50 (2009) 949-952.
- [43] P. Serna, P. Concepcion, A. Corma, *J. Catal.* 265 (2009) 19-25.
- [44] U. Siegrist, P. Baumeister, WO 9532941 A1, Ciba-Geigy AG.
- [45] P. Baumeister, U. Siegrist, M. Studer, EP 0842920 A2, Novartis AG.
- [46] M. Boronat, P. Concepción, A. Corma, S. González, F. Illas, P. Serna, *J. Am. Chem. Soc.* 129 (2007) 16230-16237.
- [47] B. Coq, A. Tijani, F. Figuéras, *J. Mol. Catal.* 68 (1991) 331-345.
- [48] N. Semagina, A. Renken, L. Kiwi-Minsker, *J. Phys. Chem. C* 111 (2007) 13933-13937.
- [49] M. Boudart, *Chem. Rev.* 95 (1995) 661-666.
- [50] M. Che, C.O. Bennett, *Adv. Catal.* 36 (1989) 55-172.
- [51] N. Semagina, L. Kiwi-Minsker, *Catal. Rev.: Sci. Eng.* 51 (2009) 147-217.
- [52] V.V. Pushkarev, K. An, S. Alayoglu, S.K. Beaumont, G.A. Somorjai, *J. Catal.* 292 (2012) 64-72.
- [53] R. van Hardeveld, F. Hartog, *Surf. Sci.* 15 (1969) 189-230.
- [54] N. Semagina, L. Kiwi-Minsker, *Catal. Lett.* 127 (2009) 334-338.
- [55] A. Borodzinski, *Catal. Lett.* 71 (2001) 169-175.

-
- [56] S. Gómez-Quero, F. Cárdenas-Lizana, M.A. Keane, *Ind. Eng. Chem. Res.* 47 (2008) 6841-6853.
- [57] M.A. Aramendía, V. Boráu, I.M. García, C. Jiménez, F. Lafont, A. Marinas, J.M. Marinas, F.J. Urbano, *J. Catal.* 187 (1999) 392-399.
- [58] Z. Karpinski, *Adv. Catal.* 37 (1990) 45-100.
- [59] G.C. Bond, *Chem. Soc. Rev.* 20 (1991) 441-475.
- [60] B. Coq, F. Figueras, *J. Mol. Catal. A: Chem.* 173 (2001) 117-134.
- [61] M.M. Telkar, C.V. Rode, R.V. Chaudhari, S.S. Joshi, A.M. Nalawade, *Appl. Catal. A* 273 (2004) 11-19.
- [62] J.P. Boitiaux, J. Cosyns, S. Vasudevan, *Appl. Catal.* 6 (1983) 41-51.
- [63] Á. Mastalir, Z. Király, F. Berger, *Appl. Catal. A* 269 (2004) 161-168.
- [64] F. Cárdenas-Lizana, M.A. Keane, *J. Mater. Sci.* 48 (2013) 543-564.
- [65] K.-i. Shimizu, Y. Miyamoto, T. Kawasaki, T. Tanji, Y. Tai, A. Satsuma, *J. Phys. Chem. C* 113 (2009) 17803-17810.
- [66] F. Cárdenas-Lizana, C. Berguerand, I. Yuranov, L. Kiwi-Minsker, *J. Catal.* 301 (2013) 103-111.
- [67] R. Ferrando, J. Jellinek, R.L. Johnston, *Chem. Rev.* 108 (2008) 845-910.
- [68] H.-L. Jiang, Q. Xu, *J. Mater. Chem.* 21 (2011) 13705-13725.
- [69] D.C. Huang, K.H. Chang, W.F. Pong, P.K. Tseng, K.J. Hung, W.F. Huang, *Catal. Lett.* 53 (1998) 155-159.
- [70] H. Lindlar, *Helv. Chim. Acta* 35 (1952) 446-456.
- [71] W. Seufert, N. Gotz, H. Theobald, V. Schwendema, DE3438851-A1; EP180108-A2; JP61118328-A; EP180108-B; DE3571968-G, BASF AG.

- [72] M.P.R. Spee, D.M. Grove, G. van Koten, J.W. Geus, *Heterogeneous Catalysis and Fine Chemicals IV*, Elsevier Science B.V., New York, 1997.
- [73] H. Bönemann, W. Brijoux, K. Siepen, J. Hormes, R. Franke, J. Pollmann, J. Rothe, *Appl. Organomet. Chem.* 11 (1997) 783-796.
- [74] J.-M. Yan, X.-B. Zhang, T. Akita, M. Haruta, Q. Xu, *J. Am. Chem. Soc.* 132 (2010) 5326-5327.
- [75] J.H. Liu, A.Q. Wang, Y.S. Chi, H.P. Lin, C.Y. Mou, *J. Phys. Chem. B* 109 (2005) 40-43.
- [76] K. Tedsree, T. Li, S. Jones, C.W.A. Chan, K.M.K. Yu, P.A.J. Bagot, E.A. Marquis, G.D.W. Smith, S.C.E. Tsang, *Nat. Nanotechnol.* 6 (2011) 302-307.
- [77] F. Tao, M.E. Grass, Y. Zhang, D.R. Butcher, J.R. Renzas, Z. Liu, J.Y. Chung, B.S. Mun, M. Salmeron, G.A. Somorjai, *Science* 322 (2008) 932-934.
- [78] M. Crespo-Quesada, M. Grasemann, N. Semagina, A. Renken, L. Kiwi-Minsker, *Catal. Today* 147 (2009) 247-254.
- [79] D. Uzio, G. Berhault, *Catal. Rev.: Sci. Eng.* 52 (2010) 106-131.
- [80] A.Y. Stakheev, L.M. Kustov, *Appl. Catal. A* 188 (1999) 3-35.
- [81] M. Zawadzki, W. Mista, L. Kepinski, *Vacuum* 63 (2001) 291-296.
- [82] F. Cárdenas-Lizana, M. Crespo-Quesada, L. Kiwi-Minsker, *Chimia* 66 (2012) 681-686.
- [83] N. Iwasa, M. Yoshikawa, M. Arai, *Phys. Chem. Chem. Phys.* 4 (2002) 5414-5420.
- [84] S. Penner, M. Stöger-Pollach, R. Thalinger, *Catal. Lett.* 144 (2014) 87-96.

-
- [85] W. Luo, W.H. Doh, Y.T. Law, F. Aweke, A. Ksiazek-Sobieszek, A. Sobieszek, L. Salamacha, K. Skrzypiec, F. Le Normand, A. Machocki, S. Zafeiratos, *J. Phys. Chem. Lett.* 5 (2014) 1837-1844.
- [86] E. Jeroro, J.M. Vohs, *Catal. Lett.* 130 (2009) 271-277.
- [87] A. Corma, P. Serna, *Science* 313 (2006) 332-334.
- [88] S.-i. Fujita, H. Yoshida, K. Asai, X. Meng, M. Arai, *J. Supercrit. Fluids* 60 (2011) 106-112.
- [89] C.-J. Jia, F. Schüth, *Phys. Chem. Chem. Phys.* 13 (2011) 2457-2487.
- [90] D.R. Kennedy, G. Webb, S.D. Jackson, D. Lennon, *Appl. Catal. A* 259 (2004) 109-120.
- [91] X. Zhu, X. Zhao, Z. Ning, X. Sui, *Key Eng. Mater.* 509 (2012) 245-252.
- [92] M. Jin, H. Liu, H. Zhang, Z. Xie, J. Liu, Y. Xia, *Nano Res.* 4 (2011) 83-91.
- [93] Y. Xia, Y. Xiong, B. Lim, S.E. Skrabalak, *Angew. Chem., Int. Ed.* 48 (2009) 60-103.
- [94] A.R. Tao, S. Habas, P. Yang, *Small* 4 (2008) 310-325.
- [95] B. Lim, H. Kobayashi, T. Yu, J. Wang, M.J. Kim, Z.-Y. Li, M. Rycenga, Y. Xia, *J. Am. Chem. Soc.* 132 (2010) 2506-2507.
- [96] J.S. Bradley, G.H. Via, L. Bonneviot, E.W. Hill, *Chem. Mater.* 8 (1996) 1895-1903.
- [97] V.K. LaMer, R.H. Dinegar, *J. Am. Chem. Soc.* 72 (1950) 4847-4854.
- [98] C. Burda, X.B. Chen, R. Narayanan, M.A. El-Sayed, *Chem. Rev.* 105 (2005) 1025-1102.
- [99] T. Teranishi, M. Miyake, *Chem. Mater.* 10 (1998) 594-600.

- [100] B. Lim, M. Jiang, J. Tao, P.H.C. Camargo, Y. Zhu, Y. Xia, *Adv. Funct. Mater.* 19 (2009) 189-200.
- [101] Z. Jiang, J. Xie, D. Jiang, X. Wei, M. Chen, *CrystEngComm* 15 (2013) 560-569.
- [102] N. Semagina, A. Renken, D. Laub, L. Kiwi-Minsker, *J. Catal.* 246 (2007) 308-314.
- [103] S. Biella, F. Porta, L. Prati, M. Rossi, *Catal. Lett.* 90 (2003) 23-29.
- [104] C. Bianchi, F. Porta, L. Prati, M. Rossi, *Top. Catal.* 13 (2000) 231-236.
- [105] J.S. Bradley, E.W. Hill, C. Klein, B. Chaudret, A. Duteil, *Chem. Mater.* 5 (1993) 254-256.
- [106] S. Kataoka, Y. Takeuchi, A. Harada, T. Takagi, Y. Takenaka, N. Fukaya, H. Yasuda, T. Ohmori, A. Endo, *Appl. Catal. A* 427 (2012) 119-124.
- [107] N.E. Musselwhite, S.B. Wagner, K.A. Manbeck, L.M. Carl, K.M. Gross, A.L. Marsh, *Appl. Catal. A* 402 (2011) 104-109.
- [108] S.H.Y. Lo, Y.-Y. Wang, C.-C. Wan, *J. Colloid Interface Sci.* 310 (2007) 190-195.
- [109] J. Le Bars, U. Specht, J.S. Bradley, D.G. Blackmond, *Langmuir* 15 (1999) 7621-7625.
- [110] Y. Li, E. Boone, M.A. El-Sayed, *Langmuir* 18 (2002) 4921-4925.
- [111] B. Lim, J. Wang, P.H.C. Camargo, M. Jiang, M.J. Kim, Y. Xia, *Nano Lett.* 8 (2008) 2535-2540.
- [112] N. Toshima, M. Harada, Y. Yamazaki, K. Asakura, *J. Phys. Chem. C* 96 (1992) 9927-9933.

-
- [113] N. Toshima, P. Lu, *Chem. Lett.* (1996) 729-730.
- [114] K.A. Guy, H. Xu, J.C. Yang, C.J. Werth, J.R. Shapley, *J. Phys. Chem. C* 113 (2009) 8177-8185.
- [115] T. Yuranova, C. Franch, A.E. Palomares, E. Garcia-Bordejé, L. Kiwi-Minsker, *Appl. Catal. B* 123 (2012) 221-228.
- [116] I. Yuranov, A. Renken, L. Kiwi-Minsker, *Appl. Catal. A* 281 (2005) 55-60.
- [117] P. Tribolet, L. Kiwi-Minsker, *Catal. Today* 102 (2005) 15-22.
- [118] D.R. Cahela, B.J. Tatarchuk, *Catal. Today* 69 (2001) 33-39.
- [119] J. De Greef, G. Desmet, G. Baron, *Catal. Today* 105 (2005) 331-336.
- [120] I. Cerri, M. Pavese, G. Saracco, V. Specchia, *Catal. Today* 83 (2003) 19-31.
- [121] L. Kiwi-Minsker, *Chimia* 56 (2002) 143-147.
- [122] P. Tribolet, L. Kiwi-Minsker, *Catal. Today* 105 (2005) 337-343.
- [123] M. Ruta, N. Semagina, L. Kiwi-Minsker, *J. Phys. Chem. C* 112 (2008) 13635-13641.
- [124] V.A. Davankov, M.P. Tsyurupa, *React. Polym.* 13 (1990) 27-42.
- [125] E.M. Sulman, L.Z. Nikoshvili, V.G. Matveeva, I.Y. Tyamina, A.I. Sidorov, A.V. Bykov, G.N. Demidenko, B.D. Stein, L.M. Bronstein, *Top. Catal.* 55 (2012) 492-497.
- [126] S.N. Sidorov, L.M. Bronstein, V.A. Davankov, M.P. Tsyurupa, S.P. Solodovnikov, P.M. Valetsky, E.A. Wilder, R.J. Spontak, *Chem. Mater.* 11 (1999) 3210-3215.

- [127] S.N. Sidorov, I.V. Volkov, V.A. Davankov, M.P. Tsyurupa, P.M. Valetsky, L.M. Bronstein, R. Karlinsey, J.W. Zwanziger, V.G. Matveeva, E.M. Sulman, N.V. Lakina, E.A. Wilder, R.J. Spontak, *J. Am. Chem. Soc.* 123 (2001) 10502-10510.
- [128] L.M. Bronstein, G. Goerigk, M. Kostylev, M. Pink, I.A. Khotina, P.M. Valetsky, V.G. Matveeva, E.M. Sulman, M.G. Sulman, A.V. Bykov, N.V. Lakina, R.J. Spontak, *J. Phys. Chem. B* 108 (2004) 18234-18242.
- [129] P.T. Witte, P.H. Berben, S. Boland, E.H. Boymans, D. Vogt, J.W. Geus, J.G. Donkervoort, *Top. Catal.* 55 (2012) 505-511.
- [130] B. Wuestenberg, R.T. Stemmler, U. Letinois, W. Bonrath, M. Hugentobler, T. Netscher, *Chimia* 65 (2011) 420-428.
- [131] W. Bonrath, M. Eggersdorfer, T. Netscher, *Catal. Today* 121 (2007) 45-57.
- [132] W. Bonrath, T. Netscher, *Appl. Catal. A* 280 (2005) 55-73.
- [133] Y. Sun, Y. Xia, *Science* 298 (2002) 2176-2179.
- [134] M. Ganesan, R.G. Freemantle, S.O. Obare, *Chem. Mater.* 19 (2007) 3464-3471.
- [135] E. Sulman, V. Matveeva, A. Usanov, Y. Kosivtsov, G. Demidenko, L. Bronstein, D. Chernyshov, P. Valetsky, *J. Mol. Catal. A: Chem.* 146 (1999) 265-269.
- [136] X.-Y. Quek, Y. Guan, E.J.M. Hensen, *Catal. Today* 183 (2012) 72-78.
- [137] A. Quintanilla, V.C.L. Butselaar-Orthlieb, C. Kwakernaak, W.G. Sloof, M.T. Kreutzer, F. Kapteijn, *J. Catal.* 271 (2010) 104-114.
- [138] C. Evangelisti, N. Panziera, A. D'Alessio, L. Bertinetti, M. Botavina, G. Vitulli, *J. Catal.* 272 (2010) 246-252.
- [139] H. Hirai, N. Yakura, *Polym. Adv. Technol.* 12 (2001) 724-733.

-
- [140] S. Jujjuri, E. Ding, S.G. Shore, M.A. Keane, *J. Mol. Catal. A: Chem* 272 (2007) 96-107.
- [141] M. Hansen, K. Anderko, *Constitution of Binary Alloys*, 2nd Edition, McGraw-Hill, New York, 1958.
- [142] N.K. Nag, *J. Phys. Chem. B* 105 (2001) 5945-5949.
- [143] S.B. Ziemecki, J.B. Michel, G.A. Jones, *React. Solids* 2 (1986) 187-202.
- [144] C. Amorim, M.A. Keane, *J. Colloid Interface Sci.* 322 (2008) 196-208.
- [145] D. Teschner, J. Borsodi, A. Wootsch, Z. Revay, M. Haevecker, A. Knop-Gericke, S.D. Jackson, R. Schloegl, *Science* 320 (2008) 86-89.
- [146] A. Papp, Á. Molnár, Á. Mastalir, *Appl. Catal. A* 289 (2005) 256-266.
- [147] A. Antony, C. Hakanoglu, A. Asthagiri, J.F. Weaver, *J. Chem. Phys.* 136 (2012) 054702.
- [148] D.M. Ruthven, *Adsorption, Fundamentals*, John Wiley & Sons, Inc, Kirk-Othmer Encyclopedia of Chemical Technology, 2000.
- [149] E. Joannet, C. Horny, L. Kiwi-Minsker, A. Renken, *Chem. Eng. Sci.* 57 (2002) 3453-3460.
- [150] A. Borodzinski, A. Cybulski, *Appl. Catal. A* 198 (2000) 51-66.
- [151] U.K. Singh, M.A. Vannice, *J. Catal.* 191 (2000) 165-180.
- [152] R.I. Macey, G.F. Oster, Berkeley Madonna™ 1997.
- [153] P. Mäki-Arvela, J. Hájek, T. Salmi, D.Y. Murzin, 292 (2005) 1-49.
- [154] D. Mei, M. Neurock, C.M. Smith, *J. Catal.* 268 (2009) 181-195.
- [155] G.E. Ramírez-Caballero, Y. Ma, R. Callejas-Tovar, P.B. Balbuena, *Phys. Chem. Chem. Phys.* 12 (2010) 2209-2218.

- [156] A.V. Ruban, H.L. Skriver, J.K. Nørskov, *Phys. Rev. B* 59 (1999) 15990-16000.
- [157] N. Toshima, Y. Wang, *Langmuir* 10 (1994) 4574-4580.
- [158] J.M. Montejano-Carrizales, M.P. Iñiguez, J.A. Alonso, *Phys. Rev. B* 49 (1994) 16649-16658.
- [159] T. Shibata, B.A. Bunker, Z.Y. Zhang, D. Meisel, C.F. Vardeman, J.D. Gezelter, *J. Am. Chem. Soc.* 124 (2002) 11989-11996.
- [160] A.M. Molenbroek, S. Haukka, B.S. Clausen, *J. Phys. Chem. B* 102 (1998) 10680-10689.
- [161] K.J.J. Mayrhofer, V. Juhart, K. Hartl, M. Hanzlik, M. Arenz, *Angew. Chem., Int. Ed.* 48 (2009) 3529-3531.
- [162] S.M. Holmes, C. Markert, R.J. Plaisted, J.O. Forrest, J.R. Agger, M.W. Anderson, C.S. Cundy, J. Dwyer, *Chem. Mater.* 11 (1999) 3329-3332.
- [163] C. Lange, D. De Caro, A. Gamez, S. Storck, J.S. Bradley, W.F. Maier, *Langmuir* 15 (1999) 5333-5338.
- [164] J. Rebelli, A.A. Rodriguez, S. Ma, C.T. Williams, J.R. Monnier, *Catal. Today* 160 (2011) 170-178.
- [165] J.E.A.M. Vandenmeerakker, *J. Appl. Electrochem.* 11 (1981) 395-400.
- [166] U. Matatov-Meytal, M. Sheintuch, *Catal. Commun.* 10 (2009) 1137-1141.
- [167] P. Lu, T. Teranishi, K. Asakura, M. Miyake, N. Toshima, *J. Phys. Chem. B* 103 (1999) 9673-9682.
- [168] T. Matsushita, Y. Shiraishi, S. Horiuchi, N. Toshima, *Bull. Chem. Soc. Jpn.* 80 (2007) 1217-1225.

-
- [169] V. Ponec, G.C. Bond, *Catalysis by Metals and Alloys*, Elsevier, Amsterdam, 1995.
- [170] O.M. Løvvik, S.M. Opalka, *Surf. Sci.* 602 (2008) 2840-2844.
- [171] S. Lambert, B. Heinrichs, A. Brasseur, A. Rulmont, J.-P. Pirard, *Appl. Catal. A* 270 (2004) 201-208.
- [172] A. Yarulin, I. Yuranov, F. Cárdenas-Lizana, P. Abdulkin, L. Kiwi-Minsker, *J. Phys. Chem. C* 117 (2013) 13424-13434.
- [173] Z.W. Lu, S.H. Wei, A. Zunger, *Phys. Rev. B* 44 (1991) 10470-10484.
- [174] I. Coulthard, T.K. Sham, *Phys. Rev. Lett.* 77 (1996) 4824-4827.
- [175] J.A. Bennett, G.A. Attard, K. Deplanche, M. Casadesus, S.E. Huxter, L.E. Macaskie, J. Wood, *ACS Catal.* 2 (2012) 504-511.
- [176] G. Vilé, D. Baudouin, I.N. Remediakis, C. Copéret, N. López, J. Pérez-Ramírez, *ChemCatChem* 5 (2013) 3750-3759.
- [177] P. Claus, *Top. Catal.* 5 (1998) 51-62.
- [178] Q.W. Zhang, J. Li, X.X. Liu, Q.M. Zhu, *Appl. Catal. A* 197 (2000) 221-228.
- [179] E.V. Abkhalimov, B.G. Ershov, *Colloid J.* 72 (2010) 441-445.
- [180] J. Shu, B.E.W. Bongondo, B.P.A. Grandjean, A. Adnot, S. Kaliaguine, *Surf. Sci.* 291 (1993) 129-138.
- [181] G. Battaglin, E. Cattaruzza, G. De Marchi, F. Gonella, G. Mattei, C. Maurizio, P. Mazzoldi, M. Parolin, C. Sada, I. Calliari, *Nucl. Instrum. Methods Phys. Res. B* 191 (2002) 392-395.
- [182] N.A. Khan, S. Shaikhutdinov, H.J. Freund, *Catal. Lett.* 108 (2006) 159-164.
- [183] P. Matczak, S. Romanowski, *Cent. Eur. J. Chem.* 9 (2011) 474-480.

- [184] S. González, K.M. Neyman, S. Shaikhutdinov, H.-J. Freund, F. Illas, *J. Phys. Chem. C* 111 (2007) 6852-6856.
- [185] P.A. Sheth, M. Neurock, C.M. Smith, *J. Phys. Chem. B* 109 (2005) 12449-12466.
- [186] B.C. Campo, M.A. Volpe, C.E. Gigola, *Ind. Eng. Chem. Res.* 48 (2009) 10234-10239.
- [187] M.W. Tew, H. Emerich, J.A. van Bokhoven, *J. Phys. Chem. C* 115 (2011) 8457-8465.
- [188] A. Sárkány, Z. Zsoldos, B. Furlong, J.W. Hightower, L. Guzzi, *J. Catal.* 141 (1993) 566-582.
- [189] M. Khodadadi-Moghaddam, A. Habibi-Yangjeh, M.R. Gholami, *J. Mol. Catal. A: Chem.* 306 (2009) 11-16.
- [190] R.A. Sheldon, *Green Chem.* 9 (2007) 1273-1283.
- [191] K. Alfonsi, J. Colberg, P.J. Dunn, T. Fevig, S. Jennings, T.A. Johnson, H.P. Kleine, C. Knight, M.A. Nagy, D.A. Perry, M. Stefaniak, *Green Chem.* 10 (2008) 31-36.
- [192] R.A. Sheldon, *Chem. Soc. Rev.* 41 (2012) 1437-1451.
- [193] G. Hopfengärtner, D. Borgmann, I. Rademacher, G. Wedler, E. Hums, G.W. Spitznagel, *J. Electron Spectrosc. Relat. Phenom.* 63 (1993) 91-116.
- [194] A. Bruehwiler, N. Semagina, M. Grasemann, A. Renken, L. Kiwi-Minsker, A. Saaler, H. Lehmann, W. Bonrath, F. Roessler, *Ind. Eng. Chem. Res.* 47 (2008) 6862-6869.

-
- [195] J. Silvestre-Albero, A. Sepúlveda-Escribano, F. Rodríguez-Reinoso, J.A. Anderson, *Phys. Chem. Chem. Phys.* 5 (2003) 208-216.
- [196] F. Ammari, J. Lamotte, R. Touroude, *J. Catal.* 221 (2004) 32-42.
- [197] F. Boccuzzi, A. Chiorino, G. Ghiotti, F. Pinna, G. Strukul, R. Tessari, *J. Catal.* 126 (1990) 381-387.
- [198] J. Hidalgo-Carrillo, M.A. Aramendía, A. Marinas, J.M. Marinas, F.J. Urbano, *Appl. Catal. A* 385 (2010) 190-200.
- [199] A. Borgna, T.F. Garetto, C.R. Apesteguía, F. Le Normand, B. Moraweck, *J. Catal.* 186 (1999) 433-441.
- [200] K.M. Eblagon, P. Heydorn Concepción, H. Silva, A. Mendes, *Appl. Catal. B* 154 (2014) 316-328.
- [201] F. Boccuzzi, A. Chiorino, G. Ghiotti, *Surf. Sci.* 209 (1989) 77-88.
- [202] M. Behrens, R. Schlögl, *X-Ray Diffraction and Small Angle X-Ray Scattering*, in: M. Che, J.C. Védrine (Eds.), *Characterization of Solid Materials and Heterogeneous Catalysts: From Structure to Surface Reactivity*, Wiley-VCH, Weinheim, 2012.
- [203] J.A. Rodriguez, M. Kuhn, *J. Chem. Phys.* 102 (1995) 4279-4289.
- [204] D. Wang, F. Ammari, R. Touroude, D.S. Su, R. Schlögl, *Catal. Today* 147 (2009) 224-230.
- [205] F. Cárdenas-Lizana, Y. Hao, M. Crespo-Quesada, I. Yuranov, X. Wang, M.A. Keane, L. Kiwi-Minsker, *ACS Catal.* 3 (2013) 1386-1396.
- [206] D.R. Baer, D.J. Gaspar, P. Nachimuthu, S.D. Techane, D.G. Castner, *Anal. Bioanal. Chem.* 396 (2010) 983-1002.

- [207] J.Z. Shyu, K. Otto, *Appl. Surf. Sci.* 32 (1988) 246-252.
- [208] J. Silvestre-Albero, F. Coloma, A. Sepúlveda-Escribano, F. Rodríguez-Reinoso, *Appl. Catal. A* 304 (2006) 159-167.
- [209] Q. Wang, C. Wei, L.M. Pérez, W.J. Rogers, M.B. Hall, M.S. Mannan, *J. Phys. Chem. A* 114 (2010) 9262-9269.
- [210] A. Yarulin, I. Yuranov, F. Cárdenas-Lizana, D.T.L. Alexander, L. Kiwi-Minsker, *Appl. Catal. A* 478 (2014) 186-193.
- [211] B. Coq, A. Tijani, F. Figuéras, *J. Mol. Catal.* 71 (1992) 317-333.
- [212] J. Silvestre-Albero, F. Rodríguez-Reinoso, A. Sepúlveda-Escribano, *J. Catal.* 210 (2002) 127-136.
- [213] J.P. Boitiaux, J. Cosyns, S. Vasudevan, *Appl. Catal.* 15 (1985) 317-326.
- [214] A. Corma, P. Concepción, P. Serna, *Angew. Chem. Int. Ed.* 46 (2007) 7266-7269.
- [215] J. Hájek, N. Kumar, P. Mäki-Arvela, T. Salmi, D.Y. Murzin, *J. Mol. Catal. A: Chem.* 217 (2004) 145-154.
- [216] C. Reichardt, *Chem. Rev.* 94 (1994) 2319-2358.
- [217] C. Lu, J. Lu, L. Ma, Q. Zhang, X. Li, *Effect of Solvent Polarity Properties on the Selectivity and Activity for 3,4-Dichloronitrobenzene Hydrogenation over Pd/C Catalyst*, in: Y.X. Wen, F.H. Lei (Eds.), *Advances in Chemical Engineering, Pts 1-3*, 2012, pp. 2379-2383.
- [218] Y. Marcus, *Chem. Soc. Rev.* 22 (1993) 409-416.
- [219] U.K. Singh, M.A. Vannice, *Appl. Catal. A* 213 (2001) 1-24.
- [220] S. Mukherjee, M.A. Vannice, *J. Catal.* 243 (2006) 131-148.

-
- [221] F. Cárdenas-Lizana, S. Gómez-Quero, M.A. Keane, *ChemSusChem* 1 (2008) 215-221.
- [222] N.M. Bertero, A.F. Trasarti, C.R. Apesteguía, A.J. Marchi, *Appl. Catal. A* 394 (2011) 228-238.
- [223] F. Cárdenas-Lizana, S. Gómez-Quero, M.A. Keane, *Catal. Commun.* 9 (2008) 475-481.
- [224] D. He, X. Jiao, P. Jiang, J. Wang, B.-Q. Xu, *Green Chem.* 14 (2012) 111-116.
- [225] A.F. Trasarti, N.M. Bertero, C.R. Apesteguía, A.J. Marchi, *Appl. Catal.* 475 (2014) 282-291.
- [226] M. Consonni, D. Jokic, D.Y. Murzin, R. Touroude, *J. Catal.* 188 (1999) 165-175.
- [227] R.J. Madon, M. Boudart, *Ind. Eng. Chem. Fundam.* 21 (1982) 438-447.
- [228] S. Kaneko, M. Izuka, A. Takahashi, M. Ohshima, H. Kurokawa, H. Miura, *Appl. Catal. A* 427 (2012) 85-91.
- [229] S.K. Cheah, V.P. Bernardet, A.A. Franco, O. Lemaire, P. Gelin, *J. Phys. Chem. C* 117 (2013) 22756-22767.
- [230] J. Raskó, *J. Catal.* 217 (2003) 478-486.
- [231] A. Bourane, O. Dulaurent, D. Bianchi, *J. Catal.* 196 (2000) 115-125.
- [232] J.W. Niemantsvedriet, *Spectroscopy in Catalysis: An Introduction*, Wiley-VCH, Weinheim, 1993.
- [233] F. Thibault-Stazyk, F. Maugé, in: M. Che, J.C. Védrine (Eds.), *Characterization of Solid Materials and Heterogeneous Catalysts: From Structure to Surface Reactivity*, Wiley-VCH, Weinheim, 2012.

[234] I. Chorkendorff, J.W. Niemantsverdriet, *Concepts of Modern Catalysis and Kinetics*, Wiley-VCH, Weinheim, 2007.

[235] E. Merino, *Chem. Soc. Rev.* 40 (2011) 3835-3853.

[236] F. Hamon, F. Djedaini-Pilard, F. Barbot, C. Len, *Tetrahedron* 65 (2009) 10105-10123.

[237] J. Silvestre-Albero, A. Sepúlveda-Escribano, F. Rodríguez-Reinoso, J.A. Anderson, *J. Catal.* 223 (2004) 179-190.

[238] Z. Bodnar, T. Mallat, I. Bakos, S. Szabo, Z. Zsoldos, Z. Schay, *Appl. Catal. A* 102 (1993) 105-123.

Curriculum Vitae

Education

01/2011 – 10/2014: PhD in Chemical Engineering.

Group of Catalytic Reaction Engineering.

Swiss Federal Institute of Technology, Lausanne (EPFL).

09/2008 – 08/2010: MSc in Process and Technology. Grade average 4.8 (out of 5.0).

Department of Technology of Petrochemical Synthesis and Artificial Liquid Fuel.

M.V. Lomonosov Moscow State Academy of Fine Chemical Technology.

09/2004 – 07/2008: BSc in Process and Technology. Grade average 4.5 (out of 5.0).

Department of Technology of Petrochemical Synthesis and Artificial Liquid Fuel.

M.V. Lomonosov Moscow State Academy of Fine Chemical Technology.

Professional Experience

01/2011 – 10/2014: Doctoral Assistant.

Group of Catalytic Reaction Engineering, Swiss Federal Institute of Technology, Lausanne (EPFL).

Main achievements:

I developed the catalysts for selective hydrogenation of alkynols and aromatic nitro-compounds (target products - key intermediates in fine chemicals industry). The technology was patented by **DSM Nutritional Products**.

Teaching assistance:

- "Eco-Friendly Production of the Chemicals and Process Intensification" by Prof. A. Renken.
- "Chemical Engineering of Heterogeneous Reactions" by Prof. L. Kiwi-Minsker.

- "Théorie des réacteurs" by Prof. L. Kiwi-Minsker.
-

09/2008 – 05/2009: Part-time Engineer in Quality Control Laboratory.

All-Russian Research Institute of Oil Refining, Moscow.

Key responsibilities:

- Design, operation and service of a cracking unit.
- Quality control of the products of thermo-oxidative cracking.
- Purchase of the equipment based on the laboratory needs.

Internships and Projects

01/2010 – 07/2010: Swiss Federal Institute of Technology, Lausanne (EPFL).

Master thesis internship. Title: "Structure Sensitivity of Acetylene Hydrogenation over Size/Shape-Controlled Palladium Nanoparticles".

This work represents a critical advancement in a nano-scale catalyst optimization and constitutes a powerful tool for rational catalyst design with multiple applications.

04/2008 – 06/2008: A.V. Topchiev Institute of Petrochemical Synthesis, Moscow, Russia.

Bachelor project. Title: "Synthesis and Physicochemical Properties of Mesoporous Oxides".

Following high demand for effective oil processing, I developed the synthesis of mesoporous catalysts for potential use in hydrotreatment of petroleum fractions.

Languages

English: Fluent (C1) **French:** Intermediate (B1/B2) **Russian:** Native speaker

Publications

[1] A. Yarulin, C. Berguerand, A. Olasolo Alonso, I. Yuranov, L. Kiwi-Minsker. Increasing Pt Selectivity to Vinylaniline by Alloying with Zn via Reactive Metal-Support Interaction. *Catal. Today* (Submitted).

[2] A. Yarulin, C. Berguerand, I. Yuranov, F. Cárdenas-Lizana, I. Prokopyeva, L. Kiwi-Minsker. Pt-Zn Nanoparticles Supported on Porous Polymeric Matrix for Selective 3-Nitrostyrene Hydrogenation. *J. Catal.* **2015**, 321, 7.

[3] A. Yarulin, I. Yuranov, F. Cárdenas-Lizana, D.T.L. Alexander, L. Kiwi-Minsker. How to Increase the Selectivity of Pd-based Catalyst in Alkynol Hydrogenation: Effect of Second Metal. *Appl. Catal. A* **2014**, 478, 186.

[4] A. Yarulin, I. Yuranov, F. Cárdenas-Lizana, P. Abdulkin, L. Kiwi-Minsker. Size-effect of Pd-(Poly(N-vinyl-2-pyrrolidone)) Nanocatalysts on Selective Hydrogenation of Alkynols with Different Alkyl Chains. *J. Phys. Chem. C* **2013**, *117*, 13424.

[5] A. Yarulin, R.M. Crespo-Quesada, E.V. Egorova, L.L. Kiwi-Minsker. Structure Sensitivity of Selective Acetylene Hydrogenation over the Catalysts with Shape-controlled Palladium Nanoparticles. *Kinet. Catal.* **2012**, *53*, 253.

[6] M. Crespo-Quesada, A. Yarulin, M. Jin, Y. Xia, L. Kiwi-Minsker. Structure Sensitivity of Alkynol Hydrogenation on Shape- and Size-Controlled Palladium Nanocrystals: Which Sites Are Most Active and Selective? *J. Am. Chem. Soc.* **2011**, *133*, 12787.

[7] M. Crespo-Quesada, J.-M. Andanson, A. Yarulin, B. Lim, Y. Xia, L. Kiwi-Minsker. UV-Ozone Cleaning of Supported Poly(vinylpyrrolidone)-Stabilized Palladium Nanocubes: Effect of Stabilizer Removal on Morphology and Catalytic Behavior. *Langmuir* **2011**, *27*, 7909.

Conferences

23.08.2014 - 27.08.2014: 21st International Congress of Chemical and Process Engineering, Prague, Czech Republic.

Title: Optimization of Pt Catalyst for Selective Nitrostyrene Hydrogenation (*Oral presentation*)

06.09.2013: Swiss Chemical Society Fall Meeting, Lausanne, Switzerland.

Title: Activity and Selectivity of Pd Catalyst in Liquid-Phase Alkynol Hydrogenation: Effect of Particle Size and Modification with the Second Metal (*Oral presentation*).

23.06.2013 - 26.06.2013 Summer School Catalysis for Sustainability: “Exploring Resource Diversity for Energy & Materials Supply”, Rolduc Abbey, the Netherlands.

Title: Monodispersed Pd Nanoparticles for Liquid-Phase Alkynol Hydrogenation: How to Improve Selectivity? (*Poster*).

01.07.2012 - 06.07.2012: 15th International Congress on Catalysis, Munich, Germany.

Title: Shape-Tailored Monodispersed Palladium Nanoparticles in Acetylene Hydrogenation: The Effect of Stabilizer and Second Metal (*Poster*).

16.06.2011 - 17.06.2011 1st Swiss Heterogeneous Catalysis Meeting, Grindelwald, Switzerland.

Title: Shape and Size-tailored Palladium Nanoparticles to Study Structure Sensitivity of 2-methyl-3-butyn-2-ol Hydrogenation (*Oral presentation*).